

TU Braunschweig – Niedersächsisches Forschungszentrum für  
Luftfahrt

Berichte aus der Luft- und Raumfahrttechnik

Forschungsbericht 2017-05

**Aeroacoustic Wind Tunnel Correction  
Based on Numerical Simulation**

**Jin Jiao**

Deutsches Zentrum für Luft- und Raumfahrt e.V. (DLR)  
Institut für Aerodynamik und Strömungstechnik  
Technische Akustik  
Lilienthalplatz 7  
38108 Braunschweig

---

Diese Veröffentlichung wird gleichzeitig in der Berichtsreihe "NFL - Forschungs-  
berichte" geführt.

Diese Arbeit erscheint gleichzeitig als von der Fakultät für Maschinenbau der  
Technischen Universität Carolo-Wilhelmina zu Braunschweig zur Erlangung des  
akademischen Grades einer Doktor-Ingenieurin genehmigte Dissertation.



Aeroacoustic Wind Tunnel Correction Based on Numerical Simulation

Von der Fakultät für Maschinenbau  
der Technischen Universität Carolo-Wilhelmina zu Braunschweig

zur Erlangung der Würde

einer Doktor-Ingenieurin (Dr.-Ing.)

genehmigte Dissertation

von : Jin Jiao  
aus : Shaanxi(China)

eingereicht am : 17.01.2017  
mündliche Prüfung am : 21.04.2017

Gutachter : Prof. Dr.-Ing. Jan Werner Delfs  
Prof. Dr.-Ing. Sabine Christine Langer

2017



# Abstract

As an unavoidable factor of the aeroacoustic study in the open-jet wind tunnel, the free shear layer induced by the nozzle performs significant effects on the sound propagation. These effects include the direction alteration and the amplitude reduction (caused by the mean flow gradient and the turbulence), as well as the spectral redistribution (caused by the turbulence) of the original incident sound wave. To eliminate the misunderstandings and incorrect conclusions drawn from the measurement data in the open-jet wind tunnel, a reliable correction method for the shear layer effects is necessary. The thesis focuses on the numerical investigation of the free shear layer effects under various situations: the variation in the shear layer thickness, in the shear layer shape, in the flow speed, in the source frequency and in the flow type (averaged mean flow including non parallel flow effects or turbulent flow). In this way, a systematical and detailed analysis of the free shear layer effects is provided with the evaluation of the state of the art correction method (Amiet's approach).

Using a hybrid Computational AeroAcoustics method, the mean flow gradient effects and the turbulence effects were treated separately to study their influences on both two-dimensional and three-dimensional sound propagation. The numerical results indicated a slight influence from the shear layer thickness and the source frequency in the 2D averaged shear flow, whereas the accuracy of the correction method can be improved by applying a modified model in the curved shear flow. In the 3D averaged planar shear flow, the correction method showed a good agreement with the numerical results. A 'dangerous area' was identified in the 3D rectangularly shaped shear flow, where the correction method failed to handle the shear layer effects appropriately. Moreover, the spectral broadening effects due to the turbulence was observed in both 2D and 3D as expected. The results indicated a stronger amplitude reduction with increasing source frequency, flow speed as well as the shear layer thickness.

These results offer insights into the variation of the shear layer effects with each parameter. The correction method (Amiet's approach) is proven to be efficient in 2D and specific 3D (source-observer plane perpendicular to the shear layer) situations. The error due to the shear layer shape in 3D can be avoided by locating the microphones outside the aforementioned 'dangerous area'. The position of such a 'dangerous area' is found to be related to the size of the nozzle geometry. Moreover, primary studies of the turbulent shear layer effects illustrate severe spectral broadening and amplitude reduction (at the tone frequency) as the source frequency, the flow speed, the shear layer thickness increases.



# Zusammenfassung

Unvermeidbar bei akustischen Untersuchungen in einem Windkanal mit offener Messstecke ist die signifikante Veränderung der Schallausbreitung beim Durchgang durch die freie Scherschicht. Die Effekte sind Richtungsänderungen und Amplitudenänderungen der Schallwellen (verursacht durch die mittleren Strömungsgradienten und zu einem kleinen Teil durch die Turbulenz), sowie die spektrale Umverteilung (verursacht durch die Turbulenz) der ursprünglich einfallenden Schallwelle. Um die Messdaten aus offenen Messstrecken richtig interpretieren zu können, ist ein zuverlässiges Korrekturverfahren nötig zur Kompensation der Scherschichteffekte. Diese Arbeit konzentriert sich auf die numerische Untersuchung Effekte der freien Scherschicht auf den Schalldurchgang. Folgende Parameter wurden dabei betrachtet: Scherschichtdicke, Scherschichtform, Strömungsgeschwindigkeit, Quellfrequenz, stationäre und turbulente Strömung. Auf diese Weise wird eine systematische und detaillierte Analyse der Effekte der freien Scherschicht auf die Akustik möglich. Die Ergebnisse werden mit der Korrekturmethode von Amiet verglichen, welche zur Zeit der Stand der Technik ist.

Genutzt wurde ein hybrides 'Computational Aeroacoustics'-Verfahren bei dem die Effekte durch mittlere Strömungsgradienten separat von den Effekten durch zeitaufgelöste Turbulenz betrachtet werden kann. Untersucht wurden sowohl zwei- als auch dreidimensionale Schallausbreitung. Es stellt sich heraus, dass sowohl die Grenzschichtdicke als auch die Quellfrequenz bei 2D stationärer Strömung nur einen geringen Einfluss auf die notwendige Korrektur haben. Jedoch kann die Berücksichtigung der Krümmung der Scherschicht die Korrektur verbessern. Bei einer dreidimensionalen quasi 2D Scherschicht stimmt die Korrekturmethode gut mit den numerischen Ergebnissen. Eine rechtwinklige Düsenserschicht lässt die Korrekturmethode in lateralen Bereichen sogar vollständig versagen (Kritischer Bereich). Bei Untersuchungen des Einflusses der zeitaufgelösten Grenzschichtturbulenz ist sowohl in 2D, als auch in 3D eine Umverteilung der Schallenergie in zum Ton benachbarte Frequenzbänder beobachtet worden ('Spectral Broadening'), sowie eine zeitgleiche Reduktion des Tonschallpegels. Die Amplitudenreduktion steigt mit zunehmender Quellfrequenz, Strömungsgeschwindigkeit und Scherschichtdicke.

Die erzeugten Ergebnisse bieten Einblicke auf den Einfluss der Scherschicht auf Schalldurchgang abhängig von unterschiedlichen Scherschichtparametern. Die Korrekturmethode nach Amiet hat sich für 2D Probleme und für den Schalldurchgang in der Mittelebene in 3D bewährt. Messfehler bei rechtwinkligen Scherschichten können vermieden werden durch Meidung von stark lateralen Messpositionen. Die Lage des kritischen Bereichs ist abhängig von den Abmessungen der Düse. Erste Ergebnisse des Einflusses der instationären Turbulenz zeigen eine starke spektrale Aufweitung ('spectral broadening') bei gleichzeitiger Tonamplitudenreduktion. Der Einfluss

wird stärker mit steigender Quellfrequenz, steigender Strömungsgeschwindigkeit und dickerer Scherschicht.

# Acknowledgement

Foremost, I would like to express my special appreciation and thanks to my supervisor Professor Dr.-Ing. Jan Delfs for his helpful advices and discussions during my Ph.D study. His guidance helped me a lot in the research and writing of this thesis. With his help, it becomes possible for me to get a deeper understanding of the computational aeroacoustics. I would like to thank him for supporting my study and the valuable advises on my way to be a researcher.

I also want to thank my colleagues from the Technical Acoustic department at DLR for their wonderful collaboration. They supported me greatly and were always willing to help me in both my study and my daily life. I would particularly like to thank Mr. Jürgen Dierke for his excellent help through my entire Ph.D study. Mr. Dierke has been helpful in providing advices on programming issues and analysis of the numerical results. In addition, I would like to thank the colleagues, who provided detailed and valuable advices in the writing of my thesis. I also want to thank the China Scholarship Council for the financial support of my study.

Last but not the least, I would like to thank my family: my parents and my husband for supporting me spiritually throughout writing this thesis and my life in general. Their devotion, unconditional love and support have enabled me to complete this Ph.D study.



# Contents

<b>1</b>	<b>Introduction</b>	<b>1</b>
1.1	Background . . . . .	1
1.2	Free shear layer effects in the open-jet test section wind tunnel . . . . .	2
1.3	Literature review . . . . .	4
1.3.1	Studies on the mean flow gradient effect in the free shear layer . . . . .	4
1.3.2	Studies on the turbulence effect in the free shear layer . . . . .	6
1.4	Objective and the approach . . . . .	8
1.5	Outline of the thesis . . . . .	8
<b>2</b>	<b>Amiet's approach</b>	<b>11</b>
2.1	Introduction . . . . .	11
2.2	Basic idea and the correction model . . . . .	12
2.3	Angle correction . . . . .	14
2.3.1	Total reflection . . . . .	15
2.3.2	Zone of silence . . . . .	15
2.3.3	Application of the angle correction in the open-jet wind tunnel . . . . .	16
2.4	Amplitude correction . . . . .	17
2.4.1	Application of the amplitude correction in the open jet wind tunnel . . . . .	18
2.5	Summary . . . . .	19
<b>3</b>	<b>Numerical method</b>	<b>21</b>
3.1	Introduction . . . . .	21
3.2	PIANO (Perturbation Investigation of Aerodynamic Noise) . . . . .	22
3.2.1	Governing Equations . . . . .	22
3.2.2	Numerical algorithm . . . . .	23
3.2.3	Boundary conditions . . . . .	24
3.2.4	Sound source model . . . . .	25
3.3	Reconstruction of the turbulence (FRPM method) . . . . .	26
3.3.1	Governing equations . . . . .	27
3.3.2	Modeling of turbulent velocities (FRPM method) . . . . .	28
3.4	Acoustic quantities . . . . .	31
<b>4</b>	<b>Numerical Results</b>	<b>33</b>
4.1	Sound propagation through analytical shear layers (2D) . . . . .	33
4.1.1	Computational setup . . . . .	33
4.1.2	Characteristics of the base flow . . . . .	35
4.1.3	Sound propagation through constant thickness shear layers . . . . .	38
4.1.4	Alteration of the sound wave amplitude through constant thickness shear layers . . . . .	45

4.1.5	Sound propagation through wind tunnel shear layers . . . . .	48
4.1.6	Alteration of the sound wave amplitude through spreading shear layers . . . . .	52
4.1.7	Source directivity in constant thickness and wind tunnel shear flows . . . . .	54
4.2	Sound propagation through the curved shear layer (2D) . . . . .	56
4.2.1	Computational setup . . . . .	56
4.2.2	Characteristics of the base flow . . . . .	57
4.2.3	Centerline models applied in Amiet's approach . . . . .	59
4.2.4	Sound propagation through curved shear layers . . . . .	59
4.2.5	Alteration of the sound wave amplitude through curved shear layers . . . . .	61
4.2.6	Sound propagation through the curved shear layer considering the nozzle rim reflection . . . . .	63
4.2.7	Alteration of sound wave amplitude through the curved shear layer as nozzle surface considered . . . . .	64
4.3	Sound propagation through analytical shear layers (3D) . . . . .	66
4.3.1	Computational setup . . . . .	67
4.3.2	Sound propagation through the planar and the realistic wind tunnel shear layers . . . . .	68
4.3.3	Alteration of the sound wave amplitude through 3D analytical shear layers . . . . .	77
4.4	Sound propagation through turbulent shear layers (2D) . . . . .	82
4.4.1	Computational setup . . . . .	82
4.4.2	Characteristics of the turbulence part in the free shear layer . . . . .	84
4.4.3	Sound propagation through the turbulent shear layer . . . . .	85
4.4.4	Alteration of the sound wave characteristics through the turbulent shear layer . . . . .	88
4.4.5	Role of turbulent pressure fluctuation in the scattering effects . . . . .	96
4.5	Sound propagation through turbulent shear layers (3D) . . . . .	96
4.5.1	Computational setup . . . . .	96
4.5.2	Sound propagation through the turbulent shear layer . . . . .	100
4.5.3	Alteration of the sound wave characteristics through the turbulent shear layer . . . . .	100
<b>5</b>	<b>Summary, conclusions and outlook</b> . . . . .	<b>105</b>
5.1	Summary . . . . .	105
5.2	Conclusions . . . . .	106
5.3	Outlook . . . . .	107
<b>A</b>	<b>Derivation of Amiet's approach</b> . . . . .	<b>109</b>
A.1	Refraction angle change . . . . .	109
A.2	Refraction amplitude change . . . . .	112

<b>Contents</b>	<b>ix</b>
<hr/>	
<b>B Figures of the numerical results</b>	<b>115</b>
<b>C Instabilities in the 3D simulation in the turbulent shear layer</b>	<b>123</b>
<b>Nomenclature</b>	<b>127</b>
<b>Bibliography</b>	<b>131</b>



# Introduction

---

## 1.1 Background

Aeroacoustics is a relatively young subject in the branch of the aerodynamics. It met its golden age in the early 1950s, since Lighthill published his famous Lighthill's analogy [M. J. Lighthill 1952, M. J. Lighthill 1954]. So-called Lighthill's analogy is a rearrangement of the Navier-Stokes equations into an inhomogeneous wave equation, so that all non-linear terms are shifted to the right hand side, which were explained by Lighthill as the flow source terms. They consist of the changes in flow velocity, entropy as well as the viscous friction stresses. Based on the assumption of the source terms in Lighthill's equation, it is possible to physically understand the origin of free turbulence induced sound, then to further model them mathematically.

Beside the theoretical studies, experimental studies also play an important role in the aeroacoustic research. Similar as the studies in the fluid dynamics, most of the aeroacoustic experiments are usually operated in wind tunnels. Comparing with full-scale flight test, it can provide valuable data for the development and validation of aerodynamic design in more controllable manner and at a reduced cost. For example, aeroacoustic wind tunnel tests can give the source and directivities of the aircraft noise, which could be used in both validations of numerical methods and foundations of noise reduction treatment. The aeroacoustic wind tunnel can be generally classified into two types according to the form of its test section, i.e. closed and open-jet test section wind tunnels. Both of them are commonly used for aeroacoustic studies of a variety of flow-induced noise phenomena. The choice of wind tunnels is usually relevant to the test purpose, model size as well as the requirement of the flow parameters.

The open-jet test section wind tunnel (refer as open-jet wind tunnel in the following) consists of an anechoic chamber around the test section, which can provide a near-anechoic environment without wall reflections that occur in a closed-jet wind tunnel. Besides, this facility can significantly improve the signal-to-noise ratio at the single microphone via measurement in the farfield out of the flow. This feature significantly reduces the contamination from the background noise caused by the flow and its interaction with the supporting system. However, one essential problem bothering acousticians is the free shear layer effects on the propagation of sound waves through it in such an open-jet wind tunnel. The free shear layer is formed due to the velocity gradient between the nozzle flow and the surrounding quiescent media when the flow travels from the open jet through the test section. Since the microphones are usually placed out of the jet flow in the farfield, the

sound waves generated by the test object have to pass through the free shear layer before reaching the microphones. The sound waves experience complex propagation effects during the traveling through the free shear layer, including the significant alteration in the direction, the amplitude as well as the frequency band. If the corresponding farfield measurement data are used to trace back to determine the originates and characteristics of the noise source, it can lead to deviations from the actual situation and finally yield incorrect conclusions if the free shear layer effects were ignored. Moreover, in the acoustic wind tunnel tests a typical requirement is to distinguish discrepancies starting from  $1 \sim 1.5dB$  when assessing aeroacoustic sources. It means that any systematic errors (e.g. caused by the shear layer) in the measurement setup, which lead to exceeding this value may be critical.

Regarding the shear layer problem in the open-jet wind tunnel, it is quite necessary to put forward a method to remove the effects from the measurement data. Many researchers noticed the phenomena since the late 1970s and studied it in experimental or theoretical ways, which will be presented later in the literature review. Based on these studies, several solutions were raised up to correct the deviations caused by the shear layer effects. However, most of the solutions were derived with some simplifications. An exhaustive understanding of the shear layer effects is in shortage due to the limitations of the wind tunnel test itself on such a problem. Such a gap could now be filled with the help of Computational AeroAcoustics (CAA) methods after its rapid development in the past two decades, which is deemed as the topic of this dissertation.

In the last two decades, a routine use of CAA was established and has undergone spectacular progress in the research field. Various computational methods were extensively developed and utilized to describe the aerodynamically generated noise and the sound wave propagation in an inhomogeneous flow field. CAA was taken as an efficient tool in aeroacoustic studies aiming at understanding the physics of noise generation and propagation, as well as the noise prediction. Either hybrid CAA or direct noise computation (DNC) has shown good performance in the aeroacoustic studies. Considering its application in the current topic, CAA can both complement the experimental work with the numerical database and provide an opportunity to validate the state-of-the-art correction method under various situations. The situations could vary in shear layer thickness, shear layer shape, flow speed and source frequency etc. It is convenient to figure out the influence of the variation of each parameter independently with CAA methods while excluding the possible environmental effects occurring in the experiment. With the help of CAA methods these shear layer effects will be intensively investigated in the current work.

## 1.2 Free shear layer effects in the open-jet test section wind tunnel

It is known that the real shear flow is highly unsteady turbulent flow. When the sound waves pass through it, their characteristic modifications are mainly caused

## 1.2. Free shear layer effects in the open-jet test section wind tunnel 3

by two factors. One is induced by the mean flow gradient while the other is caused by the turbulence in the shear layer. Fig.1.1 illustrates the typical flow structure in an open-jet wind tunnel and the test set-up for the measurement. The source is positioned in the potential core of the open jet flow to minimize turbulence effect of the jet flow, while microphones are usually placed out of flow in the anechoic chamber where an approximate quiescent air could be guaranteed. The mean flow profile indicated by the black vectors is obtained from the time-averaged horizontal velocity. The time invariant turbulence is represented by the circular vortices. The effects induced by these two parts are usually treated separately in the acoustical study.

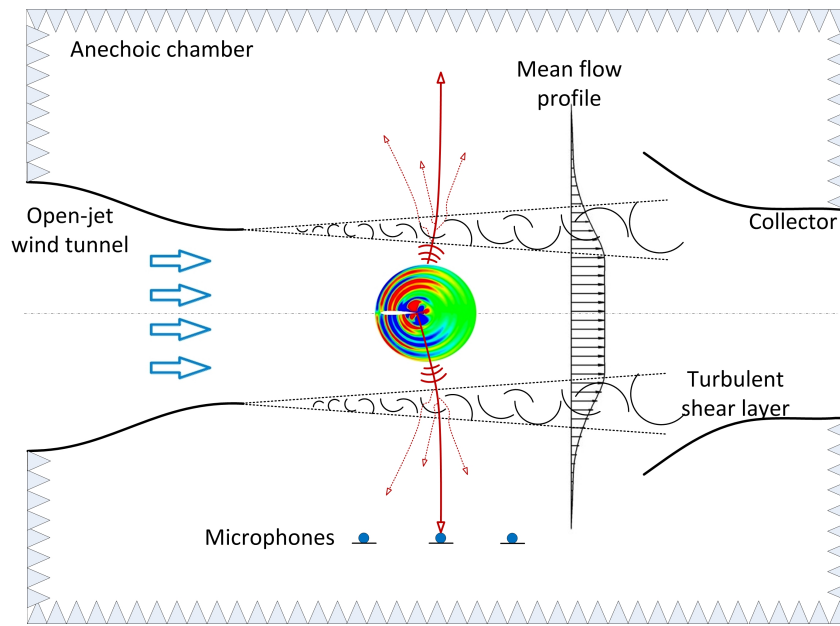


Figure 1.1: Sound transmission through a free jet shear layer

Considering firstly the influence of the mean flow gradient alone, it generally results in two phenomena: sound wave refraction and reflection. Due to the accompanying interaction of sound waves with a time-averaged shear flow, a portion of the power of the incoming wave transmits through the shear layer but radiates in a modified angle, named as refraction, indicated as solid arrows in Fig.1.1. The other portion of the power is reflected back into the jet flow, named as reflection. The strength of the refraction and reflection depends on the flow speed and the incident angle of sound wave into the shear layer. These effects directly lead to the direction and amplitude alteration of the original sound waves, which obviously affect the accuracy of the measurement data outside the shear layer.

Considering the turbulence part in the shear layer, it expresses itself as fluctuations of the properties in the shear flow. When sound waves pass through such a medium, the interaction between the sound wave and the random fluctuating medium results in a power loss in the sound wave magnitude and a modification

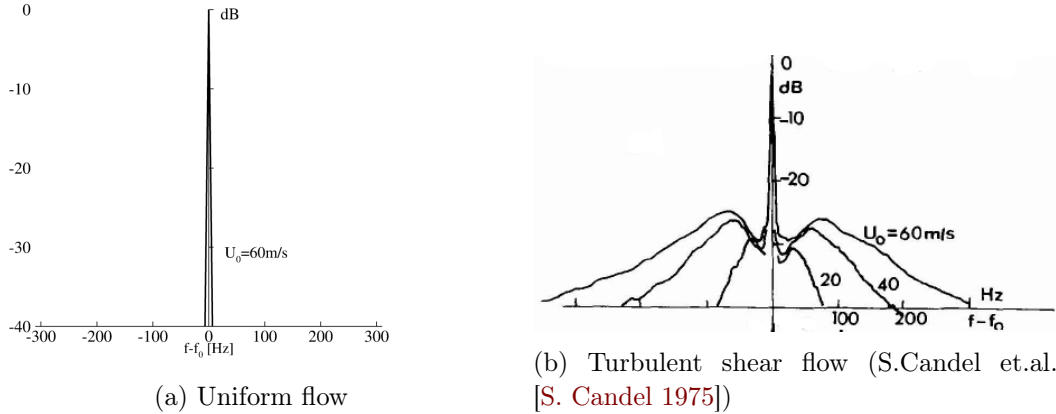


Figure 1.2: Spectrum at a single measurement point in the uniform flow and turbulent flow.

in the sound wave spectral content. The phenomenon is especially obvious if the source is a tonal. Standing at a fixed microphone position out of flow, the perceived signal owns a lower magnitude at the tone frequency compared with that in the no-turbulence flow. This is due to the scattering of the original sound wave by the turbulence, as indicated by the thin dashed arrows. Such a scattering is not only in the magnitude but also in the frequency, which leads to a broadening of the spectrum into neighboring bands of the tone frequency, as shown in Fig.1.2b. Comparing with the spectrum at the same position in the uniform flow (refer to Fig.1.2a), Fig.1.2b illustrates a broader spectral distribution as well as two humps aside the primary tone frequency, whose corresponding frequencies are flow speed dependent. Such a phenomenon is referred as spectral broadening or haystacking. Besides, the turbulence could absorb partially the sound power from the primary source while generate additional noise as an unexpected source. These effects will not be considered in the current study since they are believed to play a less important role in the open-jet wind tunnel tests[K. K. Ahuja 1978].

### 1.3 Literature review

The aforementioned classification of the shear layer effects are exactly extracted from the previous researches on the subject. In this section, the previous studies will be introduced according to this classification as well to give a clear view of the development of corresponding researches.

#### 1.3.1 Studies on the mean flow gradient effect in the free shear layer

Several analytical and numerical methods have been developed to model the refraction and reflection of sound waves by the mean flow gradient through the shear layer. Generally, the free shear layer was approximated with some simplified models

in these work. In Miles [J. W. Miles 1957] and Ribner's [H. S. Ribner 1957] work the free shear layer was modelled as a zero-thickness interface (vortex sheet) between two relatively moving media. Based on it, they established the relation between the acoustical parameters of a plane incident wave, reflected wave and transmitted wave. Although it is an idealized analysis, it provides a feasible way to interpret and analyze the mean flow gradient effect in the free shear layer. Taking these analyses and their shear layer model as the base, Gottlieb [P. Gottlieb 1960] derived the far-field approximation of specified source types later. To further approach the realistic mean flow gradient between two media, Graham and Graham [E. W. Graham 1969] approximated the shear layer as two different models and numerically solved the corresponding equation of the parallel sheared flow. One model contained two plane zero-thickness interfaces with distance apart and a uniform flow inbetween. The other was a finite thickness shear layer with a linear velocity profile. This work provided some basic information on the shear layer thickness effect but was still restricted to the plane sound wave. Noticing the requirement in the open-jet wind tunnel for the shear layer correction for more general cases, Amiet posed an approach for the treatment of the planar shear layer refraction effect by combining solution of Ribner [H. S. Ribner 1957] and Miles [J. W. Miles 1957] as well as geometrical acoustics [R. K. Amiet 1975], which is independent of the source type and the source frequency. The method calibrated both the direction alteration and the magnitude alteration of the sound wave propagation in a shear flow to that in a uniform flow. Later the approach was extended by Amiet to applications for both planar and cylindrical shear layers [R. K. Amiet 1978]. The only limitation of the method was that the source should be on the jet centerline of the cylindrical nozzle, which was overcome by Morfey and Joseph [C. L. Morfey 2001]. The approach has been widely applied in the open-jet wind tunnel correction due to its simplicity and applicability. Several experimental validations were conducted to examine its reliability and accuracy for the cylindrical shear layer [A. Ozkul 1979] [R. H. Schlinker 1980] [K. K. Ahuja 1981] and the planar shear layer [C. Bahr 2010] [C. Bahr 2011]. Since the experimental validations are usually affected by other factors like the specifics of the employed source, the turbulence in the shear layer and the background noise, many researchers sought for numerical methods to investigate the efficiency of the correction approach [L. Koop 2005] [T. Padois 2013] by solving Linearized Euler Equations (LEE). Additionally, accompanying the common application of the method, some modifications were adopted to improve its accuracy in specified open-jet wind tunnels [W. H. Herkes 1985] [Y. Wang 2015].

In addition to Amiet's approach, some other methods were provided as well for the correction of the mean flow gradient effect. During the same period as Amiet, Tester and Burrin [B. J. Tester and R. H. Burrin 1974] conducted a theoretical study on the refraction effect while considering the axial variation of the shear layer, of which the results show qualitative agreement with the experimental data. For further study of the shear layer effect, they suggested a more realistic mean flow model in the theoretical study. Another approach was provided by Morfey and Tester [B. J. Tester 1976] [C. L. Morfey 1977] for facility-to-flight corrections in the open-

jet wind tunnel by numerically solving Lilley's equation on an axisymmetric stratified base flow. In their approach, the deviation brought by the finite thickness and the spreading shape of the shear layer were examined and compared with geometric acoustics approximation. However, the application of the approach in the wind tunnel tests was limited due to its complexity in the routine use. Another correction procedure was given by Candel [S. M. Candel 1976] by implementing a first-order numerical geometrical acoustics solution in a realistically modelled mean shear flow based on measurements. By comparing with Amiet's approach, it presented a quite close agreement except at some extreme measurement angles [J. D. Belleval 1976].

### 1.3.2 Studies on the turbulence effect in the free shear layer

As another important factor of the free shear layer effects, the turbulence scattering effect was extensively studied in the theoretical way at the very beginning. Several approximation schemes were given to roughly estimate its influences on the wave propagation. The primary studies were carried out using a frozen turbulence and the single scattering (Born approximation) assumptions, as done by Lighthill [M. J. Lighthill 1953]. By using the frozen turbulence assumption, the turbulence is regarded as inhomogeneities which only vary in space during the time of passage of an incident wave. The single scattering assumption, as its name implies, is a reasonable approximation for the situation when incident wavelength is smaller than the macro-scale of turbulence. Based on these assumptions Lighthill derived an estimation of the energy scattered per unit time from unit volume of the turbulence. In his derivation, the mean flow was ignored, while the parameters from the incident wave and the turbulence were included. He also predicted the directional distribution of the scattered wave by considering a single scattering process as well as an uniform (i.e. quite random) directional scattering with the consideration of a multiple successive scattering. The latter one was more appropriate for the situation when the incident wavelength is less than the macro-scale of the turbulence. The frozen turbulence assumption taken by Lighthill simplified the theoretical analysis since scattered waves were confined to be of the same frequency as incident waves. As the source frequency increases, the traveling time of the sound wave in the turbulence increases accordingly, in which the turbulence can not be considered 'frozen' any more. Therefore, Howe [M. S. Howe 1973] examined a multiple scattering of incident waves in a temporally evolving turbulence field without concerning the mean flow. In the study he figured out the spectral broadening of the acoustic spectrum by the temporally evolving field, which differs from the spatial scattering mentioned earlier. This phenomenon was experimentally illustrated in the work by Candel et al. [S. Candel 1975], followed by the analysis and comparison with the theoretical study [S. M. Candel 1976] according to geometric acoustics. In their study a broadening of the spectrum was observed at out-of-flow positions from a monochromatic test source inside the open-jet flow potential core. The received signal out-of-flow showed spectral broadening with two sidebands (see Fig.1.2b). It was found in their study that the level and corresponding frequencies of these sidebands were relevant

with the flow speed, the shear layer thickness as well as the source frequency. Similar phenomena were observed in many experimental studies carried out subsequently for the investigation of free shear layer effects [K. K. Ahuja 1978] [K. K. Ahuja 1981] [A. Ozkul 1979] [R. H. Schlinker 1980] [J. C. Hardin 1981]. In the work by Ahuja et al. [K. K. Ahuja 1978] [K. K. Ahuja 1981], they found that the turbulence scattering becomes effective only when the ratio between the shear layer thickness and the acoustic wavelength of discrete tones approaches a value of 10 and the signal experiences a reduction in the magnitude at the tone frequency. Moreover, these effects became more significant as the flow speed increased. In Schlinker and Amiet's report [R. H. Schlinker 1980], beside the qualitative validation of the scattering controlling parameters in the experiments they derived an estimation to predict the onset of the turbulence scattering based on the scattered energy equation given by Lighthill [M. J. Lighthill 1953]. The prediction lost its function at high frequencies since it was derived from the single scattering assumption. They noted that the spectral broadening is caused by the Doppler shift of incident wave, in which the scattered volume shows a Doppler shift to lower frequencies downstream and higher frequencies upstream of the cross-point of the incident wave with the shear layer. In the work by Hardin et al. [J. C. Hardin 1981], they believed that the spectral broadening was entirely relevant with the amplitude modulation of the signal by the time-varying shear layer, and the frequency shift hypothesis is not necessary for the explanation of the data. Some experimental work was also carried out by Ross et al. [R. Ross 1981] [R. Ross 1983] in the German-Dutch wind tunnel (DNW), who assessed the free shear layer effect using a 1/3-octave analysis. Their work showed that the turbulence effect correction was only necessary in the case of high velocity, high frequency and extreme microphone angles as long as the 1/3-octave analysis was used. Guedel conducted a comparison work between experiments and theoretical work, in which the latter one was deduced from single scattering models [A. Guedel 1985]. His work provided some parametric information of acoustic measurements in open-jet facilities as well as the limitation of the theoretical analysis. The analysis based on the single scattering was proved to be sufficient for the case when the parameter  $M\delta/\lambda$  is less than 1.5 (where  $M$  is the flow Mach number,  $\delta$  is the shear layer thickness and  $\lambda$  is the incident acoustic wavelength).

In the recent years, the scattering effect due to the turbulence attracted again the attention due to the widely application of the open-jet facility as well as the development of numerical methods, of which the latter enables to have a deeper understanding of the mechanism of the scattering process. Apart from the experimental work [P. Sijtsma 2014], which basically verified the phenomena observed in Candel's study, McAlpine et al. [A. McAlpine 2009] presented an analytical model with a high-frequency weak-scattering approach for the spectral effect of the turbulent shear layer. The double-humped spectrum in Candel's test were qualitatively reproduced by the model, while the quantitative differences were still present. The CAA method was also adopted to study the spectral broadening effect of the turbulent shear layer, as done by Ewert et al. [R. Ewert 2008]. In their work the turbulent base-flow was modeled using a stochastic method, by which the general trends of

the spectrum were well predicted when compared with Candel's tests.

## 1.4 Objective and the approach

As one may notice from the above, most studies were carried out either experimentally or theoretically and generally without showing the individual effects from the two factors in the free shear layer. Although several correction methods have been provided for the open-jet wind tunnel experiments, a systematical study of the problem and verification from the numerical field is lacking. Moreover, it is noted that the shear layer shape may severely affect the accuracy of the correction method if the microphone-source plane is not perpendicular to the shear layer while a laterally variation of the microphone position. Such a situation was not seriously treated in the past. The data corrected by the current methods may not achieve the expected accuracy due to the simplifications and assumptions introduced in the derivative procedure, which are to some degree not coincident with the real situation in the wind tunnel tests.

Therefore, this thesis aims at deeply studying the free shear layer effects in the open-jet wind tunnel with the help of CAA methods. The variation of several parameters, such as the shear layer thickness, the shear layer shape, the flow speed, the turbulence as well as the primary source frequency, are considered. The numerical results are subsequently compared with the correction method (Amiet's approach). By conducting such a strategy, a systematical and detailed understanding of the free shear layer effects can be achieved, including the transmission characteristics of the sound wave through the free shear layer as well as the quantitative influence of each parameter. The efficiency of the correction method under each situation are also provided. Additionally, the numerical results can be taken as complementary part for the correction method to improve its accuracy, avoid misinterpretation of the data and to potentially increase the range of measurement positions in the wind tunnel.

The entire work is carried out with a hybrid Computational Aeroacoustics method, in which the sound propagation is simulated by numerical acoustic methods on a background flow obtained by solving RANS equations. The turbulence feature is modeled with a 4D synthetic turbulence method, which enables us to separately study the turbulent effect and the mean flow gradient effect in the free shear layer.

## 1.5 Outline of the thesis

Chapter 2 gives a general description of the correction method for the mean flow gradient effects of the free shear layer derived by Amiet. The data obtained from Amiet's correction is taken as the theoretical value for the comparisons with numerical results in the following chapter. The basic equations are presented, which are necessary to describe features and important angles.

Chapter 3 addresses the numerical methods, including the methods of simulating

---

sound propagation in a non-uniform flow and the model of the turbulence reconstruction. A simple introduction of the sound source models applied in the study is provided together with some acoustic properties used in the future analysis.

Chapter 4 includes the simulation results of the shear layer effects. The mean flow gradient effect is investigated firstly following the sequence from two-dimensional to three-dimensional, based on the analytical mean flow field with constant thickness and the real wind tunnel flow field without turbulence. They are followed by the study of 2D shear layer shape effect and the nozzle surface reflection effect. Afterwards, the sound transmission through a 3D rectangular shear layer are simulated and analyzed. Finally, turbulence part will be superposed into the previous base flow to observe its scattering and spectral broadening effects on the sound propagation.

Chapter 5 comprises the summary of the numerical results and corresponding conclusions about the free shear layer effects. The possible research directions and advises for further work are presented as well.



# Amiet's approach

---

As mentioned earlier, many methods have been provided for handling the free shear layer effects in the open-jet wind tunnel. Amongst these, the approach derived by Amiet [R. K. Amiet 1975] has gained the most attention due to its generality and easy-applicability. It provides an easy but efficient way to correct the effect introduced by the mean flow gradient through the free shear layer, which can be applied to any source type since it corrects the alteration of both the amplitude and the propagation angle of the incident wave. The method is adopted also as the shear layer correction method in DLR's Aeroacoustic Wind tunnel Braunschweig(AWB), of which the shear flow is the main study object of the current research. Considering its frequent application in the experimental work in the AWB, the method is employed to offer the reference data as a theoretical solution for the comparison with the numerical results. Conversely, the numerical results are used to verify the reliability and the accuracy of the approach under various measurement situations. This chapter presents an introduction of the correction model of Amiet's approach and a detailed exploration of the key parameters and features of the correction equations.

## 2.1 Introduction

Amiet's approach is derived based on a transmission model by Ribner [H. S. Ribner 1957] and Miles [J. W. Miles 1957] as well as geometric acoustics. The transmission model established by Ribner and Miles provides a parametric relation between the incident wave and the transmitted wave for the sound propagation through an infinitely thin interface (vortex sheet) between two relatively moving media. Geometric acoustics helps to build the sound intensity variation while propagating in the uniform flow at both sides of the shear layer. Combining these two, Amiet constructed a complete approach for the open-jet shear layer correction to calibrate the mean flow gradient effect. The approach was firstly derived for a planar shear layer with the source and microphones located in the same perpendicular plane to the shear layer. Later it was extended to a more general case in which the microphone locations can vary spatially in 3D. Additionally, the solution was added for the cylindrical shear layer with an on-axis source. The approach takes into account both the amplitude and the angle corrections, which can be employed for the general cases of an unknown source at any frequency.

In the current study, only the corrections for the planar shear layer by Amiet are involved to treat the rectangularly shaped shear layer in the AWB. The information

for the cylindrical shear layer can be found in Amiet's paper [R. K. Amiet 1978] if interested. Besides, the two-dimensional model is taken in this chapter as the model for the introduction. A more general correction model is presented in the Appendix A.

Several assumptions were introduced for simplification in the derivation. Firstly, the shear layer is modelled as an infinitely thin interface (vortex sheet), which significantly simplifies the derivation and makes it possible to derive a relation of the acoustic perturbation across the shear layer from the specified boundary condition. In their study, Ribner and Miles assumed continuity of displacement across the interface, which is deemed reasonable in the physical study [L. M. B. C. Campos 1986]. In this way, the intensity variation of the incident sound wave due to the passage through the shear layer can be determined. This simplification differs from the real case where the free shear layer has a finite thickness varying axially as the flow goes downstream. The possible deviation caused by such an assumption will be examined numerically in the current study with a consideration of varying source frequency. As in the classical studies, the flow field is assumed uniform at both sides of the shear layer. The original derivation is obtained for the microphones in a stationary medium, which indicates a zero flow speed at one side. This assumption can be easily extended to a more general case, in which the flow speeds are non-zero at both sides but differ from each other. The fluid density is assumed to be identical at both sides of the shear layer. Both assumptions are reasonable and conform with the situation for the most low Mach number open-jet wind tunnels. Since the method aims at corrections for the mean flow gradient effect, the turbulence scattering is neglected. This neglect does not meet the reality, but it is reasonable to separately study the two factors in the free shear layer and present their contributions in the total effects individually. Furthermore, the reflection of the sound wave by another shear layer is neglected, although there are upper and lower shear layers in the open-jet wind tunnel. This neglect is reasonable for the most general situation in the low speed open jet wind tunnel since the reflected part by the free shear layer is of considerably smaller amplitude than the transmitted part and will not interfere with the original incident wave due to both the intensity dissipation and multiple reflections in the jet flow.

Regarding the acoustic feature of the source, the observer/microphone is assumed to be in both the geometrical and acoustic far-field of the source, which means that the distance between the observer and the source is significantly greater than both the source dimensions and the acoustic wavelength. And the reason for this assumption is that only the far-field part of the source is considered and used in the derivation.

## 2.2 Basic idea and the correction model

In this section, the basic idea of the derivation of the method is given with a two-dimensional model, as shown in Fig.2.1. As aforementioned, the shear layer is

simplified as an infinitely thin vortex sheet, which is illustrated by a zero-thickness plane parallel to the flow direction at a distance  $h$  away from the source. Below the shear layer the flow is uniform with the speed  $U_0$ , which exerts a convective effect on the wave propagation. This effect is expressed by spatially compressed sound wave signals upstream and stretched sound wave signals downstream in the figure. The phenomenon disappears above the shear layer, where the fluid is assumed to be at rest. The observer/microphone is located at a distance  $y_M$  from the source, which is indicated by point  $M$ . The dashed line from the source to  $M$  forms an angle  $\theta_M$  with the shear layer, representing the measurement angle defined in the wind tunnel test. The actual sound wave propagation path in the shear flow is shown by the solid lines from the source to the point  $C$  further to  $M$ , where  $C$  is the cross point with the shear layer. The sound wave follows the trace from  $C$  to  $M$  rather than from  $C$  to  $A$  since it is refracted by the shear layer. The original sound wave propagation direction makes an angle  $\theta_0$  with the shear layer in the uniform jet flow, which is defined as the radiation angle. After the passage through the shear layer, the modified wave propagation direction forms an angle  $\theta_t$  with the shear layer, which is named as transmission angle. If the shear layer was absent, the sound wave radiated from the source would follow the path from the source to the point  $C$  further to point  $A$ , which means that the data received at point  $M$  in a shear flow should be measured at point  $A$  in a uniform flow without shear layer. A relation is established between the acoustic parameters at point  $M$  and point  $A$  by Amiet. Once the data at the measurement location is known in the wind tunnel tests, the corresponding corrected data in a uniform flow can be determined. Point  $A$  is named as corrected position.

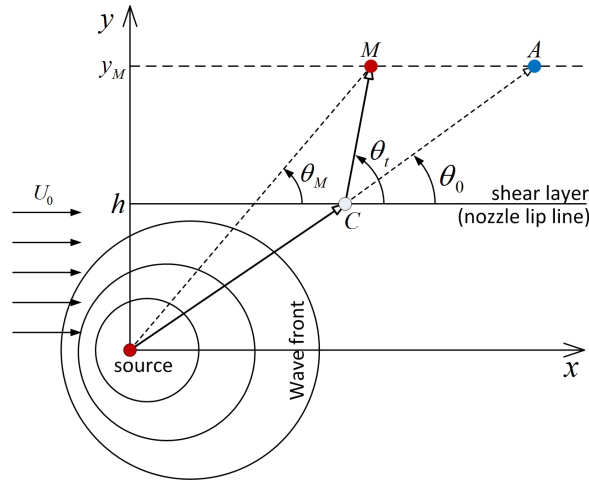


Figure 2.1: Correction model of Amiet's approach

Based on the presented model, a reversed derivation procedure is employed by Amiet in view of known information at the measurement point in the open-jet wind tunnel test. Firstly, the position of the cross point  $C$  needs to be determined, i.e.  $\theta_0$  should be fixed. For this purpose the geometrical relation between the length and

angle parameters in the model, as well as the sound propagation characteristic that the trace wave numbers of the incident and transmitted waves are equal along the  $x$ -axis as across the shear layer is exploited. This forms the basis for the relations between measurement angle, transmission angle and radiation angle. Then  $\theta_0$  is easily derived by an iteration process (e.g. Newton's method). Knowing the position of the cross point  $C$ , the amplitude of the pressure perturbation measured at point  $M$  can be traced back to point  $C+$  right above the shear layer, which is used to derive the value at point  $C-$  just below the shear layer according to the transmission relation proposed by Ribner [H. S. Ribner 1957] and Miles [J. W. Miles 1957]. Until now, the sound wave amplitude alteration resulting from the shear layer has been calibrated out from the measurement data. The amplitude at point  $A$  may easily be determined from the sound level at  $C-$  by the fact that the sound pressure decays inversely proportional to the distance from the source in the uniform flow. Similarly, the procedure can be applied to the microphone array to study the acoustic features of the test object. Additionally, the correction processes are classified in the current study according to their function as angle correction and amplitude correction, respectively.

### 2.3 Angle correction

The angle correction provides the relation among the measurement angle, the radiation angle and the transmission angle, from which the corresponding corrected location ( $A$ ) in a uniform flow can be determined for a known measurement position ( $M$ ). The equations are derived based on the geometrical relations of the distance and the angles, as well as the matching of phase speeds between the incident wave and the transmitted wave (trace-velocity matching principle [A. D. Pierce 1981]). Below are the correction equations applied in the open-jet wind tunnel,

$$\tan \theta_0 = \frac{\sqrt{(1 - M \cos \theta_t)^2 - \cos^2 \theta_t}}{(1 - M^2) \cos \theta_t + M} \quad (2.1)$$

$$y_M \cot \theta_M = h \cot \theta_0 + (y_M - h) \cot \theta_t \quad (2.2)$$

where  $\theta_0$  is the radiation angle,  $\theta_t$  represents the transmission angle and  $\theta_M$  indicates the measurement angle.  $M$  is the acoustic Mach number of the jet flow, which is obtained from  $U_0/a_\infty$ .  $y_M$  is the distance from the source to the microphone line and  $h$  is the distance between the source and the shear layer. Their definitions are illustrated in Fig.2.1.

These two equations can be combined to give an expression for  $\theta_0$  in terms of measurement angle  $\theta_M$  by eliminating  $\theta_t$ , in order to directly generate the corrected position. However, the current form is more concise and beneficial for the study of the properties of the equations, including the critical angles when the limiting situation is achieved, which are presented in the following sections.

### 2.3.1 Total reflection

If the sound wave meets the shear layer at such an angle that the corresponding transmitted wave goes along the shear layer at angle  $\theta_t = 0^\circ$  or  $\theta_t = 180^\circ$ , then there is not an actual transmission through the shear layer. The incident wave is perfectly reflected under such a situation, which is named as total reflection or perfect reflection. By setting  $\theta_t = 0^\circ$ , the critical radiation angle for the total reflection is generated as the wave travels in the flow direction, which can be derived from Eq.(2.1) as

$$\theta_0^{tot} = \tan^{-1} \frac{\sqrt{(1-M)^2 - 1}}{1 - M^2 + M} \quad (2.3)$$

When the  $\theta_0 \leq \theta_0^{tot}$ , the sound wave can not go through the shear layer and forms a silent area just above the shear layer. In the opposite direction, the limiting case is achieved for  $\theta_t = 180^\circ$  as the wave propagates against the flow direction. The corresponding critical radiation angle is

$$\theta_0^{tot} = \tan^{-1} \frac{\sqrt{(1+M)^2 - 1}}{M^2 + M - 1} \quad (2.4)$$

An identical phenomenon happens as in previous downstream case only except that it happens while  $\theta_0 \geq \theta_0^{tot}$ . One may notice that such a critical angle is only relevant with the open-jet flow speed (or the flow speeds at both sides of the shear layer for more general cases), but irrelevant with the distance parameters.

Regarding these expressions for the critical angle of total reflection, it is noticed in Eq.(2.3) that the total reflection only happens while  $M > 2$ , which is not the situation we are considering in the current study. Obviously, the angle indicated by Eq.(2.4) represents the limiting case that happens in the current study, which will be considered as a reference in the following numerical study.

### 2.3.2 Zone of silence

In order to investigate another characteristic of the sound wave propagation in the shear flow, a parameter needs to be mentioned, i.e. the incidence angle  $\theta_i$ . As indicated in Fig.2.2a the angle defines the orientation of the wave fronts which only corresponds to the wave propagation angle  $\theta_0$  in a medium at rest. When  $\theta_i = 0^\circ$  or  $\theta_i = 180^\circ$ , the sound wave propagates parallel to the shear layer, defining the limiting case where no sound wave transmits through the shear layer. The corresponding transmission angle  $\theta_t^s$  defines the boundary of an area where no sound wave transmits into, and the area is called the zone of silence.

Another angle relation between incident and radiation angle is added to the equation system to obtain  $\theta_t^s$ , which is established by considering the convective effect by the flow velocity on the sound propagation.

$$\tan \theta_0 = \frac{\sin \theta_i}{\cos \theta_i + M} \quad (2.5)$$

$\theta_t^s$  can be obtained by eliminating  $\theta_0$  from Eqs.(2.1) and (2.5). Then the critical angle downstream is obtained by setting  $\theta_i = 0^\circ$  as

$$\theta_t^s = \cos^{-1} \frac{1}{1 + M} \quad (2.6)$$

The area between the angle range  $0^\circ < \theta_t < \theta_t^s$  is free of sound, since any incident angle satisfies  $\theta_i > 0^\circ$  would result in a transmission angle  $\theta_t > \theta_t^s$ . Moreover, such a zone expands with the open-jet flow speed. When the sound wave hits the shear layer upstream at incidence angle  $\theta_i = 180^\circ$ , the corresponding critical transmission angle is obtained as

$$\theta_t^s = \cos^{-1} \frac{1}{M - 1} \quad (2.7)$$

According to the mathematical characteristics of cos-function, this upstream critical angle only exists as the Mach number is bigger than 2, which is not covered in the current study. Therefore, the zone of silence is only considered in the downstream propagation.

### 2.3.3 Application of the angle correction in the open-jet wind tunnel

Knowing the properties of the angle correction, this section gives a practical application of it in DLR's Aeroacoustic Wind tunnel Braunschweig(AWB), which gives a theoretical overview of the refraction effect. The nozzle of AWB is 1.2m high and 0.8m wide of rectangular shape. The free stream velocity can reach a maximum of 65m/s. The maximum flow speed under standard test conditions is up to 60m/s. A detailed introduction of AWB can be found in the reference [M. Pott-Pollenske 2008]. In the following study, three typical flow speeds in AWB are chosen to investigate the shear layer effects in the aeroacoustic wind tunnel experiments, which are 40m/s, 50m/s and 60m/s.

Generally, the test object is installed at the nozzle centerline, which indicates a source-shear layer distance  $h = 0.6m$  from the side view of the test section. The placed microphone line is chosen at the sideline  $y_M = 1.2m$  in the study, guaranteeing enough distance from the shear layer to avoid the flow induced influence. Inserting these parameters into the angle correction Eqs.(2.1) and (2.2), it is convenient to obtain the curves between the angles by iteratively solving the equations, shown in Fig.2.2.

Referring to Fig.2.2a, it provides a model of angle definitions for a quick review. Fig.2.2b gives the transmission angle variation with the radiation angle for the AWB shear flow at different flow speeds. The transmission wave angle is bigger than the radiation angle throughout the entire range, which indicates that the incident sound wave is always refracted by the shear layer to the backward direction, as shown in Fig.2.2a by solid lines. Such an alteration in the direction becomes evident with the flow speed, especially at some extreme angles. As the radiation angle approaches

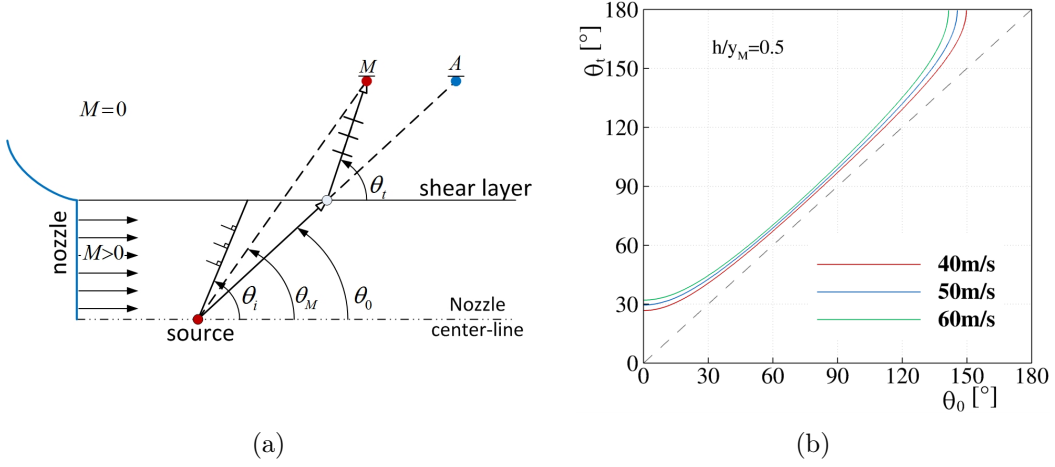


Figure 2.2: Angle relations for different flow speeds.

to  $0^\circ$ , it results in a transmission angle around  $30^\circ$ , which is the boundary of the zone of silence mentioned earlier. As the transmission angle approaches to  $180^\circ$ , its corresponding radiation angle labels the critical total reflection angle under various flow speeds. Beyond this angle, no sound wave could transmit through the shear layer. As the flow speed increases, the total reflection happens at a smaller radiation angle and the area of the zone of silence is broadened, which evidences a stronger shear layer effect at higher flow speed as expected. It should be mentioned that any microphone along the line  $y_M$  will receive a sound signal in spite of the occurrence of the total reflection and the zone of silence. Since the entire range of angles up to  $\theta_t$  is reached upstream (see Fig.2.2b) and the incidence angle  $\theta_i = 0$  does never occur due to the finite dimensions in an actual wind tunnel. However, the range of the corresponding measurable radiation angles ( $\theta_0$ ) is limited by the shear layer effects, in addition to the limitation by the geometrical obstacles of the wind tunnel (e.g. nozzle rim).

## 2.4 Amplitude correction

Providing the wave propagation path in the shear flow, the amplitude of the receiving signal at the measurement point is corrected to the value at the 'right' position in the uniform flow. Basically, the alteration of the amplitude of the acoustic perturbation results from two factors. One is the change in the propagation path length due to the deviation from the original direction. The other is the contribution from the reflection by the shear layer, which causes an energy loss into the reflected part. To correct these effects away from the measurement data, Amiet gives the following pressure amplitude ratio for measurement and corrected position.

$$\frac{\overline{p_A'^2}}{\overline{p_M'^2}} = \frac{h^2}{y_M^2} \frac{[\sin \theta_t + (y_M/h - 1)\zeta]}{\sin \theta_t} \frac{[\sin^3 \theta_t + (y_M/h - 1)\zeta^3]}{\sin^3 \theta_t} \frac{[\zeta + \sin \theta_t (1 - M \cos \theta_t)^2]}{4\zeta^2} \quad (2.8)$$

where  $\overline{p_A^2}$  and  $\overline{p_M^2}$  represent the mean square value (temporal average value of squared pressure perturbation) at point  $A$  and point  $M$  respectively.  $\zeta = [(1 - M \cos \theta_t)^2 - \cos^2 \theta_t]^{1/2}$ . Definitions of other parameters are illustrated in Fig.2.1.

The equation is easy to follow based on the aforementioned correction procedure in Sec.2.2. The ray tube spreading from cross point  $C$  to point  $M$  is indicated by the second and third term, which compensate the intensity loss in  $z$  direction and  $xy$  plane respectively. The intensity jump across the shear layer is considered by the fourth term, which is caused by the reflection by the shear layer. After recovering the energy lost, the amplitude change from point  $C$  to  $A$  is formulated by the first term. The equation given here is derived for the three-dimensional situation where the microphone-source plane is perpendicular to the planar shear layer. A more general amplitude correction equation is presented in the Appendix A, in which the lateral variation of the sound wave propagation is taken into account.

Similar to the angle correction, a deep understanding of the features of the amplitude correction is helpful for the numerical investigations, which are presented in the following section with its practical application in the AWB.

#### 2.4.1 Application of the amplitude correction in the open jet wind tunnel

Applying the geometric parameters of AWB ( $h/y_M = 0.5$ ), the amplitude correction curves can be obtained for the shear flow at various flow speeds from the previous correction equation, plotted in Fig.2.3. It should be mentioned that the second term in the equation disappears in a 2D shear layer, when also 2D wave propagation is considered since for 2D waves there is not an energy loss in  $z$  direction. The 3D curves were plotted for the situation when the source-microphones plane is perpendicular to the planar shear layer.

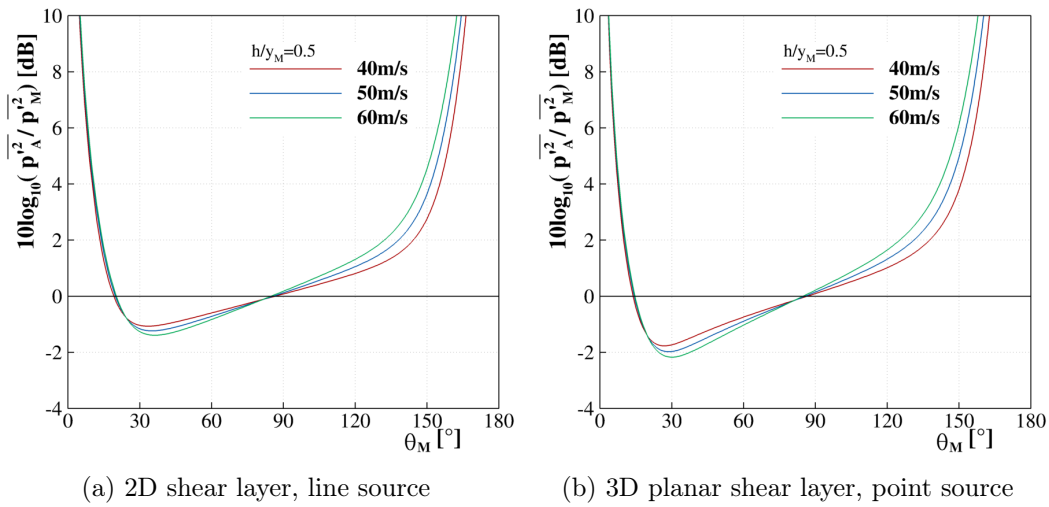


Figure 2.3: Amplitude correction at various flow speeds

Regarding the application in the wind tunnel tests, the correction curves are plotted against the measurement angle  $\theta_M$ . The  $y$  axis represents the Sound Pressure Level (SPL) difference between the pressure perturbations at point  $A$  and  $M$ , which indicates the SPL value needs to be added to or subtracted from the measurement data. In both 2D and 3D shear flow, when the sound wave propagates towards upstream ( $\theta_M > 90^\circ$ ), it experiences an energy loss due to both the path alteration and the shear flow reflection. Therefore, extra SPL needs to be added to the measurement data. When the sound wave transmits towards downstream at some angles ( $\theta_M > 20^\circ$  in 2D and  $\theta_M > 15^\circ$  in 3D), the energy variation balance between reflection and path alteration is inverted, so that the correction SPL is less than 0. There are two particular measurement angles where no correction is required ( $\overline{p_A^2}/\overline{p_M^2} = 1$ ). One is slightly smaller than  $90^\circ$ , where the receiving signal transmits across the shear layer at the incidence angle  $90^\circ$  that it does not experience any effects from the shear layer. The corresponding measurement angle is less than  $90^\circ$  because of the flow convection effect and decreases slightly with the flow speed. The other special angle around  $20^\circ$  in the 2D shear flow ( $15^\circ$  in the 3D shear flow) is formed due to the energy variation balance caused by the propagation path alteration and the shear layer reflection. The energy loss due to the reflection balances out the energy addition due to shorter propagation path after refraction at this point. Comparing the curves at the same flow speed in 2D and 3D, a bigger correction value is needed in 3D due to the additional ray tube spreading in  $z$  direction. Considering the influence of the flow speed, it is obvious that the absolute correction value increases with the flow speed for the entire measurement angle range.

## 2.5 Summary

The correction approach was briefly reviewed in this chapter. Some features of the correction equations were mentioned with their applications in the AWB, such as total reflection, the zone of silence and characteristics of the amplitude correction. In the considered situation, the total reflection happens when sound propagates against the flow beyond the critical radiation angle. A zone of silence is formed far downstream where the sound wave propagates parallelly to the shear layer. Moreover, when the sound wave meets the shear layer perpendicularly, it goes through the shear layer without any refraction or reflection. Several theoretical critical values were provided for corresponding phenomena, which can be taken as the guidance for our numerical study.



# Numerical method

---

A hybrid approach was adopted in the current study to investigate the free shear layer effects. The approach is generally conducted in three distinct phases, i.e. computational fluid dynamics(CFD), the sound generation and the sound propagation. This approach is meant to help saving considerable computational effort in comparison to direct noise computation (DNC), although its accuracy might be lower than that obtained with a DNC method. However, its accuracy is sufficient for our purpose of the sound propagation through the free shear layer, since we focus on the propagation of sound waves rather than the generation process. In this chapter, the methods employed for each phase are briefly introduced, including the CFD and CAA tools utilized in the process. Additionally, the source models are presented, followed by the definitions of some acoustic quantities used in the analysis of numerical results.

## 3.1 Introduction

The hybrid approach applied in the current study involves firstly the simulation of the open-jet wind tunnel flow field by solving the RANS equations. The work [V. Ciobaca 2009] was carried out with DLR's computational fluid dynamics tool TAU [N. Kroll 1989]. The flow through the empty anechoic chamber was simulated on an unstructured grid including parts of the nozzle and the collector for three typical flow speeds in AWB, i.e.  $40m/s$ ,  $50m/s$  and  $60m/s$ . Additionally, the flow field is provided at  $60m/s$  when a high-lift airfoil is installed in the test section in order to investigate the effect of the test model induced flow curvature. The corresponding CFD grids can resolve the open jet free shear layers fairly well. Menter's SST turbulence model was selected for the simulation of viscous effects and turbulence statistics through the free shear layers. The basic equations are discretized with a central scheme and the turbulence equations by a second order accurate upwind scheme. More details of the description of the CFD solver can be found in the reference [N. Kroll 1989].

Taking the provided shear flow as a background flow, the simulation of the acoustic propagation was conducted using DLR's computational aeroacoustic solver PIANO [J. W. Delfs 2008]. PIANO is a numerical code designed to simulate the aerodynamic noise generation and acoustic wave propagation in non-uniform flows. It is based on the equations governing the inviscid dynamics of perturbations in a given time-averaged (viscous, turbulent) mean flow field, which is appropriate for our study of the mean flow gradient effect through the shear layer in the first step.

When it comes to the study of the scattering effect through the shear layer, the unsteady fluctuations in the shear layer need to be realized and considered in the governing equations. In the present study, the unsteady turbulence is modelled with a 4D synthetic turbulence method developed at DLR[R. Ewert 2011], i.e. the Fast Random Particle Method (FRPM). The FRPM could reconstruct the turbulence with all statistical features as predicted by time-averaged RANS. It includes the convection of the synthetic eddies by the turbulent mean flow as well as the influence from the turbulence decay. A general introduction of both PIANO and FRPM are presented in the following sections, including the basic equations and the treatments of boundary conditions et.al.

## 3.2 PIANO (Perturbation Investigation of Aerodynamic Noise)

### 3.2.1 Governing Equations

As already mentioned, PIANO is able to simulate the aerodynamic sound generation and acoustic wave propagation in non-uniform flows. It is based on structured, curvilinear multi-block grids. Several types of governing equations are provided in the code, which are Linearised Euler Equations(LEE), Acoustic Perturbation Equations(APE) respectively. The unsteady linearised Euler equations were chosen to describe the generation and propagation of aeroacoustic sound in the shear flow due to its capability in supporting vorticity, entropy and pressure waves. Moreover, since the physics of the unsteady turbulent flow are captured by a corresponding CFD solver and a stochastic turbulence model, the perturbation equations are just responsible for the acoustic propagation part of the problem. Therefore, certain simplifications could be introduced into the governing acoustic equations. The non-dimensional Navier-Stokes equations for thermally and calorically perfect gas are listed as below:

$$\begin{aligned}
 \frac{\partial \rho}{\partial t} + \mathbf{v} \cdot \nabla \rho + \rho \nabla \cdot \mathbf{v} &= 0 \\
 \frac{\partial \mathbf{v}}{\partial t} + \mathbf{v} \cdot \nabla \mathbf{v} + \frac{1}{\rho} \nabla p &= \frac{M}{Re} \frac{1}{\rho} \nabla \cdot \boldsymbol{\tau} \\
 \frac{\partial p}{\partial t} + \mathbf{v} \cdot \nabla p + p \nabla \cdot \mathbf{v} &= \frac{M}{Re} \left[ (\gamma - 1) \boldsymbol{\tau} : \nabla \mathbf{v} - \frac{1}{Pr} \nabla \cdot \mathbf{q} \right]
 \end{aligned} \tag{3.1}$$

Here,  $\rho, \mathbf{v}, p$  denote density, velocity and pressure, non-dimensionalized with  $\rho_\infty, a_\infty, \rho_\infty a_\infty^2$  respectively.  $\boldsymbol{\tau}$  and  $\mathbf{q}$  represent the viscous stress and heat flux density, referenced to  $\mu_\infty U_\infty / L$  and  $k_\infty a_\infty^2 / (c_p (\gamma - 1) L)$  respectively.  $M = U_\infty / a_\infty$ ,  $Re = \rho_\infty U_\infty L / \mu_\infty$  and  $Pr$  represent the Mach-, Reynolds- and Prandtl numbers. Usually the aeroacoustic problems are characterized by small amplitude fluctuations in a steady mean flow. Therefore, the primitive variables will be written as a combination of a time-averaged steady mean-flow quantity and a fluctuation part, in which the order of the perturbation is represented by introducing a small number

$\varepsilon \ll 1$ ,

$$\rho = \rho_0 + \varepsilon\rho', \quad \mathbf{v} = \mathbf{v}_0 + \varepsilon\mathbf{v}', \quad p = p_0 + \varepsilon p' \quad (3.2)$$

In order that the quantities with subscript 0 represent a flow, they have to satisfy the steady form of Eqs.(3.1). For exterior acoustics problems perturbations in the viscous stresses and heat flux are negligible, so that  $\boldsymbol{\tau} \approx \boldsymbol{\tau}_0$  and  $\mathbf{q} \approx \mathbf{q}_0$ . After three steps i) inserting Eq.(3.2) into Eqs.(3.1), ii) differentiating with respect to  $\varepsilon$ , iii) letting  $\varepsilon \rightarrow 0$ , the equations describing the linear (inviscid) dynamics of perturbations are given as,

$$\begin{aligned} \frac{\partial \rho'}{\partial t} + \mathbf{v}' \cdot \nabla \rho_0 + \mathbf{v}_0 \cdot \nabla \rho' + \rho' \nabla \cdot \mathbf{v}_0 + \rho_0 \nabla \cdot \mathbf{v}' &= 0 \\ \frac{\partial \mathbf{v}'}{\partial t} + \mathbf{v}' \cdot \nabla \mathbf{v}_0 + \mathbf{v}_0 \cdot \nabla \mathbf{v}' + \frac{1}{\rho_0} \nabla p' + \frac{\rho'}{\rho_0} \mathbf{v}_0 \cdot \nabla \mathbf{v}_0 &= 0 \\ \frac{\partial p'}{\partial t} + \mathbf{v}' \cdot \nabla p_0 + \mathbf{v}_0 \cdot \nabla p' + \gamma (p' \nabla \cdot \mathbf{v}_0 + p_0 \nabla \cdot \mathbf{v}') &= 0 \end{aligned} \quad (3.3)$$

Eqs.(3.3) are solved for  $(\rho', \mathbf{v}', p')$  for a given mean flow field with  $\rho_0, \mathbf{v}_0, p_0$  to simulate the corresponding acoustic field. Since practical problems require treatments on various curved boundaries and grids, the basic equations are transformed into a curvilinear coordinate system.

### 3.2.2 Numerical algorithm

Similar as in the CFD simulations introduced in the first section, spatial discretization and time integration are essential parts in the numerical solver. The differential equations are solved numerically in DLR's inhouse code PIANO on a curvilinear block structured mesh. The high-resolution spatial discretization is carried out based on the dispersion relation preserving (DRP) scheme of Tam and Webb [C. Tam 1993]. The scheme ensures to minimize the numerical dispersion introduced by the discretization for a given wavenumber range. The order of the accuracy is reduced for the spatial discretization from 6th to 4th order as a payment. A symmetric 7-point stencil is used in PIANO to approach the first derivative numerically except at boundaries, where an unsymmetric 7-point stencil is applied alternatively. The procedure with given DRP-coefficients ensures the 4th-order accuracy of the spatial discretization. The first derivative on a uniform grid is written as

$$\frac{\partial \phi}{\partial x} \Big|_i = \frac{1}{\Delta x} \sum_{l=-3}^3 c_l \phi_{i+l} \quad (3.4)$$

where  $\Delta x$  is the grid spacing,  $c_l$  is the coefficient for 7-point stencils, whose value can be found in the reference [J. W. Delfs 2008].

The temporal discretization is implemented with a 4th order Runge-Kutta scheme. A two-step low-dissipation, low-dispersion Runge-Kutta (LDDRK) algorithm proposed by Hu [F. Q. Hu 1996] is employed to minimize the dissipation and dispersion errors for the wave propagation. The coefficients are chosen to minimize the dissipation and dispersion errors without compromising the stability limits.

### 3.2.3 Boundary conditions

As another key factor in the numerical simulation, boundary condition plays an important role in the CAA simulation as well. When the boundary condition is used to introduce the sound wave into the computation domain, it should ensure that the wave is correctly brought into the domain without distortion or characteristic alteration. When the boundary condition is applied to let the wave radiate away from the domain, it should minimize the reflection at the boundary. Considering the specified problem in the current study, suitable boundary conditions are chosen for each case.

**Radiation boundary condition** [C. Tam 1993] is applied at bounding grid surfaces, where there are only outgoing acoustic waves. The equation is formulated as

$$\left( \frac{1}{V(\Theta)} \frac{\partial}{\partial t} + \frac{\partial}{\partial r} + \frac{1}{rc_{2D}} \right) \begin{pmatrix} \rho' \\ u' \\ v' \\ w' \\ p' \end{pmatrix} = 0 \quad (3.5)$$

where  $V(\Theta) = |\mathbf{v}_0| \cos \Theta + \sqrt{a_0^2 - |\mathbf{v}_0|^2 \sin^2 \Theta}$ .  $c_{2D}$  is a dimensional coefficient, which equals to 2 in 2D and equals to 1 for three dimensional simulation.  $a_0$  is the local sound speed, calculated from  $\sqrt{\gamma p_0 / \rho_0}$ .  $r = |\mathbf{x} - \mathbf{x}_{\text{ref}}|$  is measured from the center of acoustic sources. The angle  $\Theta = \arccos(\mathbf{r} \cdot \mathbf{v}_0 / |\mathbf{r}| |\mathbf{v}_0|)$ , while  $\mathbf{r}$  represents the distance vector from the boundary point to a reference point typically in the center of the computation domain.

**Slip Wall boundary condition** is implemented combined with the adiabatic condition on the grid blocks where the geometry of the open jet nozzle surface is included. The surfaces are considered acoustically hard. The ghost point concept from Tam and Dong [C. Tam 1994] is adopted, which introduces an additional computational node beyond the wall (located inside the body). The pressure value at the ghost point is evaluated such that the non-penetration condition is satisfied at the boundary.

$$\mathbf{n} \cdot \mathbf{v} = 0 \quad (3.6)$$

where  $\mathbf{n}$  is the normal vector of the surface. A relation for the pressure at the ghost point can be yielded by multiplying the momentum equation with the normal vector  $\mathbf{n}$

$$\rho v_i \frac{\partial v_j}{\partial x_i} n_j + n_j \frac{\partial p}{\partial x_j} = 0 \quad (3.7)$$

Analogy to the derivation of the governing equation, the linearized form of the equation can be written as

$$\frac{\partial p'}{\partial n} = n_j \frac{\partial p'}{\partial x_j} = -n_j \left\{ \frac{\partial v_j^0}{\partial x_i} (\rho' v_i^0 + \rho_0 v_i') + \frac{\partial v_j'}{\partial x_i} \rho_0 v_i^0 \right\} \quad (3.8)$$

The value of  $p'$  is evaluated at the ghost point so that Eq.(3.8) is satisfied. Finally, the density  $\rho'$  is determined by the adiabatic condition  $\rho' = p'/a_0^2$ .

**Sponge layer boundary condition** is adopted in several different ways in the study to satisfy the specific requirements. Generally, the sponge layer approach can enforce a given function in the specified layers along the boundary. It subtracts a supplement term from the right hand side from the LEE equations in the curvilinear coordinate system. The variation of the term is capable of realizing different functions to be used for the boundaries. Its general form is written as

$$Q = \sigma(\xi)(\phi' - \phi_{\text{ref}})$$

where  $\sigma(\xi)$  is a fading function which is subject to the distance to the boundary.  $\phi'$  represents the various perturbation quantities and  $\phi_{\text{ref}}$  is its respective forcing function term. Two types of  $\phi_{\text{ref}}$  are applied in the current study. Firstly, it is used to introduce the sound wave located outside of the computation domain into the domain. Such a setting can help to avoid the possible singularity problem if a perfect point source is to be represented directly inside the domain. Therefore, the form of the forcing function  $\phi_{\text{ref}}$  is relevant to the employed source model, which will be introduced in the next section. The second form of the sponge layer is used as a 'sponge' to absorb the outgoing wave in some specific area to eliminate the reflection from the boundary. Since we have a more confined domain than the real wind tunnel, some reflections do not happen in the experiment but may potentially arise in the simulation. An absorbing sponge layer is necessary to avoid the corresponding effects caused by the reflected wave. More details about the definition of forcing function and its coefficients can be found in the reference [J. W. Delfs 2008].

### 3.2.4 Sound source model

Since we aim at figuring out the shear layer effects on the sound propagation at various frequencies, a tonal source is suitable for the study. This selection also results from the fact that the scattering effect is not obvious for the broadband noise according to the previous studies by [S. Candel 1975] [R. H. Schlinker 1980]. For the broadband noise, the energy loss due to the turbulence scattering at one single frequency will drain into other neighbouring frequency bands by the turbulence scattering process. Therefore, two periodic sources were utilized to generate single frequency sound waves in 2D and 3D respectively. The third source model, a non-periodic pressure pulse, was taken as a complementary source model for validations under some particular situations to support the results from the former models.

#### Harmonic source (2D)[J. W. Delfs 2014]

A 2D harmonic source is employed to investigate the sound propagation characteristics in two dimensional shear flow at specified frequencies. Assuming a non-moving harmonic line mass or heat source located at point  $\xi_0$  in a uniform flow of Mach number  $M$ , its acoustic field produced by  $\frac{D_\infty \hat{\theta}'}{Dt}$  with  $\hat{\theta}' = \hat{\theta}_p \exp(i\omega t)\delta(\mathbf{x} - \xi_0)$

in two-dimension is

$$p'(\mathbf{x}, t) = \frac{\omega \hat{\theta}_p}{4\sqrt{1-M^2}^3} \left\{ \left[ J_0(kr_0^*) + \frac{r_0 M_r}{r_0^*(1-M^2)} Y_1(kr_0^*) \right] \cos\left(\omega t + kr_0 \frac{M_r}{1-M^2}\right) + \left[ Y_0(kr_0^*) - \frac{r_0 M_r}{r_0^*(1-M^2)} J_1(kr_0^*) \right] \sin\left(\omega t + kr_0 \frac{M_r}{1-M^2}\right) \right\} \quad (3.9)$$

where  $r_0^* = r_0 \sqrt{1-M^2 + M_r^2} / (1-M^2)$ , in which  $r_0 = |\mathbf{r}_0|$  with  $\mathbf{r}_0 = \mathbf{x} - \boldsymbol{\xi}_0$  and  $M_r = \mathbf{r}_0 \cdot \mathbf{M} / r_0$  while  $\mathbf{e}_r = \mathbf{r}_0 / r_0$ .  $\mathbf{M}$  is the local acoustic Mach number, defined as  $\mathbf{M} = \mathbf{U} / a_0$ . The expressions of perturbations  $\rho'$ ,  $\mathbf{v}'$  can be found in the reference [J. W. Delfs 2014].

#### Point mass or heat source in subsonic flow (3D)

A three dimensional point source (not necessarily harmonic in time) is taken as the acoustic source terms in 3D simulation, whose form is  $Q_p = \frac{D_\infty \dot{\theta}'}{Dt}$ . The non-moving source  $\dot{\theta}'$  is assumed to be located at point  $\boldsymbol{\xi}_0$  in a uniform flow with speed  $\mathbf{U}_0$ . The speed of sound and the density of the medium are assumed uniform as well. The source can be described as  $\dot{\theta}'(\boldsymbol{\xi}, \tau) = \delta(\boldsymbol{\xi} - \boldsymbol{\xi}_0) \theta_p(\tau)$ , where  $\theta_p(\tau)$  denotes the temporal variation of the source. The sound field as a solution to the convected wave equation can be written down according to the Green's function method. The final expression of the pressure perturbation yields

$$p'(\mathbf{x}, t) = -\frac{a_0 M_r r_0}{4\pi r_0^{*3} (1-M^2)^3} \theta_p \Big|_{t-r_0^+/a_\infty} + \frac{r_0^+}{4\pi r_0^{*2} (1-M^2)^2} \frac{\partial \theta_p}{\partial t} \Big|_{t-r_0^+/a_\infty} \quad (3.10)$$

where  $r_0^+ = [(1-M^2)r_0^* - M_r r_0] / (1-M^2)$ . The first term represents a directed near field, which decays fast like  $r_0^{-2}$ . The farfield term (the term decaying slowly like  $r_0^{-1}$ ) is directed by the flow as well, which will be observed in the following numerical results. A detailed derivation process and the analysis of the source directivity could be found in the reference [J. W. Delfs 2014].

#### Pressure pulse (2D)

The source is a Gaussian distributed non-periodic pulse source. The initial distribution of the variables are based on Gaussian functions, as

$$p'(\mathbf{x}, 0) = p_{\max} \exp \left[ -\ln 2 \frac{(\mathbf{x} - \mathbf{x}^c)^2}{b^2} \right] \quad (3.11)$$

where  $p_{\max}$  is the magnitude of the pressure pulse,  $\mathbf{x}^c$  is the coordinate of the source location,  $b$  represents the half-value radius of Gaussian. The density fluctuation is initialised according to isentropy via  $\rho' = p' / a_\infty^2$ .

### 3.3 Reconstruction of the turbulence (FRPM method)

In order to study the scattering effect induced by the turbulence in the free shear layer with the CAA method, the unsteady turbulent fluctuations are modelled with

a 4D synthetic turbulence method. The averaged turbulence field provided by the RANS simulation is used as the basis for the realization of the unsteady turbulent characteristics in the FRPM method. The resulting turbulent field expresses all the local statistical features as provided by the RANS simulation and is coupled into the sound propagation equations as additional time dependent parameters. The time-averaged mean flow is indicated by a steady state RANS solution, while the additional terms from turbulent fluctuations are modelled using the turbulent kinetic energy and length scales from the RANS solution. The scattering of the tonal waves is then resolved by the CAA simulations such that its effect can be studied numerically.

### 3.3.1 Governing equations

Before presenting the method for the realization of the turbulent fluctuations, some modifications need to be carried out for the governing equations in advance. Due to the participation of the turbulence part in the free shear layer, the original governing equations shown in Sec.3.2.1 are not suitable for the simulation any more. Their expressions vary slightly as the turbulence part is added. The part of the description of governing equations is actually included in the PIANO code, which is presented here to give a consistent view of the methodology of the numerical realization of the scattering effect.

The governing equations are in a similar form as in the previous derivation, but with turbulent fluctuations as additional time dependent parameters. The same derivation procedure is taken here as before. The primitive variables  $\rho'$ ,  $\mathbf{v}'$ ,  $p'$  indicate the acoustic perturbations as usual, but the base flow here is an unsteady fluctuating flow  $\rho$ ,  $\mathbf{v}$ ,  $p$ . By neglecting non-linear terms and viscous perturbations as before, it shows that the perturbations satisfy equations that are similar to the LEE, but with the steady mean flow  $\rho_0$ ,  $\mathbf{v}_0$ ,  $p_0$  replaced by the unsteady base flow  $\rho$ ,  $\mathbf{v}$ ,  $p$ . The linearized equations for the perturbations in the unsteady base flow are

$$\begin{aligned} \frac{\partial \rho'}{\partial t} + \mathbf{v} \cdot \nabla \rho' + \mathbf{v}' \cdot \nabla \rho + \rho \nabla \cdot \mathbf{v}' + \rho' \nabla \cdot \mathbf{v} &= 0 \\ \frac{\partial \mathbf{v}'}{\partial t} + (\mathbf{v} \cdot \nabla) \mathbf{v}' + (\mathbf{v}' \cdot \nabla) \mathbf{v} + \frac{\nabla p'}{\rho} - \frac{\nabla p p'}{\rho^2} &= \mathbf{0} \\ \frac{\partial p'}{\partial t} + \mathbf{v} \cdot \nabla p' + \mathbf{v}' \cdot \nabla p + \gamma p \nabla \cdot \mathbf{v}' + \gamma p' \nabla \cdot \mathbf{v} &= 0 \end{aligned} \quad (3.12)$$

Then the unsteady base flow is decomposed into a time-averaged part (with subscript  $\theta$  as before) and a turbulent fluctuating part (with subscript  $t$ ) as

$$\varphi(\mathbf{x}, t) = \varphi_0(\mathbf{x}) + \varphi_t(\mathbf{x}, t) \quad (3.13)$$

where  $\varphi$  represents the flow quantities  $(\rho, \mathbf{v}, p)$ . Inserting the decomposition into

Eq.(3.12), the perturbation equations can be rewritten as

$$\begin{aligned}
\frac{\partial \rho'}{\partial t} + \mathbf{v}_0 \cdot \nabla \rho' + \rho_0 \nabla \cdot \mathbf{v}' + \mathbf{v}' \cdot \nabla \rho_0 + \rho' \nabla \cdot \mathbf{v}_0 + H_1 &= 0 \\
\frac{\partial \mathbf{v}'}{\partial t} + (\mathbf{v}_0 \cdot \nabla) \mathbf{v}' + \frac{\nabla p'}{\rho_0} + (\mathbf{v}' \cdot \nabla) \mathbf{v}_0 - \frac{\nabla p_0 \rho'}{\rho_0^2} + \mathbf{H}_2 &= \mathbf{0} \\
\frac{\partial p'}{\partial t} + \mathbf{v}_0 \cdot \nabla p' + \gamma p_0 \nabla \cdot \mathbf{v}' + \mathbf{v}' \cdot \nabla p_0 + \gamma p' \nabla \cdot \mathbf{v}_0 + H_3 &= 0
\end{aligned} \tag{3.14}$$

The form of the equations on the left hand side is identical to the LEE applied for steady base flow but with addition of extra terms  $H_1, \mathbf{H}_2, H_3$ . These terms represent the interaction between the acoustic and turbulent quantities. The interaction terms up to the first order in the perturbations are

$$\begin{aligned}
H_1 &= \mathbf{v}_t \cdot \nabla \rho' + \mathbf{v}' \cdot \nabla \rho_t + \rho_t \nabla \cdot \mathbf{v}' + \rho' \nabla \cdot \mathbf{v}_t \\
\mathbf{H}_2 &= (\mathbf{v}_t \cdot \nabla) \mathbf{v}' + (\mathbf{v}' \cdot \nabla) \mathbf{v}_t + 2 \frac{\nabla p_0}{\rho_0^3} \rho' \rho_t - \frac{\nabla p_t \rho'}{\rho_0^2} + \frac{\nabla p' \cdot \rho_t}{\rho_0^2} \\
H_3 &= \mathbf{v}_t \cdot \nabla p' + \mathbf{v}' \cdot \nabla p_t + \gamma p_t \nabla \cdot \mathbf{v}' + \gamma p' \nabla \cdot \mathbf{v}_t
\end{aligned} \tag{3.15}$$

It should be mentioned that Eq.(3.12) form homogeneous equations and that these terms only describe the interaction, they do not introduce additional sound sources, which is extremely important. Since the study focuses on the scattering effects due to the turbulence fluctuations in the base flow rather than the sound generation, the turbulence generated noise is neglected. Besides, an assumption is made for the CAA simulations that the scattering is mainly caused by the unsteady turbulent velocities, as the effect due to turbulent pressure and density fluctuations are negligible. This assumption is reasonable for the scattering simulation in a cold jet, such as the situation in the current study. In fact, the importance of this neglect has been estimated by modelling the  $p_t$  on the basis of a local linearized Bernoulli equation as  $p_t \simeq -\rho \mathbf{v}_0 \cdot \mathbf{v}_t$ . As shown subsequently in Sec.4.4.5, the inclusion of  $p_t$  is of minor importance. Moreover, the turbulent velocities are assumed (and consequently modelled) to be solenoidal, i.e.  $\nabla \cdot \mathbf{v}_t = 0$ . According to these assumptions, the interaction terms have the final forms as below

$$\begin{aligned}
H_1 &= \mathbf{v}_t \cdot \nabla \rho' \\
\mathbf{H}_2 &= (\mathbf{v}_t \cdot \nabla) \mathbf{v}' + (\mathbf{v}' \cdot \nabla) \mathbf{v}_t \\
H_3 &= \mathbf{v}_t \cdot \nabla p'
\end{aligned} \tag{3.16}$$

Finally, the Eq.(3.14) with Eq.(3.16) compose the governing equations solved numerically for the scattering effect study.

### 3.3.2 Modeling of turbulent velocities (FRPM method)

The computation of the turbulent velocities ( $\mathbf{v}_t$ ) in the governing equations is conducted by the employment of the Fast Random Particle Mesh (FRPM) method. The method has already been applied in the previous work [R. Ewert 2007,

[R. Ewert 2009, R. Ewert 2011], which illustrates its good performance in the aeroacoustic applications. Its theoretical background is briefly presented in this section. A detailed description is included in the references [R. Ewert 2007, R. Ewert 2011].

The FRPM method realizes the time-dependent turbulent fluctuations synthetically from averaged turbulence statistics of the steady state RANS computation, i.e. local turbulence kinetic energy, length scale and time scale information. Considering the aforementioned governing equations for the simulation of scattering effect, the turbulent velocities are of concern in the modeling process. They are deduced from a fluctuating stream function by  $\mathbf{v}_t = \nabla \times \boldsymbol{\psi}$  with two zero components as  $\boldsymbol{\psi} = (0, 0, \psi_3(\mathbf{x}, t))^T$  in 2D. In 3D case they are deduced from a fluctuating stream function  $\boldsymbol{\psi} = (\psi_1(\mathbf{x}, t), \psi_2(\mathbf{x}, t), \psi_3(\mathbf{x}, t))^T$ , in which all the components are uncorrelated. Subsequently, the generation of the fluctuating stream function is presented.

Analytically, the fluctuating component  $\psi_i$  is generated by the convolution of a spatial white noise field  $\mathcal{U}_i$  with a filter kernel,

$$\psi_i(\mathbf{x}, t) = \int_{V_s^n} \hat{A}G(\mathbf{x} - \mathbf{x}')\mathcal{U}_i(\mathbf{x}', t)d^n x' \quad (3.17)$$

where  $G$  is the spatial filter kernel,  $n$  is the dimension of the problem, and  $V_s^n$  indicates the source region, which is usually represented by a sub-domain of the resolved CAA domain, named as 'patch' in the simulations.  $\hat{A}$  is a scaling function to realize the desired variance of  $\psi_i$ , which could be a function of either  $\mathbf{x}$  or  $\mathbf{x}'$ .

If a frozen turbulence field is realized,  $m$  ( $m$  depends on the dimension of the problem) mutually uncorrelated spatiotemporal white noise fields  $\mathcal{U}_i(\mathbf{x}, t)$  need to be adopted, which are defined by

$$\langle \mathcal{U}_i(\mathbf{x}, t) \rangle = 0 \quad (3.18)$$

$$\langle \mathcal{U}_i(\mathbf{x}, t)\mathcal{U}_j(\mathbf{x} + \mathbf{r}, t) \rangle = \rho_0(\mathbf{x})^{-1}\delta_{ij}\delta(\mathbf{r}) \quad (3.19)$$

$$\frac{D_0}{Dt}\mathcal{U}_i = 0 \quad (3.20)$$

where  $\langle \dots \rangle$  denotes the ensemble average.  $D_0/Dt = \partial/\partial t + \mathbf{v}_0 \cdot \nabla$  is a substantial derivative, by which the convection property is introduced into the fluctuation model through the convection of the white-noise field in a velocity field  $\mathbf{v}_0$ .  $\delta(\mathbf{r})$  is the Dirac delta function,  $\delta_{ij}$  is the Kronecker symbol. The density  $\rho_0$  follows from the conservation of mass with the steady velocity field  $\mathbf{v}_0$ , i.e.  $\nabla \cdot (\rho_0 \mathbf{v}_0) = 0$ .

Eq.(3.20) specifies the property of  $\mathcal{U}_i$  to be locally frozen if the observer drifts with the mean flow at velocity  $\mathbf{v}_0$ . If an exponential decay of turbulence needs to be achieved, each spatial white-noise field  $\mathcal{U}_i$  is modified with a Langevin equation [S. B. Pope 2000],

$$\frac{D_0}{Dt}\mathcal{U}_i = -\frac{1}{\tau_s}\mathcal{U}_i + \sqrt{\frac{2}{\tau_s}}\xi_i \quad (3.21)$$

in which  $\tau_s$  is the correlation time scale,  $\xi_i(\mathbf{x}, t)$  is a source term associated to

each realized field  $\mathcal{U}_i$ . It is defined by

$$\langle \xi_i(\mathbf{x}, t) \rangle = 0 \quad (3.22)$$

$$\langle \xi_i(\mathbf{x}, t) \xi_j(\mathbf{x} + \mathbf{r}, t) \rangle = \rho_0(\mathbf{x})^{-1} \delta_{ij} \delta(\mathbf{r}) \quad (3.23)$$

For sufficiently small two-point spatial and temporal separations  $\mathbf{r}$  and  $\tau$ , the Eqs.(3.19) and (3.21) can be written in a compact form as

$$\langle \mathcal{U}_i(\mathbf{x}, t) \mathcal{U}_j(\mathbf{x} + \mathbf{r}, t + \tau) \rangle = \rho_0^{-1}(\mathbf{x}) \delta(\mathbf{r} - \mathbf{v}_0 \tau) \exp\left(-\frac{|\tau|}{\tau_s}\right) \delta_{ij} \quad (3.24)$$

From Eq.(3.17), the cross-covariance of quantity  $\psi_i$  is derived as

$$\begin{aligned} \mathcal{R}_{ij}(\mathbf{x}, \mathbf{r}, \tau) &= \langle \psi_i(\mathbf{x}, t) \psi_j(\mathbf{x} + \mathbf{r}, t + \tau) \rangle \\ &= \hat{A}(\mathbf{x}) \hat{A}(\mathbf{x} + \mathbf{r}) \iint G(\mathbf{x} - \mathbf{x}') G(\mathbf{x} + \mathbf{r} - \mathbf{x}'') \langle \mathcal{U}_i(\mathbf{x}', t) \mathcal{U}_j(\mathbf{x}'', t + \tau) \rangle d^n x' d^n x'' \end{aligned} \quad (3.25)$$

Inserting Eq.(3.24) into the above equation, applying a Gaussian filter kernel

$$G(\mathbf{x} - \mathbf{x}') = \exp\left(-\frac{\pi |\mathbf{x} - \mathbf{x}'|^2}{2 l_s^2}\right) \quad (3.26)$$

and an incompressible convection field, as well as constant time and length scale  $\tau_s$  and  $l_s$ , the cross-covariance becomes

$$\mathcal{R}_{ij}(\mathbf{x}, \mathbf{r}, \tau) = \frac{\hat{A}(\mathbf{x}) \hat{A}(\mathbf{x} + \mathbf{r})}{\rho_0} l_s^n \exp\left(-\frac{|\tau|}{\tau_s} - \frac{\pi |\mathbf{r} - \mathbf{v}_0 \tau|^2}{4 l_s^2}\right) \delta_{ij} \quad (3.27)$$

which means that the fluctuation components  $\psi_i$  are uncorrelated. From the cross-covariance the variance of the fluctuations can be derived as

$$\hat{R} = \langle \psi(\mathbf{x}, t)^2 \rangle = \mathcal{R}_{ij}(\mathbf{x}, 0, 0) = \frac{\hat{A}^2(\mathbf{x}) l_s^n}{\rho_0} \quad (3.28)$$

Then, the definition of  $\hat{A}$  can be determined for a prescribed source variance  $\hat{R}$  as

$$\hat{A}(\mathbf{x}) = \sqrt{\frac{\rho_0 \hat{R}}{l_s^n}} \quad (3.29)$$

Here the amplitude of  $\hat{A}$  is defined as a function of position  $\mathbf{x}$ . It could be also defined as a function of  $\mathbf{x}'$ , which will result in an effectively realized variance instead of exactly the target variance  $\hat{R}$ .

The FRPM approach is conducted on a Cartesian background mesh, i.e. the aforementioned 'patch'. Numerous particles loaded with random numbers are evenly distributed over the mesh to approximate the white-noise field  $\mathcal{U}$ . These particles drift with the local mean flow velocity. In this way, the approach generates velocity

fluctuations, which very accurately resolve the local RANS statistics. It means that the effect of turbulence in the shear layer with locally varying length and time scales can be realized for the scattering effect study. Additionally, both frozen turbulence (refer to Eq.(3.20)) and an exponential temporal decay of turbulence (refer to Eq.(3.21)) are considered to evaluate their influences on the scattering effect.

### 3.4 Acoustic quantities

This section presents some acoustic quantities applied in the following chapter. They are utilized in both theoretical correction and analysis of the numerical results. Following are their definitions.

The **Sound Pressure Level** is the most common quantity used in the acoustic area. It is usually written in the abbreviation form SPL, which is defined as

$$L_p := 10 \lg \left( \frac{\tilde{p}}{p_{\text{ref}}} \right)^2 \text{ dB} = 20 \lg \left( \frac{\tilde{p}}{p_{\text{ref}}} \right) \text{ dB} \quad (3.30)$$

where  $p_{\text{ref}} = 2 \cdot 10^{-5} \text{ Pa}$ ,  $\tilde{p}$  is the root mean square value of the sound pressure. The quantity is used to calculate the SPL deviation between the measurement and corrected positions in the study, in which the parameter in the bracket in the above equation is replaced by the pressure ratio of Eq.(2.8). The directivity of the sound source in the shear flow is shown in SPL as well.

The **Sound Intensity  $\mathbf{I}$**  in a potential flow [M.K. Myers 1986] is defined as

$$\mathbf{I} := \overline{(\mathbf{v}' + \frac{\rho'}{\rho_0} \mathbf{v}_0)(p' + \rho_0 \mathbf{v}_0 \cdot \mathbf{v}')} = \overline{(\mathbf{v}' + \frac{p'}{\rho_0 a_0^2} \mathbf{v}_0)(p' + \rho_0 \mathbf{v}_0 \cdot \mathbf{v}')} \quad (3.31)$$

If the flow medium is at rest, the expression reduces to the classical definition of sound intensity  $\mathbf{I} := \overline{p' \mathbf{v}'}$ . The mean flow and the perturbation are assumed to be free of vorticity, which means that the conservation of the acoustic quantity in general fields is not guaranteed. Sound power could get lost in a shear flow due to the conversion of sound into vortices or be generated when sound waves interact with the vortical flow. In the current study, the sound vector field is used to trace the propagation direction of the sound power, which is helpful in the interpretation of the effects caused by the shear layer, especially in the study of the mean flow gradient effect.

The **Sound Intensity Level** is defined by

$$L_I := 10 \lg \left( \frac{|\mathbf{I}|}{I_{\text{ref}}} \right) \text{ dB} \quad (3.32)$$

where  $I_{\text{ref}} = 10^{-12} \text{ W/m}^2$ .



# Numerical Results

---

This chapter presents the numerical results of the CAA simulations, which consider separately the mean flow gradient and the turbulence effects by the free shear layer on the sound propagation. The study is firstly carried out on the influences brought by the mean flow gradient, which is started from two-dimensional (2D) simulations then further extended to three-dimensions (3D). As the starting point in the 2D study, the sound propagation characteristics is investigated in the analytically defined shear flow with linear velocity profile, which is followed by that in the 2D shear flow of the wind tunnel with an empty test section (Sec.4.1). Next, in view of a typical measurement situation, the AWB wind tunnel shear flow is considered which forms if a high-lift airfoil is installed in the test section of the wind tunnel. In this case the wind tunnel jet flow is deflected and its effect on Amiet's correction is assessed (Sec.4.2). Simultaneously, the reflection effect from the nozzle geometry is analyzed for these conditions. In the 3D study, the sound propagation in both planar shear layer and real AWB wind tunnel shear layer (shaped as the open-jet geometry) is considered and compared at various flow speeds (Sec.4.3).

Finally, the turbulence fluctuations in the free shear layer are taken into account to investigate their influences on the sound propagation in 2D (Sec.4.4) and 3D (Sec.4.5) flows.

## 4.1 Sound propagation through analytical shear layers (2D)

### 4.1.1 Computational setup

The 2D simulations were taken as a start since it could provide both a basic view of the shear layer effects and general characteristics of the sound propagation field in the presence of a shear layer, although it might be less helpful for the practical application than 3D simulation in the wind tunnel corrections. Moreover, the performance of the numerical code can be verified under such a relatively simple situation.

The simulations were begun with the sound propagation in analytically defined shear flows featuring by linear velocity profiles and constant shear layer thickness, of which the shear layer thickness varies from  $0.1m$  to  $0.5m$ ,  $0.2m$  per step. The core velocity  $60m/s$  was chosen for the linear shear flow cases since it is the typically highest test flow speed in the AWB while the shear layer exerts the strongest influence on sound wave transmission. The computation domain of such a shear flow is

Table 4.1: Conditions for shear layer mean flow gradient effects (2D).

shear layer type	flow speed ( $m/s$ )	domain size ( $m \times m$ )	source frequency ( $kHz$ )	angle range $\theta_M$ ( $^\circ$ )
constant	60	$10 \times 2.1$	1, 5, 10	15~165
spreading	40, 50, 60	$3 \times 2.1$	1, 5, 10	45~145

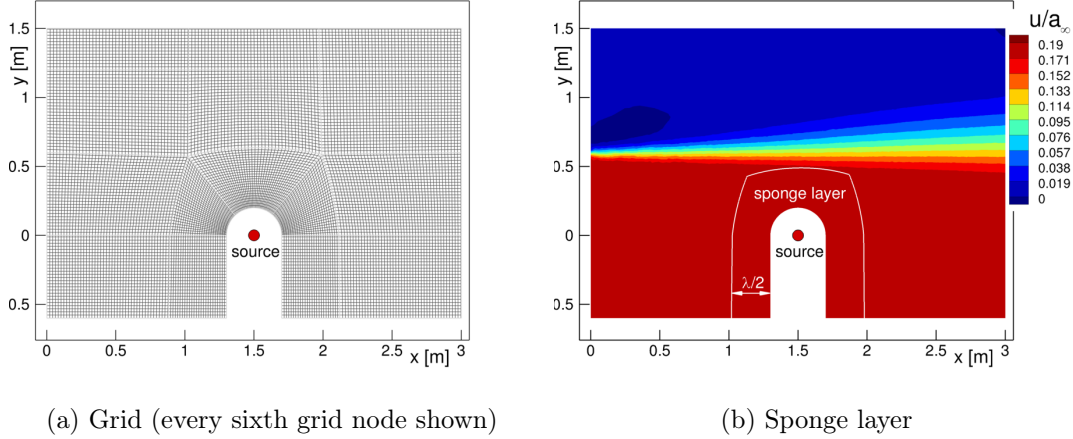


Figure 4.1: Computational grid for 2D simulations and sketch of the sponge layer.

not limited by the test section size as that in the open-jet wind tunnel, such that the domain size can be defined as required. This is quite helpful in the investigation of the refraction phenomenon at the critical angles, e.g. total reflection and zone of silence. This analysis is followed by simulations conducted for the relevant 2D slice through the actual AWB wind tunnel flow, which features a spreading shear layer whose thickness increases as the flow goes downstream. The background shear flow was provided [V. Ciobaca 2009] at three typical flow speeds in the AWB, which are  $40m/s$ ,  $50m/s$  and  $60m/s$ . Furthermore, three source frequencies were chosen to figure out the sound field features as the shear layer thickness-to-wavelength ratio ( $\delta/\lambda$ ) increases. The basic settings are listed in Tab.4.1. As shown, the computation domain size for the spreading shear flow is limited to a smaller range in the flow direction due to the test section size.

To exclude the possible effect due to the alteration in the density or the blocking strategy of the CAA grid, two identically structured grids were generated for the simulations in the analytically defined shear flow and the wind tunnel shear flow respectively. Both of them have a resolution of 7 nodes per wavelength at  $10kHz$  in both axial and vertical directions. Fig.4.1a illustrates the grid generated for simulations in the wind tunnel shear flow (spreading shear layer). The grid for the simulations of the constant thickness shear layers is just an extension of the one in Fig.4.1a in the axial direction. The source is located at  $(1.5m, 0)$  in the former case (spreading layer) and at  $(5m, 0)$  in the latter case on the nozzle centerline, while the  $y = 0$  line corresponds to the nozzle centerline in the AWB. The domain is extended

in  $y$  direction to  $y = -0.6m$  to eliminate the reflection by the bottom boundaries since it was noticed that the sound wave reflection induced by the boundary condition may interfere the total reflection occurring upstream. The coordinate of the (upper) nozzle lip-line is  $y = 0.6m$ , which was taken as the shear layer centerline in Amiet's correction model.  $y = 1.2m$  was defined as the microphone line, where several microphones were placed outside the shear layer. It assures sufficient distance away from the shear layer even when the thickest shear layer is considered.

The arc structure of the grid surrounding the source point was adopted for the sponge layer boundary condition, whose sketch is shown in Fig.4.1b on top of the horizontal velocity distribution for spreading shear layer at  $U_0 = 60m/s$ . The white curve indicates the extent and the shape of the sponge layer. Here, the sponge layer is used to introduce the sound wave from outside into the domain, which has the advantage of avoiding the singularity problem that occurs if the (analytical point) source is placed inside the domain. Details of the sponge layer condition have already been presented in the previous chapter, in which a factor  $\sigma(\xi)$  was mentioned for the controlling of its thickness. The thickness in the current study was always chosen as half of the wavelength at  $1kHz$ , which guaranteed that the sound wave is well brought into the domain without distortion at all applied frequencies. Fig.4.2 gives the instantaneous pressure field in an uniform flow as the resulted example of the computational setup. The analytical source field is smoothly brought into the domain, and there is no spurious reflections occurring at the boundaries.

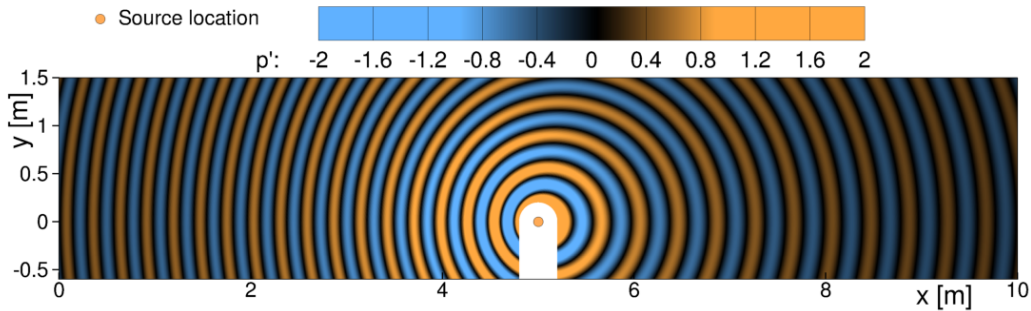


Figure 4.2: Instantaneous pressure perturbation field in the uniform flow ( $U_0 = 60m/s$ ).

#### 4.1.2 Characteristics of the base flow

Before looking at the aeroacoustic computation results, some aerodynamic features of the shear flow need to be introduced. Definitions of some parameters are presented for the shear layer characteristics, which is quite important in the following analysis of the computational data.

One of the shear layer characteristics is the shear layer thickness  $\delta$ , which is an important factor considered in the current study. The thickness of the analytically defined shear layer is easy to be determined by the length of the segment where the velocity profile is linearly distributed, as shown in Fig.4.3a. The linear velocity

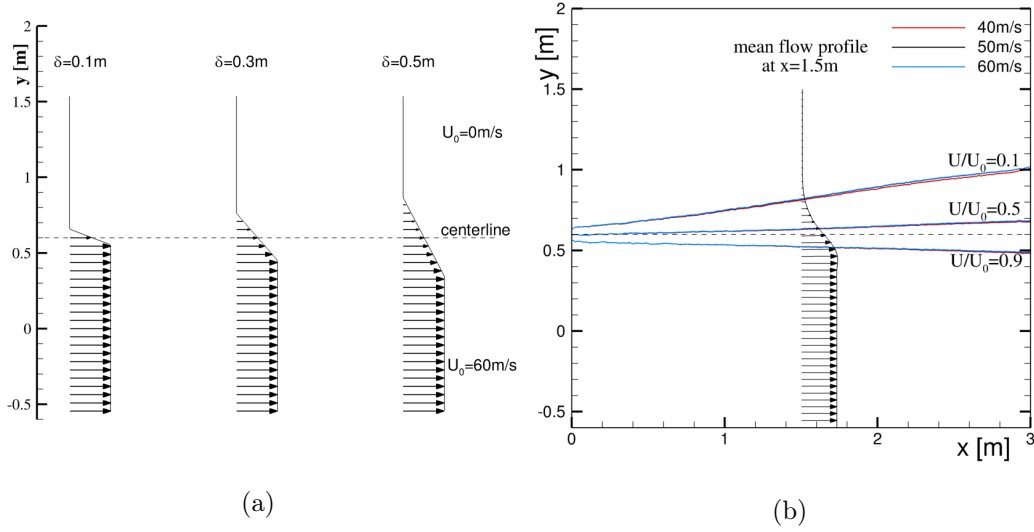


Figure 4.3: (a) velocity profiles for the constant thickness shear flow; (b) velocity lines for the AWB shear flow.

profiles are given without normalization, which keeps its centerline fixed at  $y = 0.6m$ . These velocity profiles are applied to generate the shear flows with constant thicknesses respectively. By such settings, the pure thickness effect from the shear layer can be observed without any other interferences. Besides, they are closer to the assumptions taken in Amiet's approach, which provides an opportunity to validate the method in simple cases.

Regarding the thickness definition in the wind tunnel shear layer, it is not possible to define its characteristics in exactly the same way as in the linear shear layer cases since the flow speed outside the shear layer does not exactly equal to zero. Therefore, the definition of the shear layer thickness used in Schlinker and Amiet's report [R. H. Schlinker 1980] is applied here to keep the consistency with Amiet's theoretical correction. The inner and outer boundary of the shear layer are defined by the 90% ( $U/U_0 = 0.9$ ) and 10% ( $U/U_0 = 0.1$ ) velocity lines, respectively. The distance between these boundaries is defined as the local shear layer thickness  $\delta$ , which varies from  $0.01m$  to  $0.5m$  in the applied wind tunnel shear flow. Theoretically, the half-velocity line ( $U/U_0 = 0.5$ ) should be taken as the shear layer centerline. These velocity lines are plotted for each flow speeds in Fig.4.3b with the velocity profile plotted at  $x = 1.5m$ . It is easy to observe that the spreading shape of the shear layer in the wind tunnel flow is nearly linear, whose thickness grows significantly downstream. The dashed black curve in Fig.4.3b indicates the nozzle lip-line position, which is quite close to the half velocity lines with maximum 15% deviation. Since it is not convenient to determine the half-velocity line in the wind tunnel experiments, the nozzle lip-line is deemed to be the shear layer centerline in the following study as well as in the correction approach.

The velocity profiles of the wind tunnel shear flows are given against a similarity parameter  $\eta$  to carry out the comparison of the velocity profiles at vari-

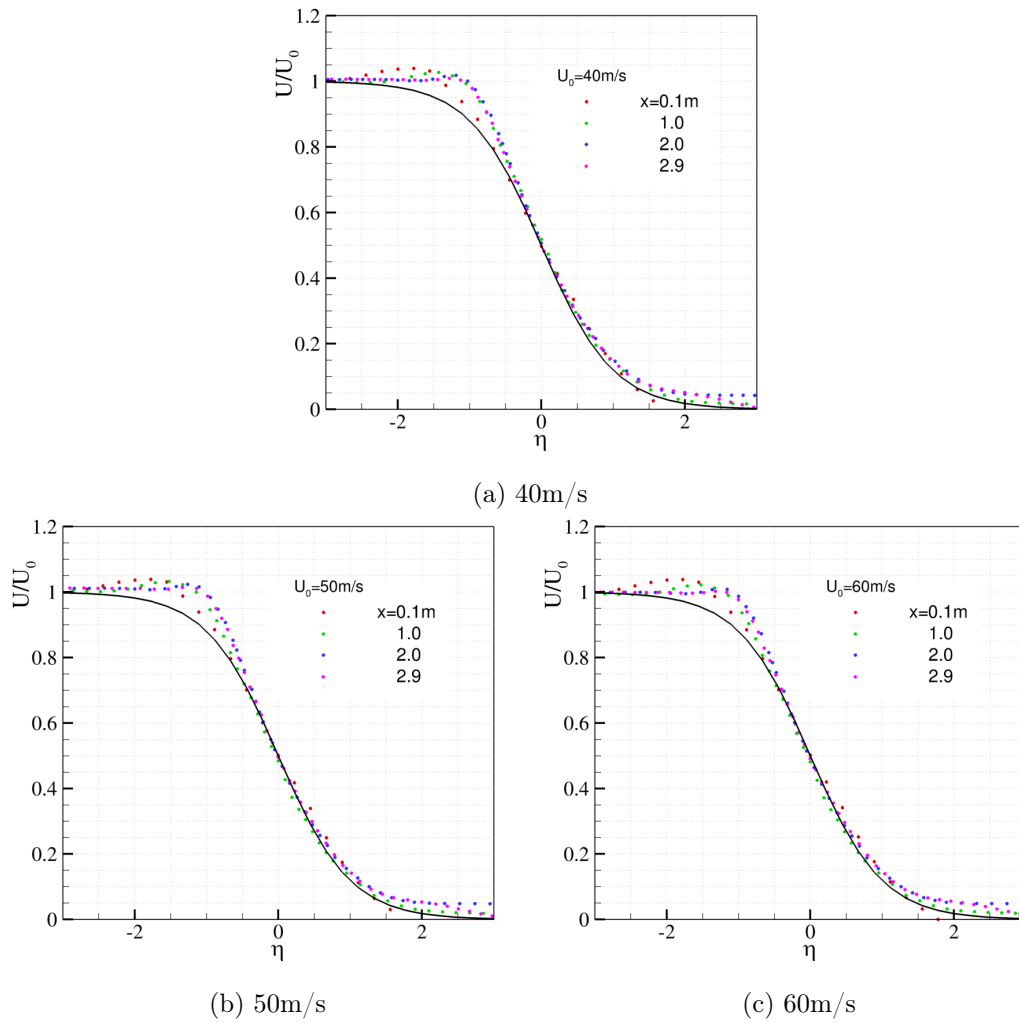


Figure 4.4: Similarity of velocity profiles at different axial sections.

ous axial sections. The parameter is extracted from Schlinker and Amiet's experimental study [R. H. Schlinker 1980], in which  $\eta$  is defined as  $\eta = (y - y_{1/2})/\delta$ , where  $y$  is the local coordinate,  $y_{1/2}$  is the half-velocity line position. The normalized velocity profiles are plotted at three stations along the flow direction for different open-jet velocities in Fig.4.4. The black curve represents the standard hyperbolic tangent analytic curve for two-dimensional plane shear layers from the report [R. H. Schlinker 1980], which is taken as a reference here. Its mathematical expression is  $U/U_0 = 0.5 [1 - \tanh(2\eta)]$ . The normalized velocity profiles at various sections show a very good collapse onto a universal distribution, whereas the hyperbolic tangent model does not quite capture the non-symmetry of the actual shear layer.

### 4.1.3 Sound propagation through constant thickness shear layers

Beginning with the sound propagation through the constant thickness shear layers, the role of the thickness in shear layer effects was investigated while different thickness-to-wavelength ratios ( $\delta/\lambda$ ) were regarded. As mentioned in Chapter 2, Amiet's approach takes the assumption of an infinitely thin shear layer, which does not agree with the practical situation in the open-jet wind tunnel (refer to Fig.4.3b). Therefore, the shear flow with linear velocity profile and constant thickness is suitable for the investigation of the pure effect of the shear layer thickness on the sound propagation. Such a simplified shear flow is supposed to help verifying the correction method as well as to enable finding the systematics of the sound propagation behavior in a finite thickness shear layer. Three thicknesses are chosen, which are  $\delta = 0.1m$ ,  $0.3m$  and  $0.5m$ . The latter two correspond to the thickness in 2D wind tunnel shear flow at  $x = 1.5m$  and  $x = 3.0m$ , respectively. The corresponding thickness-to-wavelength ratios are listed in Tab.4.2. The flow speed is  $60m/s$ .

$\delta/\lambda$	1kHz	5kHz	10kHz
0.1m	0.29	1.47	2.94
0.3m	0.88	4.41	8.82
0.5m	1.47	7.35	14.71

Table 4.2: Thickness-to-wavelength ratio of constant shear layer simulations (2D).

The computations were carried out with a harmonic source at different frequencies as listed in the tables. Fig.4.5 shows the instantaneous pressure perturbation field of periodic sound waves through the  $\delta = 0.1m$  shear layer, whose velocity profile is plotted on the left side by the red curve correspondingly. The perturbation field is given for source frequencies  $1kHz$  and  $10kHz$  to compare their various features as the ratio  $\delta/\lambda$  significantly increases. An instant is plotted where all transients of the simulation have left the domain so that the solution is strictly periodic at all positions of the domain.

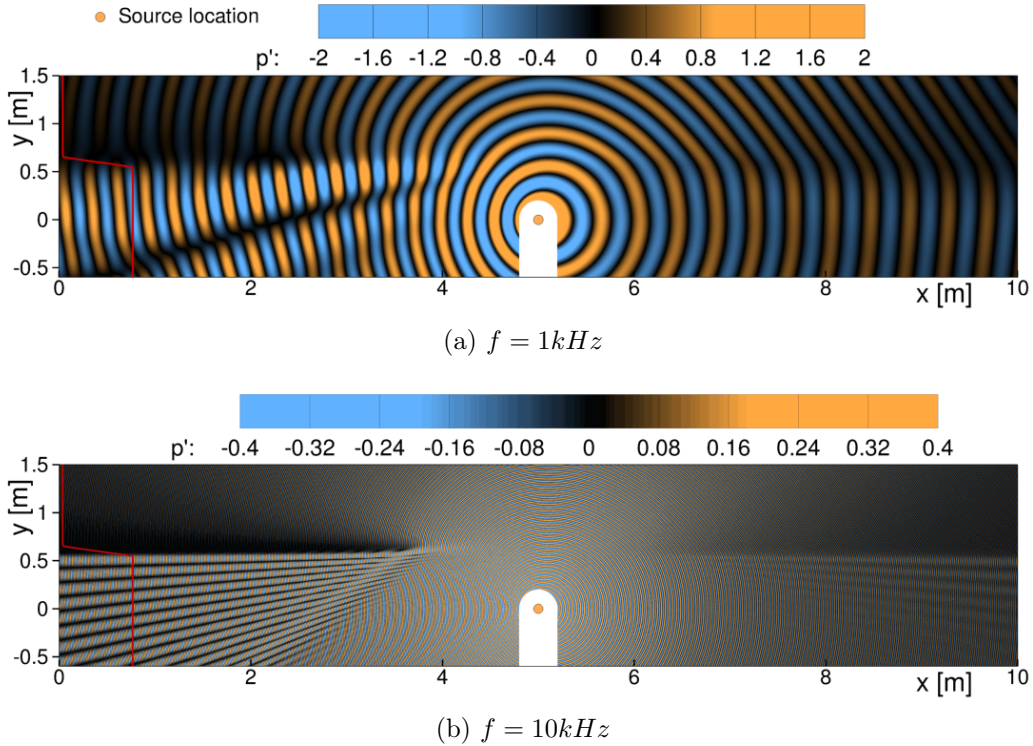


Figure 4.5: Instantaneous pressure perturbation field through  $\delta = 0.1m$  shear layer.

Looking at Fig.4.5, the most evident feature is the total reflection occurring upstream, which generates strong reflected waves. These waves interact with the original waves from the source, inducing an interference pattern below the shear layer. The total reflection feature was discussed in Sec.2.3.1, where a theoretical expression of the critical total reflection angle was derived. According to the expression, a total reflection happens upstream of the source in the flow situations considered, which is coincident with the simulation results. Another accompanying feature of the total reflection is the low perturbation area (dark shadow area in Fig.4.5) near the shear layer in the upstream direction. The area is formed by the phase shift across the shear layer between the sound waves below and above the shear layer, which can be slightly observed in Fig.4.5a. In the lower side of the shear layer, the sound waves travel slower due to the effect of the flow speed than that in the upper side, which will induce the aforementioned phase shift. This phase shift is spatially slowly varying because the wavelengths in the upper and lower domain differ slightly. Moreover, the strong bending of incident waves around the critical point of the total reflection at about  $x = 4m$  causes the sound ray tubes to spread stronger (with a respective decay in amplitude) as the refracted wave fronts travel more upstream.

In Fig.4.5 a light interference pattern could be observed in downstream domain as well, especially in the contour at  $10kHz$ . This pattern also results from the interaction of the reflected wave. When the sound wave meets the shear layer at

any other radiation angles but  $\theta_i = 90^\circ$ , a portion of the wave experiences reflection, the amount of which is dependent upon the angle as the sound wave hits the shear layer, as discussed in Sec.2.4.1. Another common feature of the perturbation field is the convection amplification by the flow speed, which is clearly expressed as a higher perturbation magnitude upstream than downstream at the same distance from the source point. This feature will be further discussed in the following section when the source directivity is examined.

To gain a deeper understanding of the sound propagation properties, the time-averaged intensity level distribution is given in Fig.4.6 for both  $1kHz$  and  $10kHz$  in the  $\delta = 0.1m$  shear flow. The intensity related values are given based on the equations mentioned in Sec.3.4. The intensity distribution itself was generated according to Eq.3.31 and averaged for several wave periods ( $> 20$  periods at the source frequency and after transients have travelled out of the domain). The shear layer region is marked with solid lines (shear layer boundaries) and dashed lines (shear layer centerline) in the figure. First of all one can observe that in contrast to the sound pressure the intensity contours do not show any convective amplification effect as expected. Since accordingly the intensity field in a uniform flow would be circular centering at the source point, one may appreciate the massive deviations from this circular structure due to the presence of the shear layer.

The interference due to the total reflection is characterized by a non-homogeneous intensity area with magnitude leaps upstream. The similar serrated pattern is found downstream corresponding to the slight reflection by the shear layer. Moreover, several low-intensity areas appear neighbouring the shear layer upstream, which correspond to the low disturbance area mentioned before due to the phase shift. The area is smooth at low frequency since the phases of the upper and lower sound waves match again after travelling certain distances, which is hard to distinguish at  $10kHz$  due to the short wavelength. In Chapter 2 the zone of silence was mentioned as another feature of the sound propagation through the shear layer, which is not clearly shown in the current case since  $\theta_i = 0^\circ$  is not achieved. However, a low-intensity level area is noticed near the right boundary, since the sound wave is always refracted to the upstream direction leaving less intensity for the downstream area.

As the intensity vector distribution is available, it is easy to plot the intensity propagation line at different radiation angles, which are shown as arrowed black curves for shear flow and blue lines for the corresponding uniform flow in Fig.4.6. The propagation traces are plotted for four radiation angles  $\theta_0 = 45^\circ, 80^\circ, 135^\circ$  and  $142^\circ$ , amongst which the last one is the critical total reflection angle calculated from the equation in Sec.2.3.1. The critical angle obviously matches with the numerical results according to the intensity propagation direction, which indicates a backward intensity propagation direction towards the open-jet flow. The radiation angle  $80^\circ$  is chosen since it corresponds to the angle value  $90^\circ$  of both incidence angle and transmission angle, which represents a no energy loss propagation through the shear layer. Comparing the intensity traces in the shear flow and the uniform flow, the alteration of the sound wave propagation direction by the shear layer is

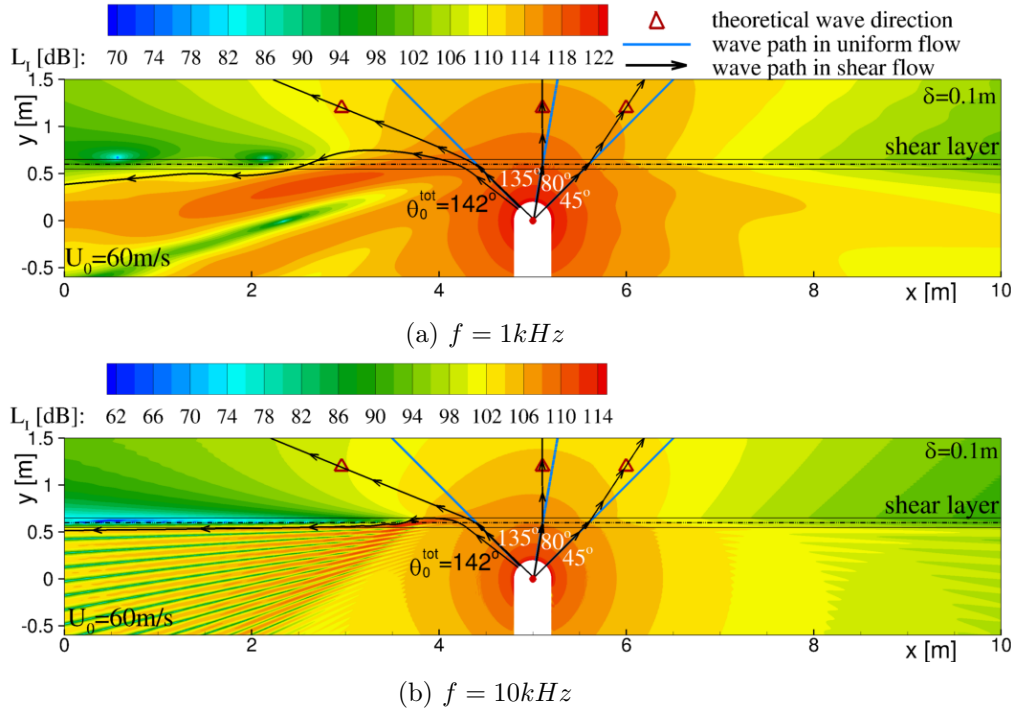


Figure 4.6: Intensity level distribution through  $\delta = 0.1m$  shear layer.

clearly shown, which demonstrates the most obvious deviation as sound wave radiates towards upstream. Beside the traces from numerical results, the transmitted directions for given radiation angles are shown as red deltas for the predictions obtained from the angle correction of Amiet's approach. They are in good agreement with the computations. It indicates that the angle correction of Amiet's approach has a good performance in such a linear thin shear flow and can revise the direction change of sound waves by the shear layer extremely well.

Turning to the distinction brought by the frequency variation, it is found that the sound wave experiences similar effects at both low and high frequencies through a thin shear layer  $\delta = 0.1m$ . The angle correction performs well for both frequencies, which is reasonable since the case is quite close to the infinitely thin shear layer assumption taken in Amiet's approach. Its performance is further examined for a thicker shear layer  $\delta = 0.3m$  flow in the following.

Fig.4.7 shows the instantaneous pressure perturbation field in the  $\delta = 0.3m$  shear flow. Comparing with Fig.4.5, the features at  $1kHz$  do not show distinctive variation, while the total reflection at  $10kHz$  happens more gradually in a thicker shear layer. This illustrates the fact that the total reflection is relevant with the variation rate of the mean flow gradient in space, leading the development from a total reflection point to a less focussed 'smeared-out' total reflection. Moreover, the shadow zone caused by the phase shift increases in size in the vertical direction, which appears to be proportional to the thickness. Its validation will be further checked as the thickest shear layer ( $\delta = 0.5m$ ) is considered.

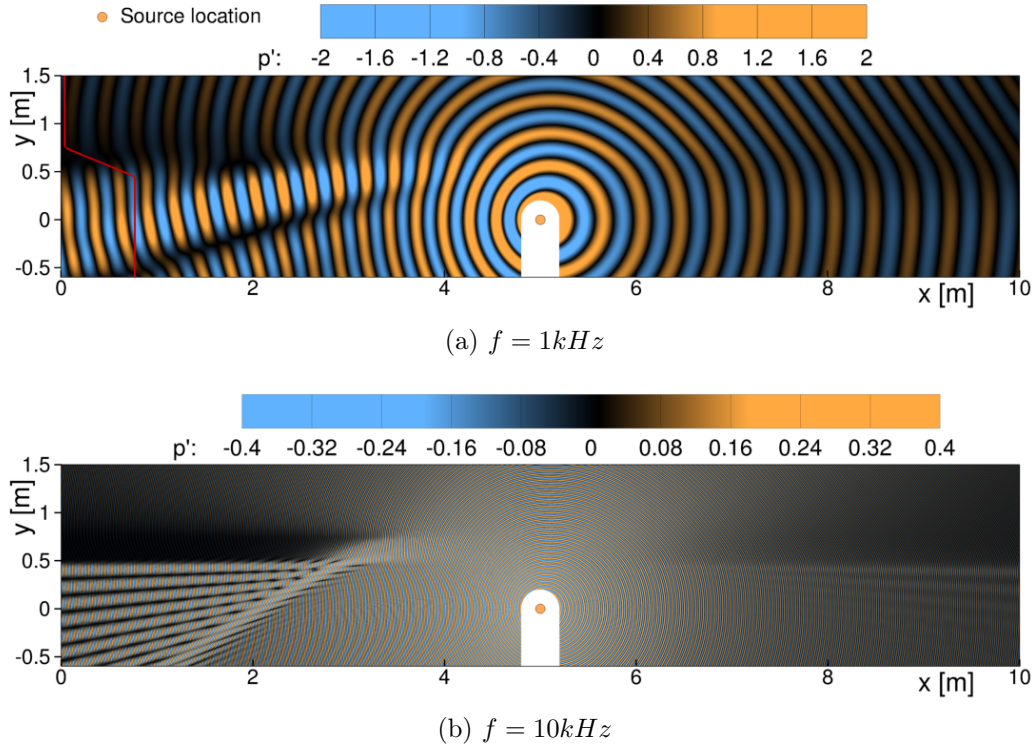


Figure 4.7: Instantaneous pressure perturbation field through  $\delta = 0.3m$  shear layer.

Fig.4.8 gives the intensity level distributions for the  $\delta = 0.3m$  shear flow. The total reflection point appears to be pushed forward with the low-intensity level area moving upstream as well. It is clear that the interference pattern below the shear layer moves away from the source at  $10kHz$  and shows a higher intensity level than in the  $\delta = 0.1m$  shear flow. This may be caused by the gradually occurring total reflection, which induces the interference among several reflected waves. By comparing the serrated distribution downstream below the shear layer, a weaker reflection is seen as the thickness increases. To quantitatively investigate the feature of the reflection by the shear layer, the directivity of the source in the shear flow will be presented later.

Regarding the intensity propagation path, a very good agreement between the computations and the theoretical predictions is observed as before. As listed in Tab.4.2,  $\delta/\lambda$  is around 8 at  $10kHz$ . The local ratio is even bigger than that as the sound hits the shear layer obliquely. The good agreement between the computations and the theoretical predictions under such a situation indicates that the shear layer thickness plays a less important role in the alteration of the propagation direction of the sound. To learn more about the thickness effect, the case with  $\delta = 0.5m$  was finally considered in this part.

Fig.4.9 shows the instantaneous pressure field for the  $\delta = 0.5m$  shear flow, which shows quite similar characteristics as in the previous cases. The interference pattern due to the total reflection slightly moves forward and shows a more gradually trend.

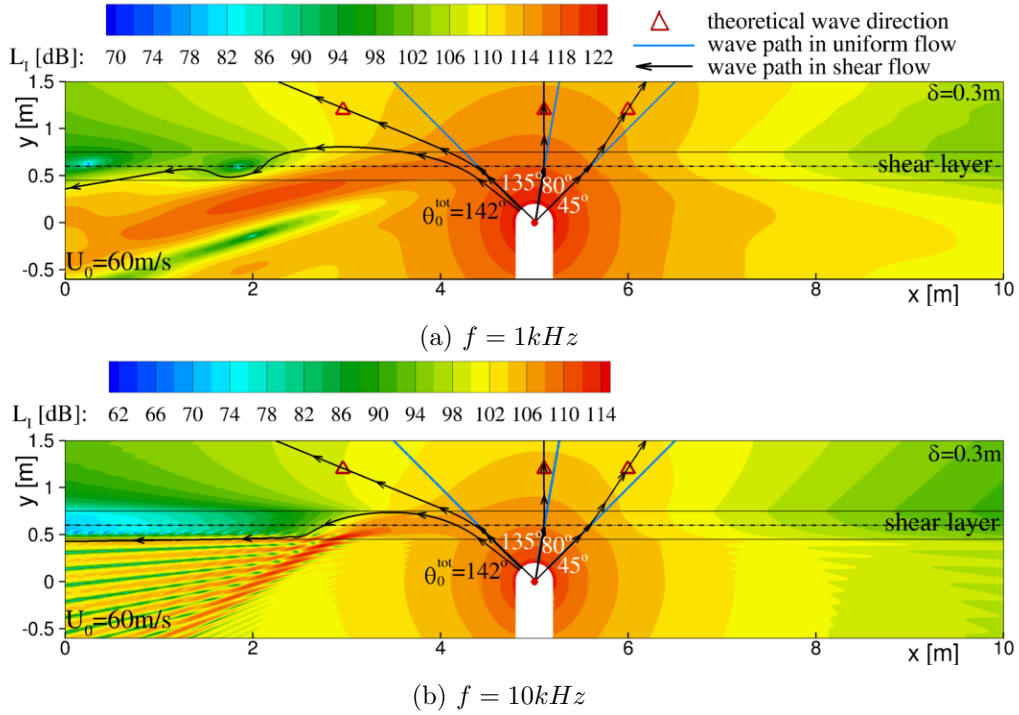


Figure 4.8: Intensity level distribution through  $\delta = 0.3m$  shear layer.

The area of the low signal strength caused by the phase shift expands with the thickness, which obviously results from the enlarged mean flow gradient area in vertical direction. This verifies that the total reflection by the shear layer is a gradual procedure, whose characteristics vary with the thickness of the shear layer.

Again, the intensity level contour is given in Fig.4.10. Obviously, a weaker reflection occurs downstream than in previous cases, which indicates that more energy of the sound wave is kept and transmitted through the shear layer rather than being reflected back to the jet flow. Moreover, the low-intensity area due to the phase shift moves further upstream compared to the other cases. When the propagation direction is considered, it shows weaker agreement between the computations and the theoretical predictions. The correction method predicts a slightly bigger transmission angle upstream and a smaller transmission angle downstream. This phenomenon may result from the convective effect by the flow speed through the shear layer. When the sound wave travels through a thicker shear layer, it experiences the convective effect in longer time compared with a thin shear layer. Therefore, its transmission angle is slightly changed by the flow speed, which is similar to the convection effect in the jet flow. Besides, it is interesting to note that particularly the simulation for the thick shear layer shows, that the occurrence of the total reflection is a function of the overall speed difference across the complete shear layer only. Fig.4.10b almost perfectly demonstrates this feature when considering the ray leaving the source under the theoretically predicted critical radiation angle for the total reflection. The propagation direction reverses in the vertical direction right at

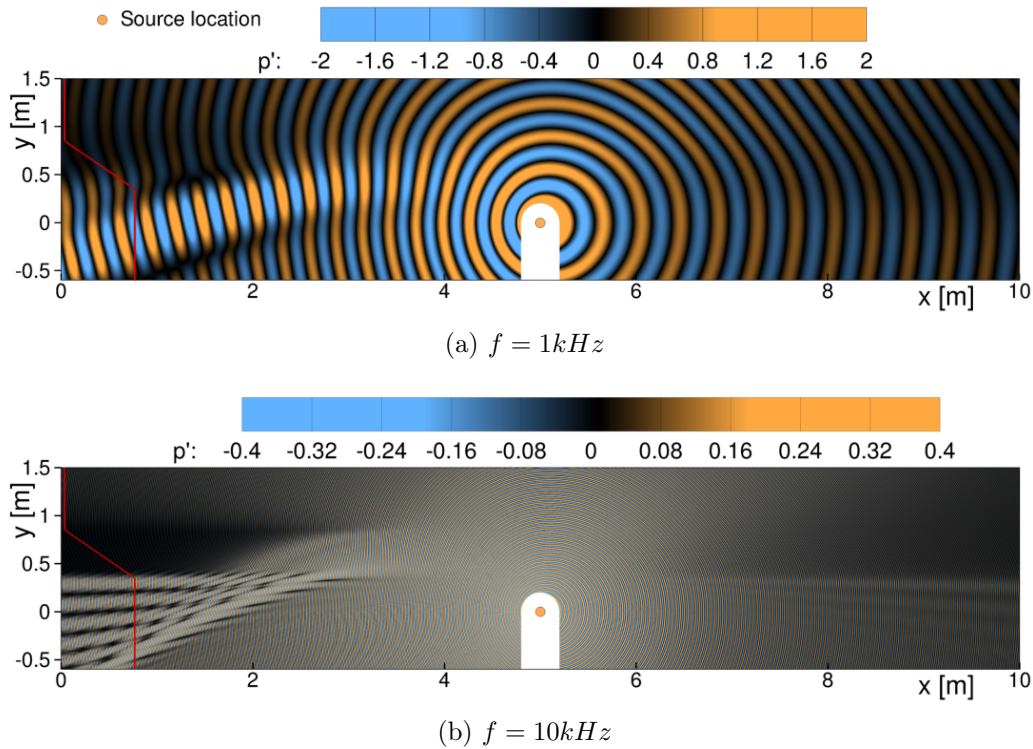


Figure 4.9: Instantaneous pressure perturbation field through  $\delta = 0.5m$  shear layer.

the vertical position where the shear layer ends.

As final observation it is noted, that the intensity lines leaving the source under the theoretical critical angle of total reflection turn parallel to the shear layer at more upstream positions not only as the shear layer thickness grows but also as the frequency decreases.

So far the basic characteristics of the sound propagation through constant thickness shear layers were introduced. Based on these qualitative comparisons for different source frequencies, it is found that the shear layer thickness affects the sound wave propagation characteristics in the extreme area, such as total reflection. The sound intensity distribution seems not to be affected too much far from the shear layer. However, it should be noticed if microphones are set in the region in front of the source near total reflection area. The angle correction in Amiet's approach can be applied to give the critical total reflection angle to avoid such a problem. The performance of the angle correction was validated and proved to be efficient as  $\delta/\lambda$  approaches to a big value. Next section will present the quantitative study of the sound field in the constant thickness shear flow as well as the comparison with the theoretical corrections.

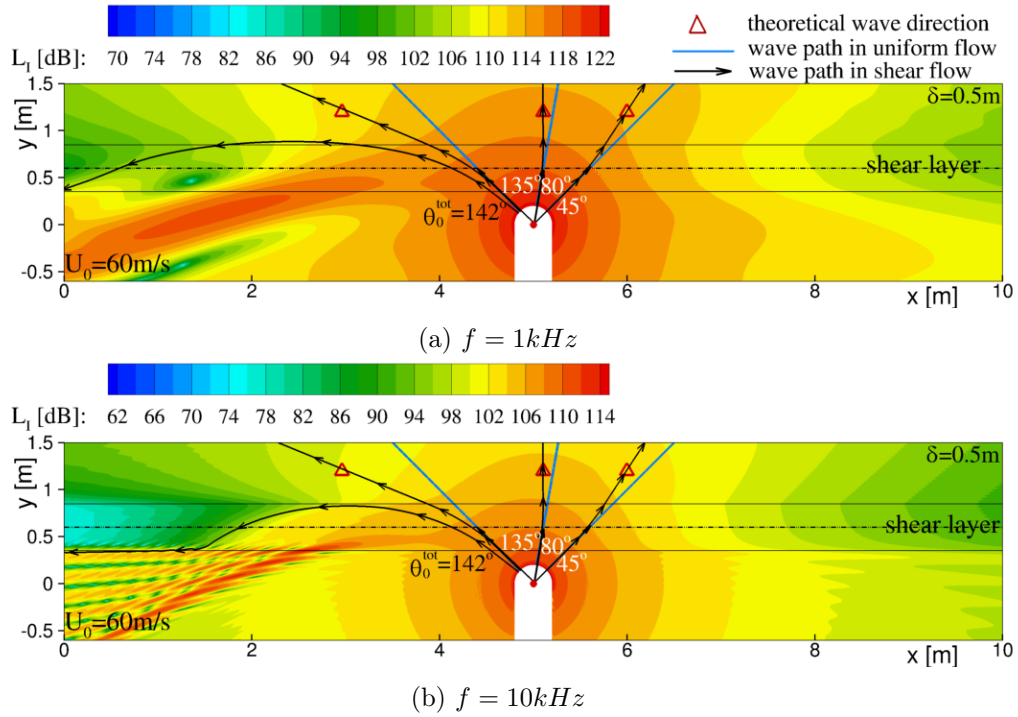


Figure 4.10: Intensity level distribution through  $\delta = 0.5m$  shear layer.

#### 4.1.4 Alteration of the sound wave amplitude through constant thickness shear layers

By observing the instantaneous pressure field and the intensity field, the features of the sound propagation through shear layers were exhaustively investigated. Next, to define exactly by how much the shear layer changes the sound pressure level received by the microphones as a function of the shear layer thickness, the pressure perturbation amplitude at receiver's position needs to be analysed. For this purpose, the pressure magnitude at specified microphone positions is extracted from the computational results, which record the root mean square pressure values. The perturbation data are later translated into sound pressure level (SPL) as mentioned in Sec.3.4. As already introduced in Sec.4.1.1, the position at  $y_M = 1.2m$  is chosen as the microphone line for the investigation, which corresponds to a  $h/y_M$  value of 0.5 in theoretical corrections. The SPL data along the line is extracted for the analysis and comparison with the theoretical values.

Fig.4.11 presents the sound pressure level for the specified microphone line at the source frequency  $1kHz$ . The  $x$ -axis represents the horizontal coordinate of the microphones, which correspond to the measurement angle  $\theta_M$  in the range  $15^\circ \sim 165^\circ$ .  $x = 5m$  indicates the position right above the source position, where  $\theta_M = 90^\circ$ . The SPL curves for various shear layer thicknesses match extremely well at the positions near  $x = 5m$ , in the angle range around  $\theta_M = 39^\circ \sim 141^\circ$  (corresponding to the coordinate range  $x = 3.5m \sim 6.5m$ ). In this range, the SPL of the transmitted wave will not vary with the shear layer thickness in the current background. This

illustrates an ignorable thickness factor as the mean flow gradient effect is considered. Beyond this angle range, the deviation brought by the shear layer thickness increases with the distance from the source point, which achieves a maximum of about  $1dB$  deviation between shear flows with thickness  $\delta = 0.1m$  and  $\delta = 0.5m$ . It is noticed that in the upstream positions the deviation increases slowly and show a smaller deviation than downstream between  $\delta = 0.3m$  and  $\delta = 0.5m$ . The reason for this better coincidence is not clear yet. Generally, the SPL value at the receivers' positions is higher in a thicker shear flow, indicating a larger transmission portion through the shear layer. In other words, the thickness of the shear layer tends to stretch the SPL distribution longitudinally about its maximum. This agrees with the weaker reflection observed in Fig.4.10 for  $\delta = 0.5m$ .

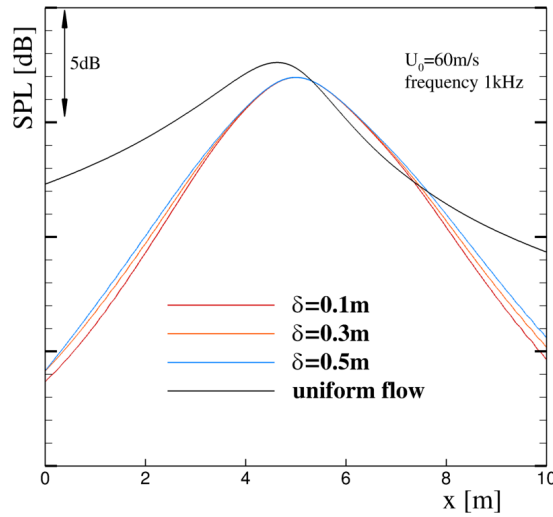


Figure 4.11: Sound pressure level distribution along microphone line  $y_M = 1.2m$ .

In Fig.4.11 the SPL value at the same receivers' positions in a uniform flow ( $U_0 = 60m/s$ ) is given as well, from which the convective amplification effect by the flow speed is quite clear. This curve can be taken as a reference to illustrate the amplitude variation induced by the shear layer. It shows a stronger alteration by the shear layer as the distance between the receiver and the source increases, which indicates the maximum deviation around  $8dB$  at the most upstream located measurement position. The curves are given only for  $1kHz$  since the SPL distributions at higher frequencies show the identical trend, whose SPL distributions are presented in the Appendix B.

By the previous comparisons, it is clear how much influence the shear layer has on the amplitude of transmitted waves in the shear flow with different thickness. Since the pressure amplitude along the same microphone line is known in both the shear flow and the uniform flow, it is convenient to plot the amplitude ratio curve as in Amiet's approach (refer to Fig.2.3). With the help of the angle correction, the coordinate of the corrected position  $A$  for each receiver at point  $M$  could be easily determined. Then the pressure amplitude data at the corrected position can

be extracted from the black curve in Fig.4.11. Finally, its ratio to the amplitude value at  $M$  is calculated. In this way, the performance of the amplitude correction could be validated in constant thickness shear flow, which is helpful for our further study in the real wind tunnel shear flow.

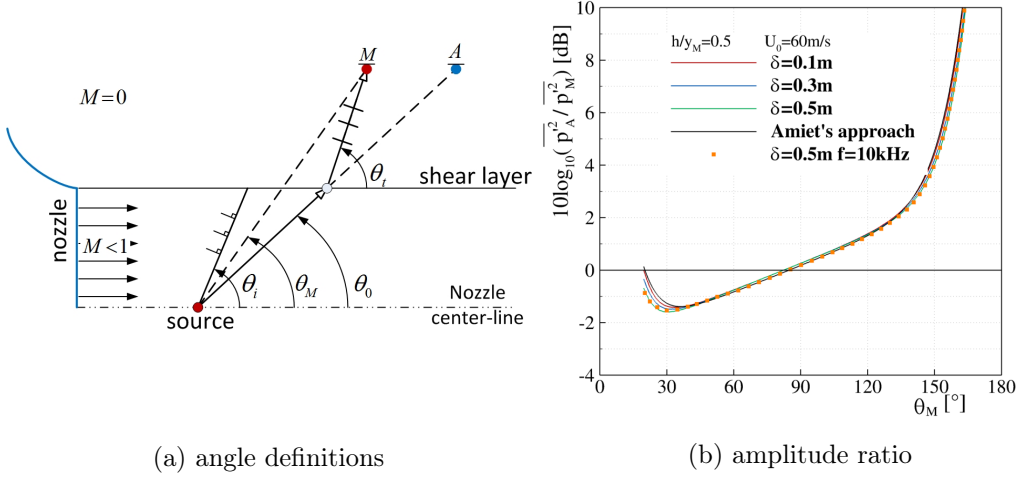


Figure 4.12: Comparison of pressure amplitude ratio between computations and the theory for constant thickness shear layers ( $f = 1kHz$ ).

Fig.4.12b gives the pressure amplitude ratio curves against the measurement angle  $\theta_M$ . The corresponding angle definitions, as well as the position of measurement and corrected points, are sketched in Fig.4.12a. The black curve is obtained from the amplitude correction of Amiet's approach for the corresponding measurement angle, in which the Mach number is 0.18 and the distance ratio  $h/y_M$  equals to 0.5 for the considered cases. The curves extracted from computational results at the source frequency  $1kHz$  for different thicknesses are given in colored curves. Amongst these, the curve for  $\delta = 0.1m$  shows the closest distribution to the theoretical values as expected. In the angle range  $\theta_M = 40^\circ \sim 145^\circ$  the pressure ratio shows quite nice agreement between computations and theoretical predictions with maximum deviation around  $0.2dB$ . Looking at the data at extreme angles very upstream and downstream, the amplitude correction could well predict the shear layer effect with less than  $1dB$  deviation from the computational results. This means that the mean flow gradient effect caused by the shear layer could be perfectly corrected by Amiet's approach for the constant thickness cases. The amplitude ratio at the source frequency  $10kHz$  is only presented for  $\delta = 0.5m$  since it shows a quite close distribution as that at  $1kHz$ . This indicates a weak frequency relevance in the amplitude correction for the constant thickness shear flow, which is a positive circumstance for the following study. The characteristics will be further validated for the actual wind tunnel flow in the following sections.

Until now we have implemented both qualitative and quantitative studies on the sound transmission through constant thickness shear layers for various source frequencies. The study gives a basic view of the sound propagation through the

shear layer and shows the deviations caused by the shear layer thickness and the source frequency. Amiet's approach was primarily validated in simplified shear flows as well. In the previous sections, the computational results are mainly given for frequency  $1kHz$  and  $10kHz$  for comparisons. Other results for source frequency  $5kHz$  may be found in the Appendix B.

#### 4.1.5 Sound propagation through wind tunnel shear layers

Sec.4.1.2 presented some basic information of the 2D wind tunnel shear flow of AWB, which illustrates a spreading shaped shear layer (Fig.4.3b) as well as a non-linear velocity profile (Fig.4.4). By the primary study of the thickness effect in previous sections, it could be assumed that the thickness rarely brought deviation to the amplitude and direction of the signals received by the microphones. This conclusion is drawn for the specified shear flow with linear velocity profile, which actually differs from that in a real wind tunnel shear flow introduced in Sec.4.1.2. To further investigate the sound propagation characteristics and the performance of Amiet's approach, the computations were implemented in a more realistic wind tunnel shear flow. As already introduced in Sec.4.1.2, three typical wind tunnel flow speeds in the AWB were chosen, i.e.  $40m/s$ ,  $50m/s$  and  $60m/s$ . The influences induced by the flow speeds was taken into account by such a setting.

Fig.4.13 shows the instantaneous pressure field in the wind tunnel shear flow with  $U_0 = 40m/s$ , in which the shear layer shape and its position are indicated by the red curves. The red curves are generated according to the definitions mentioned in Sec.4.1.2, which define the upper and lower boundaries of the shear layer in the flow field. The pressure contours show very similar features as those of the previous cases. The total reflection happens near the left boundary, which identifies as high-pressure amplitude through the shear layer. The corresponding interference pattern below the shear layer is not as clear as in previous cases due to the shrunk domain size. It should be mentioned that the critical total reflection angle increases as the flow speed decreases, which indicates a total reflection happens at the more upstream position.

Fig.4.14 plots the sound intensity level distribution as well as the propagation direction in the wind tunnel shear flow with  $U_0 = 40m$ . The level range differs with the source frequency, but the interval and the overall increment of the contour are kept the same for both frequencies, i.e.  $1dB$  and  $10dB$  respectively. The distribution shows obvious protrusion to upstream caused of the total reflection, whose critical angle is indicated by  $\theta_0^{tot}$ . The difference in the results for the frequency variation is not distinctive except the serrated distribution near the left boundary at  $10kHz$ . Such a distribution might be caused by the nearby boundary condition, which does not entirely lead the sound wave to propagate farther outward but generates slight reflection back into the domain.

Considering the intensity propagation directions in Fig.4.14, the satisfying agreement is still kept at both frequencies between Amiet's correction and computations in the context of the spreading shear layer. The only mismatch of the intensity prop-

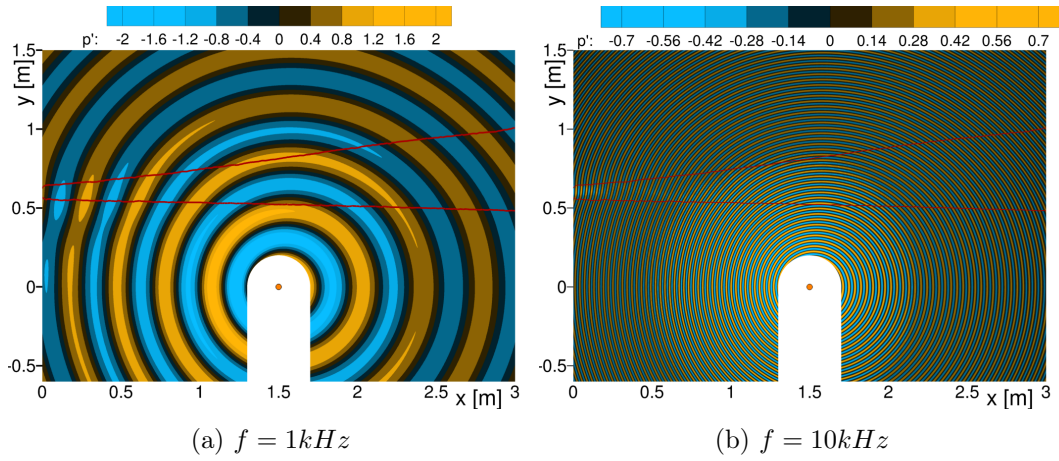


Figure 4.13: Instantaneous pressure perturbation field in  $U_0 = 40m/s$  wind tunnel shear flow.

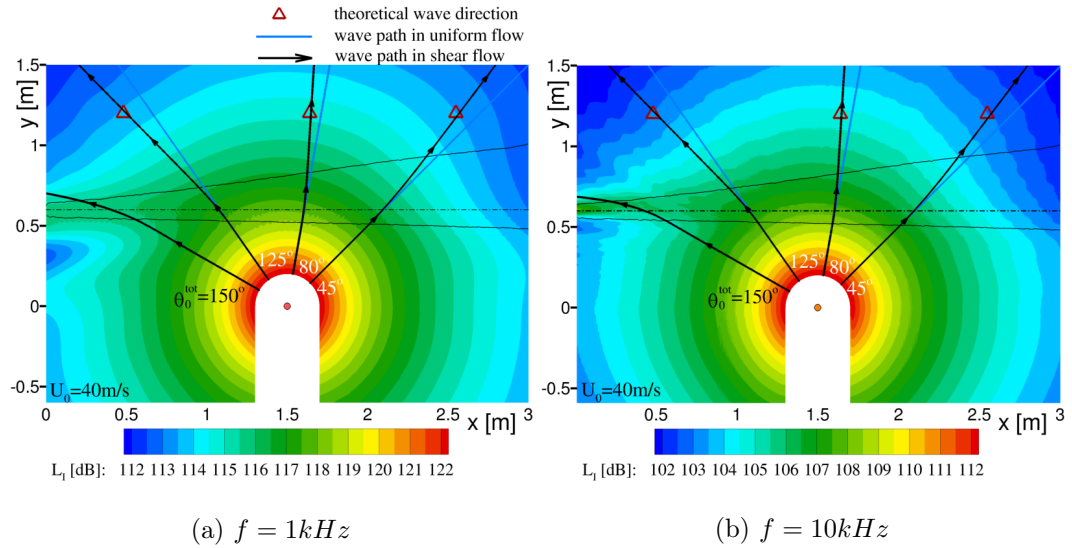


Figure 4.14: Intensity level distribution through  $U_0 = 40m$  shear flow.

agation path is at the critical total reflection angle. The wave path goes beyond the shear layer instead of propagating backward into the jet flow at the theoretical critical total reflection angle. This happened also for the previous constant thickness case ( $\delta = 0.1m$ ) but then goes back to the jet flow as it propagates further. Such further development of the propagation path is not observable here due to the limited computation domain size. Further simulation is necessary to determine the propagation path in an extended domain. Another possible reason is the reflection effect by the left boundary condition (radiation boundary condition Eq.(3.5)), which disturbs the intensity distribution around the total reflection area and further causes deviation of the critical total reflection angle.

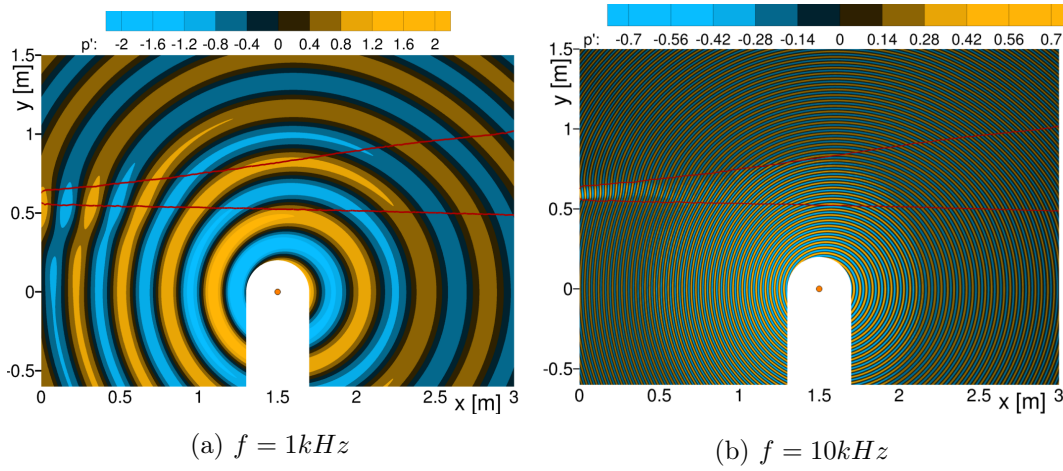


Figure 4.15: Instantaneous pressure perturbation field in  $U_0 = 50m/s$  wind tunnel shear flow.

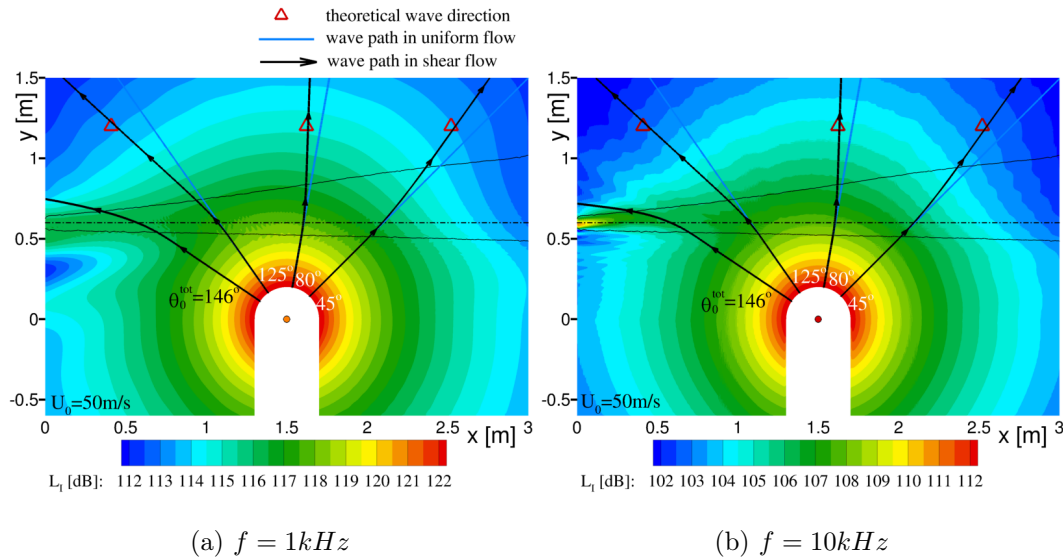


Figure 4.16: Intensity level distribution through  $U_0 = 50m$  shear flow.

Similarly, the instantaneous pressure field and intensity level contour are given

in Fig.4.15 and Fig.4.16 for the wind tunnel shear flow with  $U_0 = 50m$ . Since the influences from thickness variation and spreading shape of the shear layer are proved to be insignificant, the following study will focus on the differences brought by the flow speed. Comparing Fig.4.15 with Fig.4.13, the  $50m/s$  case presents a very similar pattern as that for  $U_0 = 40m/s$  but with a more obvious total reflection as indicated by the bright color upstream. This is verified by the intensity level contour in Fig.4.16 with a high-intensity level area appearing near the left boundary around the shear layer centerline (plotted by the dashed line). Here the total reflection happens earlier at  $146^\circ$  according to Amiet's approach, which could be the reason for the clearer pattern. Considering the wave paths, the deviation between computations and theoretical predictions of the sound propagation direction expands slightly, which may be due to the convective effect through the finite thickness shear layer as mentioned earlier.

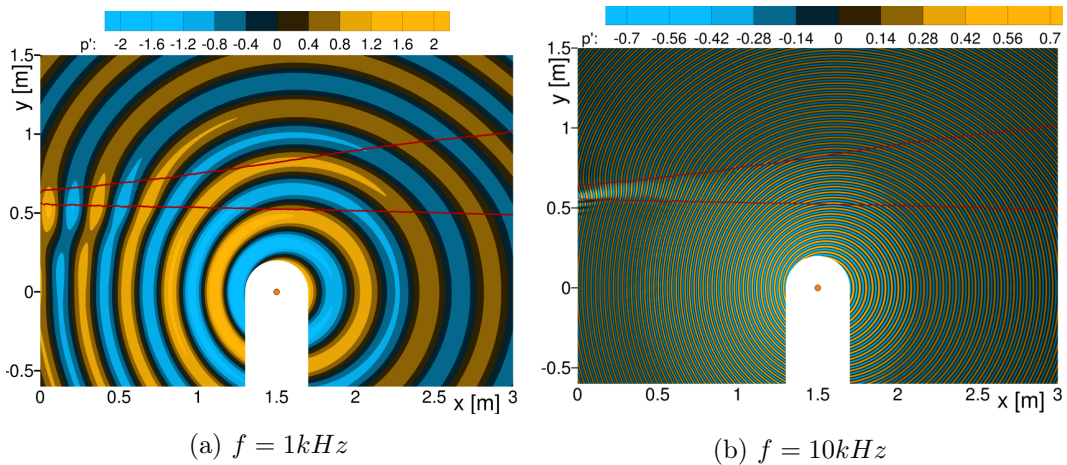


Figure 4.17: Instantaneous pressure perturbation field in  $U_0 = 60m/s$  wind tunnel shear flow.

The last contours are plotted for the sound propagation in the wind tunnel shear flow at  $U_0 = 60m/s$  in Fig.4.17 and Fig.4.18. A more obvious total reflection happens upstream, which generates a clear interference pattern below the shear layer. Since the left boundary corresponds to the position of the nozzle exit plane of the AWB wind tunnel, this simulation clearly indicates that at  $60m/s$  total reflection occurs in the shear layer outside the nozzle. The theoretical correction again predicts a slightly bigger deviation due to the refraction by the shear layer.

By showing the computational results, some characteristics of the sound propagation through the spreading wind tunnel flows were analyzed and investigated. A stronger mean flow gradient effect was observed with increasing flow speed. By comparing with the theoretical predictions, it was found that the spreading shape of the shear layer does not introduce any strong influences. The angle correction could still correct the mean flow gradient effect accurately. Next, the accuracy of the amplitude correction will be validated.

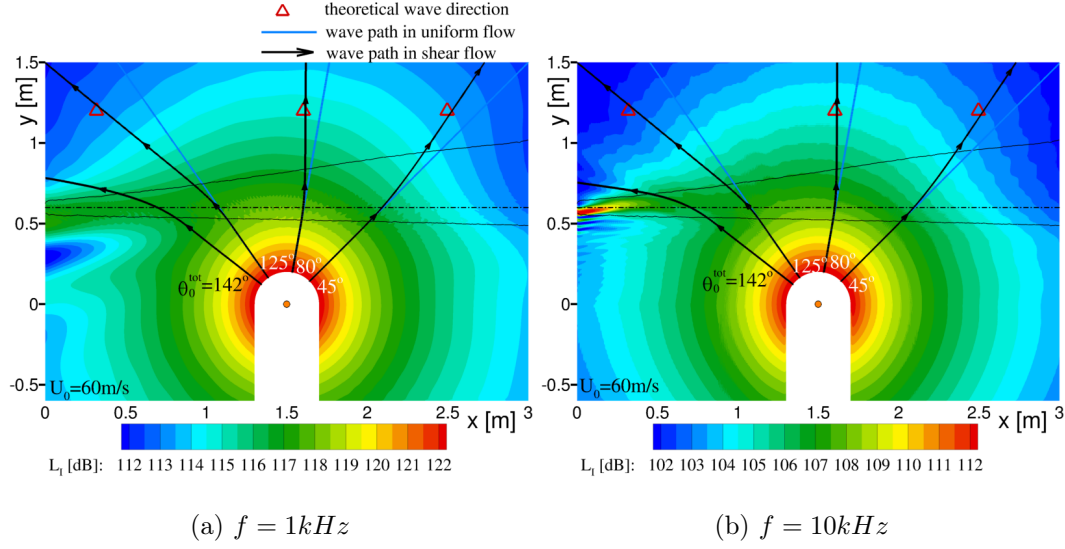


Figure 4.18: Intensity level distribution through  $U_0 = 60m$  shear flow.

#### 4.1.6 Alteration of the sound wave amplitude through spreading shear layers

The pressure amplitude distribution for the source frequency  $1kHz$  is given along the microphone line  $y_M = 1.2m$  as SPL values in Fig.4.19, in which the solid lines indicate the value received in the shear flow while the dashed lines represent the data received in the uniform flow at the same microphone position. The distributions in the shear flows with various flow speeds show almost identical profiles with only small differences (max.  $0.4dB$ ) near boundaries ( $x = 0$  and  $x = 3$ ). Considering the curves in the corresponding uniform flows, they express an obvious directional distribution due to the flow speed. Such a directivity is eliminated by the refraction effect of the shear flow and generate a similar directivity for considered flow speeds. Additionally, one may notice the wavy forms of the solid lines upstream, which are caused by the numerical boundary conditions rather than the shear layer effect. It would disappear if the computation domain was further extended upstream.

Another feature in Fig.4.19 is the inverted magnitude sequence at upstream locations for various flow speeds. In contrast to the sequence in the uniform flow that a higher magnitude is received in the higher speed flow, the magnitude goes down as the shear flow speed goes up. This indicates that upstream loss in the transmitted signal due to a stronger reflection by the shear layer in higher speed shear flow slightly overcompensates the increase due to convective amplification. This will be further validated by drawing the directivity at the same distance from the source in the next section.

Since the SPL in the shear flow and the uniform flow are available, the pressure amplitude ratio can be given between corrected point (A) and measurement point (M), as depicted in Fig.4.20. Although the flow speeds varies, the deviation between

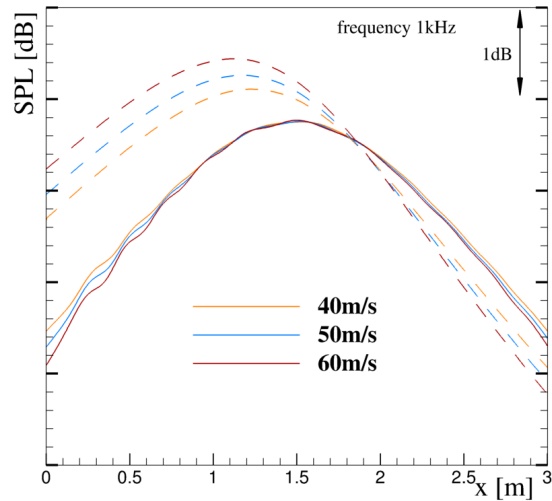


Figure 4.19: Sound pressure level distributions along the microphone line  $y_M = 1.2m$ . ( shear flow —; uniform flow - - )

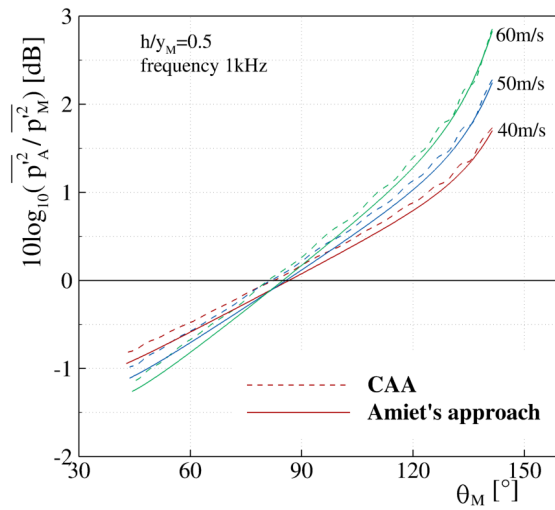


Figure 4.20: Comparison of pressure amplitude ratio between computations and the theory for wind tunnel shear layers.

computations and the theory stays in a certain range, i.e. maximum  $0.15dB$ . The computational results are almost coincident with the theory upstream ( $\theta_M > 90^\circ$ ) where the shear layer thickness is close to  $0.1m$  (approaching the zero-thickness assumption), while the maximum deviation occurs downstream where the thickness approaches a thickness of  $0.5m$ . Generally, the theory gives a lower correction magnitude than computational results, representing an underestimation of the amplitude at the corrected position in the theory. However, comparing with the amplitude ratio in the constant thickness shear flow, the overall prediction from the theory shows a good agreement with computations even when the wind tunnel shear layer owns a spreading shape.

#### 4.1.7 Source directivity in constant thickness and wind tunnel shear flows

As introduced in the previous sections, the extraction of the source directivity from computations in the shear flow is a helpful way to investigate the sound propagation and reflection characteristics. It is convenient to infer the strength of the reflection by the shear layer since the numerical simulation can provide the data below the shear layer. In order to investigate the sound propagation features before and after the total reflection point, the sound pressure directivity is firstly plotted along circles at two radii. One radius equals to  $1.0m$  centered at the source point, which is inside the region just before the total reflection point. The other radius equals to  $1.4m$  centered at the source point, which is beyond the total reflection point.

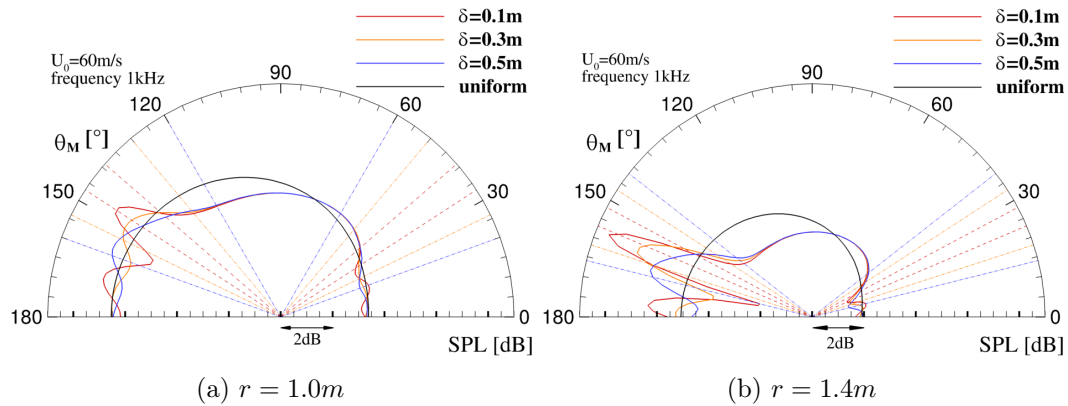


Figure 4.21: Sound pressure directivity of point mass/heat flow source in the constant thickness shear flow.

Fig.4.21 shows the source directivity at  $1kHz$ , in which the colored curves represent the data in the shear flow while the black curve indicates the data in the uniform flow. The regions, where the microphone line crosses the shear layer, are marked by the dashed lines with the corresponding color for each thickness. For example, the microphones located between measurement angles  $33^\circ \sim 41^\circ$  are inside the shear layer in the  $\delta = 0.1m$  shear flow, which are labelled by the red dashed

lines. Looking at Fig.4.21a, before the critical total reflection point, the wavy parts in both upstream and downstream area indicate the sound wave reflection by the shear layer. Obviously, a stronger reflection happens in the upstream locations as well as in the thinner thickness shear flow. This holds also for the distribution if the microphones are positioned further beyond the critical total reflection point, as given in Fig.4.21b. The distributions in Fig.4.21b illustrate a severe amplitude fluctuation upstream, which results from the interference between the reflected wave and the original sound wave. Such a fluctuation can cause up to  $3dB$  deviation comparing to the data in the uniform flow. The deviation can not achieve  $6dB$ , since the reflected wave amplitude decreases in a longer travelling path relative to the original wave. Additionally, Fig.4.21b demonstrates a stronger reflection by the shear layer since the corresponding incident wave hits the shear layer at a more shallow incidence angle.

Similarly, the sound pressure directivity in the wind tunnel shear flow may be extracted from computations at the same radii for various flow speeds, as plotted in Fig.4.22. Since the defined shear layer region is quite identical at the considered flow speeds (refer to Fig.4.3b), the label of the shear layer region is only given at the flow speed  $U_0 = 60m/s$  by the red short-dashed lines. The solid curves represent the values in the shear flow, while the long-dashed curves indicate the values in corresponding uniform flow.

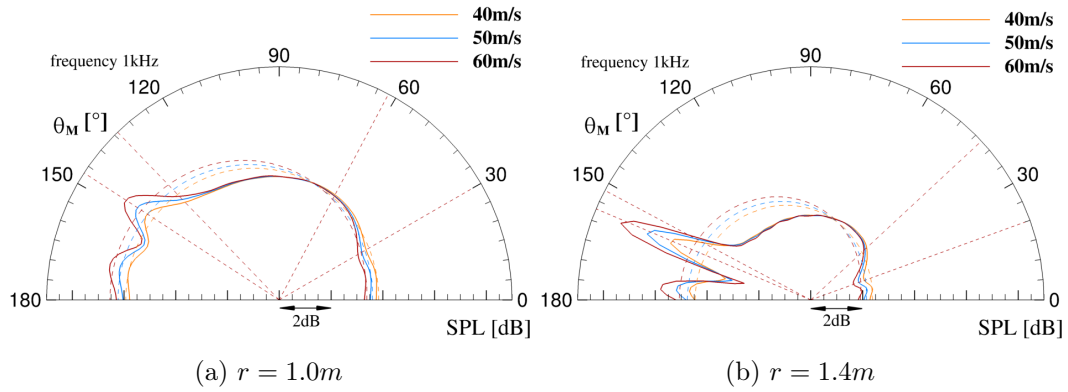


Figure 4.22: Sound pressure directivity of point mass/heat flow source in the wind tunnel shear flow.

Next, the distribution in Fig.4.22 is compared with that in Fig.4.21 at  $U_0 = 60m/s$ . The wavy form resulting from the reflection shows a smoother fluctuation in upstream direction since the shear layer thickness is bigger than  $\delta = 0.1m$  around these microphones. In downstream locations, the level is close to that of the  $\delta = 0.5m$  shear flow due to the thickness similarity. Considering the variation brought by the velocity, the reflection shows an increasing trend in strength as the flow speed goes up, which is coincident with the phenomenon observed in the pressure and intensity level contours.

## 4.2 Sound propagation through the curved shear layer (2D)

### 4.2.1 Computational setup

In the previous sections, we focused on the studies of the sound propagation through a simple analytical parallel shear layer. The corresponding base flow was obtained by CFD simulations of an empty test section wind tunnel. This ensures that the shear layer centerline is approximately parallel to the nozzle centerline (see Fig.4.3), which enables us to validate the correction method conveniently. However, the flow field is always altered by the test model placed in the test section in the wind tunnel tests, which can induce a change in the shear layer shape as well as its characteristics. In order to identify the sound propagation behavior in such an altered shear flow and further validate the correction method, the 2D flow field around a high-lift airfoil DLR F16 was considered at a specified geometric angle of attack.

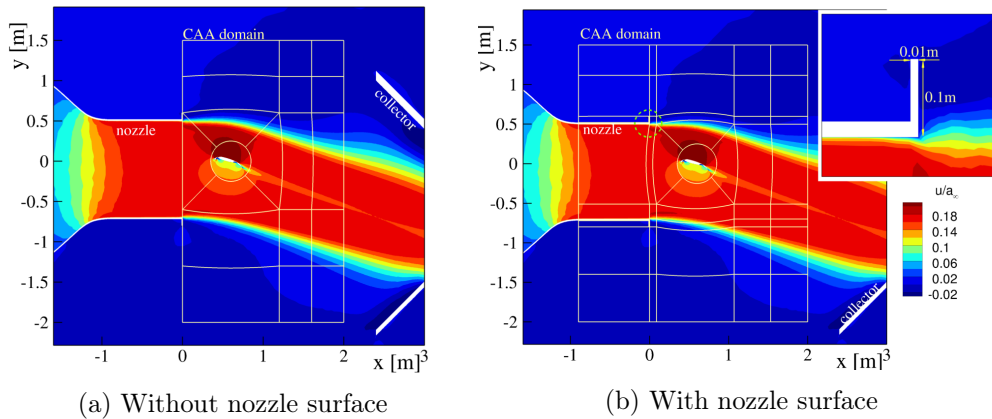


Figure 4.23: Computation domain for simulations in the curved shear flow.

The computations were firstly carried out in the wind tunnel shear flow with  $U_0 = 60\text{m/s}$ , which is free of any solid wall, as shown in Fig.4.23a. The range and the structure of the computation domain are illustrated by the yellow grid structure. The part around the airfoil surrounded by a circle was removed and a harmonic source is placed at its center instead. Since the current study focuses on the pure shear layer effects, a harmonic source was considered appropriate and consistent with the existing study than the broadband noise from an airfoil. The sound wave from the source is introduced into the domain by a sponge layer boundary condition along the circle. The domain was extended in the vertical direction to include both the upper and lower shear layer since the shear layer is not symmetrical as that in an empty test section. The sound propagation path could vary in such a shear flow, which results in differences between signals received at the upper and lower side of the test section. The resolution of the mesh was kept the same as in previous computations, i.e. 7 points per wavelength.

The study was later extended to the computations with a bigger domain, as shown in Fig.4.23b. The domain was extended upstream by  $0.9m$  to include part of the nozzle geometry. Since it was occasionally noticed that the nozzle surface may reflect the sound wave originally going upstream, which would disturb the signals received by the microphones as well. A similar structure was used as the case without nozzle geometry, in order to reduce the grid influence to some degree. The left boundary of the grid between the horizontal nozzle walls was treated as an absorbing sponge layer to avoid the possibility of unphysical reflections. The detailed structure of the rim at the nozzle exit is enlarged in the view at the top corner, whose position in the grid is highlighted by the green circle. To be comparable with the computations in the flow without nozzle surface, a harmonic source at  $1kHz$  and  $10kHz$  was firstly utilized to observe the reflection from the nozzle surface, respectively. It was replaced later by a Gaussian shaped pressure pulse, in order to clarify the surface reflection effect clearly and avoid uncertainties from the potential spurious effects from the sponge layer used to introduce the sound into the field. The details of both source models can be found in Sec.3.2.4.

To quantitatively evaluate the deviation of the received signal caused by the curved shear flow, two regular microphone lines were chosen at  $y_M = 1.1m$  above and  $y_M = -1.5m$  below the test section. The positions were chosen to ensure that the microphone lines do not cross the shear layer and the  $h/y_M$  ratio is close for upper and lower microphone lines in the theoretical correction. The different distances of the microphone lines from the nozzle centerline result from the fact that the airfoil is fixed at  $0.1m$  above the nozzle centerline, where the harmonic source was placed. If the nozzle lip-line is taken as the shear layer centerline, then  $h/y_M = 0.45$  for the upper microphones and  $h/y_M = 0.47$  for the lower microphones.

### 4.2.2 Characteristics of the base flow

As shown in the previous section, the wind tunnel jet experiences a significant curvature when passing over the lifting airfoil, which results in deviations in the shear layer boundaries and centerline from those in the standard correction approach as well as in the empty test section. This section presents the characteristics of such a curved shear flow, in which the locations of the shear layer boundaries are defined according to the way in Sec.4.1.2.

Fig.4.24 shows the velocity lines that define the boundaries and centerline of the shear layer, as well as the horizontal velocity profiles at various sections. Considering the shear layer centerlines on both upper and lower sides in Fig.4.24a, they illustrate an obvious downward deviation starting around  $x = 0.4m$  from the nozzle lip-line. The location corresponds to the leading edge of the airfoil. The shear layer centerlines  $U/U_0 = 0.5$  ( $U$  is the velocity component in  $x$  direction) deviate from the nozzle lip-line obviously as well. The latter one is usually taken as the shear layer centerline in the correction procedure. If the nozzle lip-line is still regarded as the shear layer centerline in the theoretical corrections, a maximum of 40% error will be brought into the calculation for the value of  $h$ . It appears that an oblique shear

layer centerline paralleling to the  $U/U_0 = 0.5$  velocity line will be more suitable as a centerline. Such a hypothesis will be examined in the following sections with numerical results. The horizontal velocity contour and its profiles at three sections are plotted in Fig.4.24b.

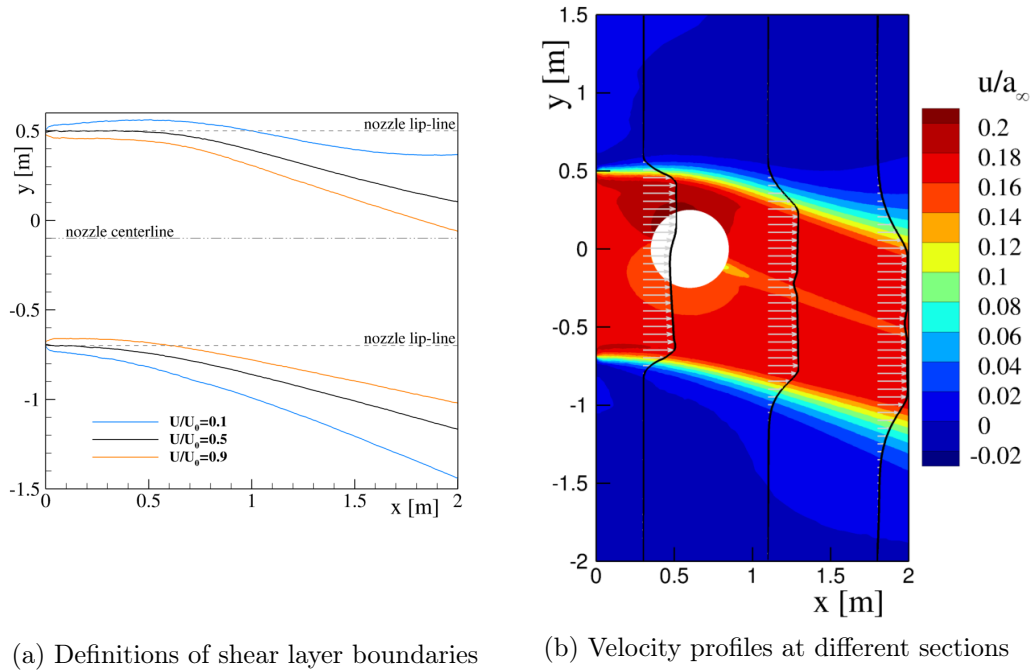


Figure 4.24: Characteristics of the shear flow around the high-lift airfoil.

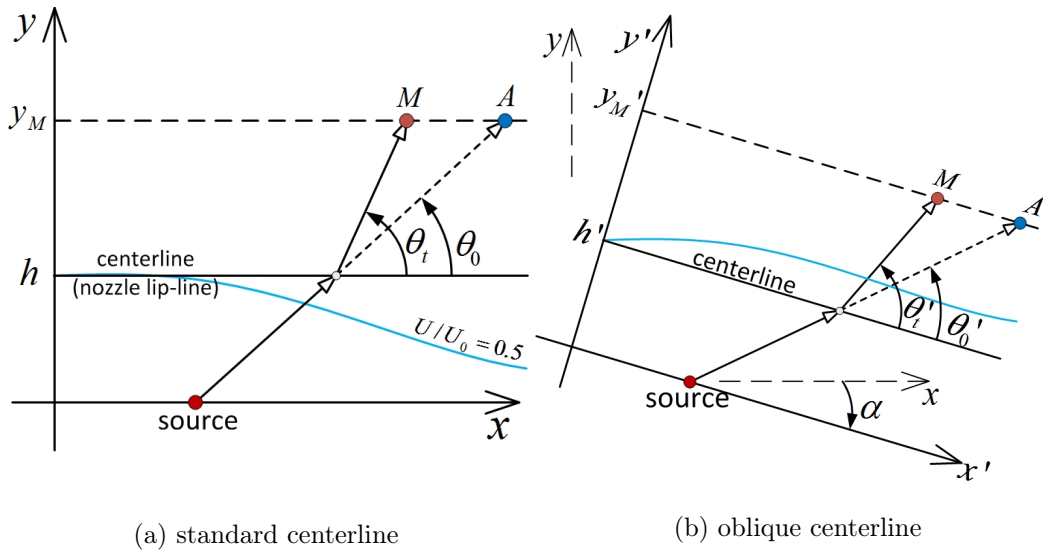


Figure 4.25: Centerline models for the theoretical correction approach.

### 4.2.3 Centerline models applied in Amiet's approach

As already noticed, the general shear layer centerline model applied previously may result in deviations in the theoretical correction method if it is applied in a curved shear flow. Therefore, a modified model was adopted additionally in the theoretical corrections for such a specified situation.

Fig.4.25 gives the sketches of two centerline models that will be applied to the considered case in the correction method. Fig.4.25a is the traditional model used for the previous cases in the shear flow of the AWB with empty test section, in which the nozzle lip-line is taken as the shear layer centerline. Fig.4.25b depicts a modified centerline model, which is parallel to the flow direction as observed well downstream of the position of the source (lifting body respectively). Both of them originates from the nozzle exit since it is easier to define such a centerline in the experiments rather than that overlapping with the practical shear layer centerline (sketched in blue color in both figures). The slope of the oblique model is determined by the geometric angle of attack of the airfoil model ( $\alpha$ ), which is easily obtained since it is provided as an initial parameter in the wind tunnel tests.

The angle and the distance needed in the correction are labelled in Fig.4.25 as well. Their values vary for the different centerline models at the same measurement point ( $M$ ). The corresponding corrected point ( $A$ ) varies as well. To be comparable with the standard centerline model, the pressure amplitude at the corrected position  $A'$  in Fig.4.25b is transformed to the position at equal sideline position in the wind tunnel coordinate ( $x - y$  coordinate) in the following comparisons.

### 4.2.4 Sound propagation through curved shear layers

Knowing the information of the background flow, the sound propagation characteristics through the curved shear flow are investigated. As usual, the computation results are firstly shown as pressure perturbation and intensity level contours to observe the temporary and the averaged sound field.

Fig.4.26 shows the instantaneous pressure perturbation field and the intensity level distribution at  $1kHz$ . The pressure contour does not show many distinguishing features from the previous cases except the convection effect. The convection effect results in an unsymmetric-pattern if one looks at the vertical direction, which is caused by curved flow direction. Total reflection is not observable since the source is located so close to the left boundary that the critical total reflection angle can not be achieved. The intensity level distribution shows a much clearer view of these characteristics in Fig.4.26b. The distribution shows an orientational feature as the reduction of the intensity when the sound wave goes through the shear layer. The practical centerline of the shear layer by definition is indicated by the black curves. When the sound wave crosses the shear layer downstream at a relatively big angle, the intensity shows a strong reduction. This reduction may result from the fact that sound wave experiences a stronger reflection when a large incidence angle is achieved.

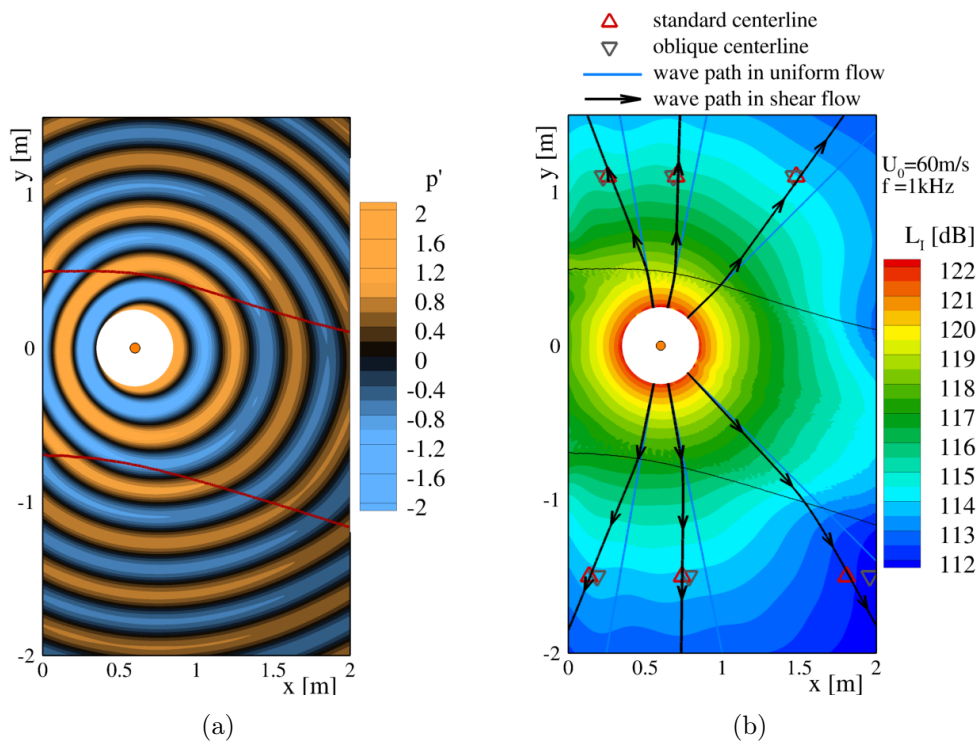


Figure 4.26: (a) Instantaneous pressure perturbation field; (b) Sound intensity level field in the shear flow around the high-lift airfoil for source frequency  $1 \text{ kHz}$ .

Regarding the intensity propagation direction in Fig.4.26b, the arrowed lines represent the propagation path in the curved shear flow, while the blue lines give the path in the uniform flow for corresponding radiation angle. Contrary to the phenomenon observed in the flow field of the empty test section where the vertical velocity is quite small, the radiation paths deviate from the paths in the uniform flow earlier before reaching the shear layer, which results from the increasing velocity in the vertical direction of the background flow field. The deviation becomes more obvious in the propagation direction downstream. The symbols indicate the propagation directions of the transmitted wave derived from the theoretical models. Both predictions obtain very closely located propagation directions outside the upper shear layer, in which the modified oblique model predicts a slightly larger transmission angle. Comparing them with the radiation path in the arrowed curve, the deviation increases slightly compared to the previous cases. Looking at the propagation paths on the lower side, the standard model illustrates a surprisingly good angle prediction compared to the modified model. Values from the oblique model appear slightly farther away from the numerical results. The possible reason of these performances is the contribution from the distance ratio  $h/y_M$ .

Since a quite similar propagation pattern is generated at  $10kHz$ , its sound field is not shown here repeatedly but can be found in the Appendix B for completeness.

#### 4.2.5 Alteration of the sound wave amplitude through curved shear layers

After knowing the sound propagation characteristics as well as the performance of the angle correction for both models, the influences by the curved shear layer and the capability of Amiet's amplitude correction can be quantitatively evaluated next. Fig.4.27 gives the pressure amplitude ratio between corrected position and measurement position. The curves for microphones both above and below the test section are shown. Due to different definitions of the measurement angle in the adopted theoretical correction models (see Fig.4.25), the curves are plotted against the horizontal coordinate of the measurement point instead of  $\theta_M$ . The  $y$ -axis represents again the correction value in  $dB$  that needs to be added to the measurement data. It needs to be mentioned that the  $x$ -coordinate of the corrected point A varies with the applied correction model.

It is noticed that the angle correction predicts the transmitted wave direction with some deviations. The common process based on the theoretical angle correction to obtain the amplitude ratio curve will not be adopted here. Instead, the curve drawn from the computation results (black curve) is obtained in an entire numerical way, which can exclude the deviations caused by the angle correction. Firstly, the intensity propagation paths in both the shear flow and the uniform flow are determined for the same radiation angle, as that in Fig.4.26b. Then their cross points with the microphone line ( $y_M = 1.1m$  or  $y_M = -1.5m$ ) could be fixed, which correspond to the points  $M$  and  $A$  in the theoretical corrections respectively. The pressure perturbation value at these two points are easily extracted from the

numerical results. Then the pressure ratio is obtained for the measurement point M. By applying such a process for many radiation angles, the CAA correction curves in Fig.4.27 could be obtained.

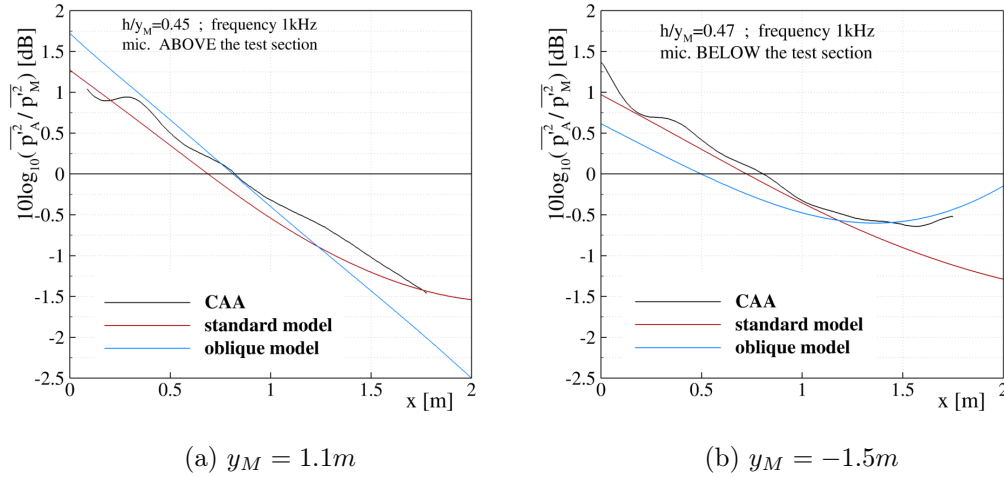


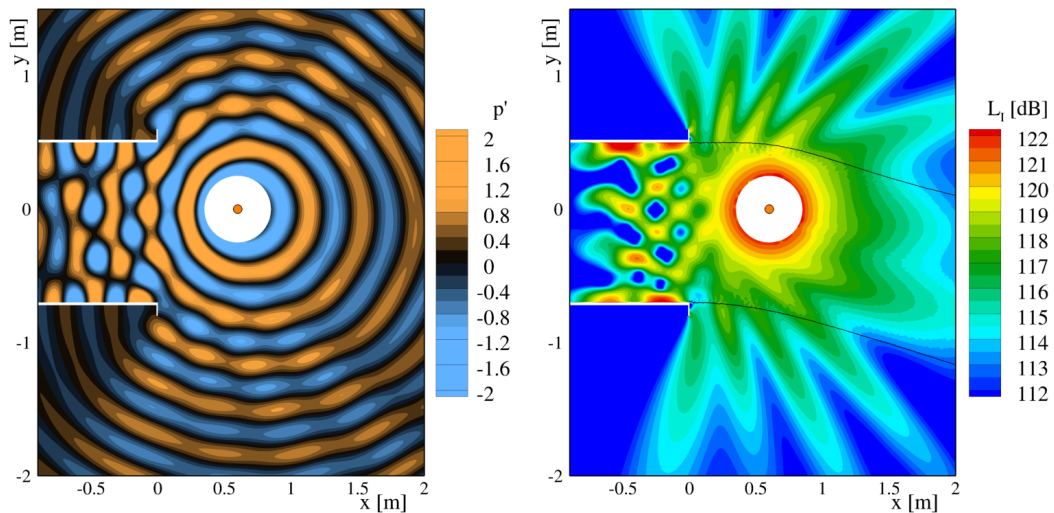
Figure 4.27: Comparison of pressure amplitude ratio between computations and the theory for curved wind tunnel shear layers at  $1kHz$ .

The theoretical curves were obtained once the measurement angle is known, represented by colored curves. Regarding the microphones located above the test section (Fig.4.27a), the CAA results illustrate a distribution generally between the values from the theoretical models in upstream locations, while the correction by the standard model seems to be closer to the CAA results in downstream locations. However, the oblique model has an advantage in predicting the trend downstream, which predicts a downward development rather than an upward trend in the standard model. It could be further validated if a larger computation domain is available. Looking at the data for the microphones on the lower side (Fig.4.27b), it is clear that the data derived from the standard model holds a better agreement with numerical results than the oblique model in upstream locations, which is reasonable since the flow curvature in this range is small and the former one is based on a better angle correction. When the microphone approaches downstream, the oblique model well predicts the trend of the amplitude ratio alteration, which can help to avoid a maximum of about  $0.5dB$  error due to the standard correction approach. Although both models do not show an excellent agreement with numerical results as in previous cases, they could still correct the curved shear layer effect in a reasonably small error range. These two models could be applied simultaneously for wind tunnel tests as currently considered situation, since the theoretical curves drawn from the models can approximate well the shape of the most accurate correction curve (as the black curve) and its possible inflection point.

### 4.2.6 Sound propagation through the curved shear layer considering the nozzle rim reflection

As already introduced, the nozzle surface, particularly the nozzle rim can reflect the wave initially oriented upstream in the wind tunnel tests. The reflected wave will then interfere with the original wave emitted from the source. Naturally, such a reflected wave would exert influences on the shear layer correction as well. The possible deviation caused by it will be investigated in detail in this and the following sections for the same curved shear flow as in the last case.

To be comparable with the computations without nozzle surface, the same harmonic source at  $1kHz$  and  $10kHz$  as in the previous case was firstly utilized to observe the reflection from the nozzle surface. Fig.4.28 gives the instantaneous pressure perturbation field as well as the intensity level field with the black curve showing the  $U/U_0 = 0.5$  velocity line. Fig.4.28a illustrates a regular interference pattern above and below the test section, which is expressed as 'finger' patterns in the intensity level distribution in Fig.4.28b. All these phenomena indicate a strong reflection from the nozzle surface, which manifest itself by a  $6dB$  drop in between the 'fingers' in the intensity level. Since the reflection from the horizontal nozzle surface is expected to be very low due to its reflection direction, it is reasonable to conclude that the reflection is mainly caused by the vertical rim of the nozzle. Obviously, this reflection can severely affect the accuracy of shear layer correction. Additionally, it needs to be mentioned that the interference pattern at the left domain boundary between the horizontal nozzle surface may not be so 'physical' since an absorbing sponge is placed here to avoid reflection from this face.



(a) instantaneous pressure field

(b) time-averaged intensity level distribution

Figure 4.28: Sound field at  $1kHz$  through curved shear layers as nozzle surface included.

As described earlier the analytical sound field of the applied point source model

needs to be introduced through an annular sponge zone around a circular hole in the computation domain. When the sound wave is reflected back towards this zone, it could result in a secondary reflection due to the boundary condition rather than propagation further downstream. This possible reflected wave could interfere with the original wave as well. In order to avoid any uncertainty from potential spurious effects from the sponge zone condition on the nozzle reflection effect, the harmonic source was replaced by a pressure pulse according to Eq.(3.11) at  $\boldsymbol{x}^c = (0.6m, 0)$  with a spatial pulse width of  $b = 0.09$  for the target frequency  $1kHz$  and  $b = 0.009$  for the target frequency  $10kHz$  respectively. The pressure pulse was placed directly into the CAA domain without a grid cut-out or a sponge layer, in order to solve an initial value problem allowing reflected waves to travel freely through the source point. By comparing the computations with the former ones, one can identify whether the grid cut-out for the source significantly alters the (reflected) sound field.

A non-periodic pressure pulse with Gaussian distribution (refer to Sec.3.2.4) was inserted as an initial value into the flow field in the validation computations. The flow velocity in the area where originally the airfoil was located was replaced by a constant flow area, whose values were taken from averaging the mean flow data along the borders of the original grid cut-out. Its numerical results are presented in the next section as SPL along specified microphone lines.

#### 4.2.7 Alteration of sound wave amplitude through the curved shear layer as nozzle surface considered

To identify the influences from the nozzle rim reflection, a convenient way is to compare the data collected along the same microphone lines in the shear flow with and without the nozzle surface. Fig.4.29 plots the SPL value along the specified microphone lines at source frequencies  $1kHz$  and  $10kHz$ . The location of the nozzle surface is indicated at the bottom. The curves are obtained for shear flows with and without nozzle surface, in which the former one is indicated by dashed lines. The solid curves behave as fluctuations around the corresponding dashed curve, which shows a maximum  $3dB$  local increase at  $1kHz$  and about  $5dB$  local increase at  $10kHz$  from the case without nozzle geometry. Note that for this comparison it is reasonable to quantify the amount of the local increase in SPL only. Theoretically, the constructive interference of one perfectly reflected plane wave would yield a maximum increase of  $6dB$ , while a respective perfect cancellation would result in negative infinite SPL levels. This will be further examined by the numerical results for pressure pulse source.

Similarly, the SPL distribution is given for the pressure pulse source in Fig.4.30. Since the source is Gaussian distributed, which can be regarded as a broadband source, the received pressure fluctuation data was transformed from time domain to frequency domain. Then the amplitude distribution can be extracted for single frequencies.

The curve in Fig.4.30 plots the SPL along the microphone line  $y_M = 1.1m$  with and without background flow field. The black curves can be taken as the reference

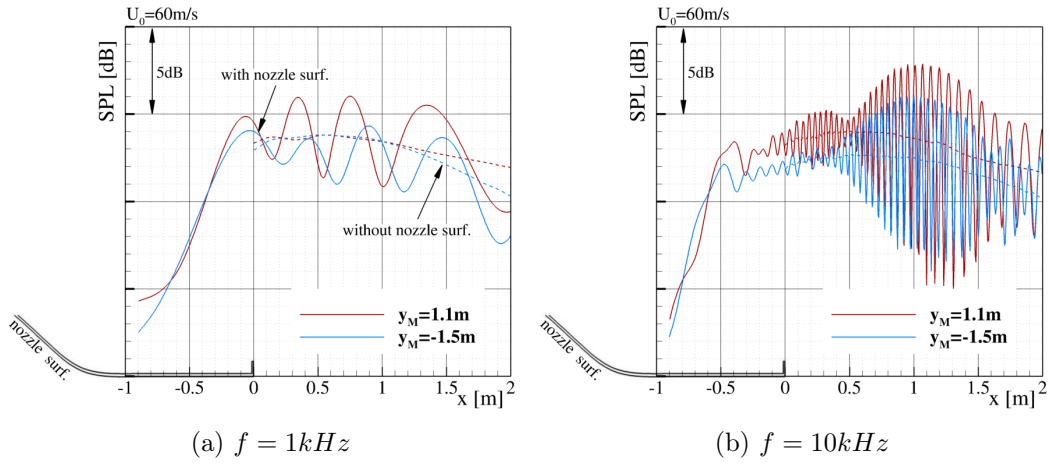


Figure 4.29: Comparison of SPL along microphone lines for computations with and without nozzle surface (harmonic source).

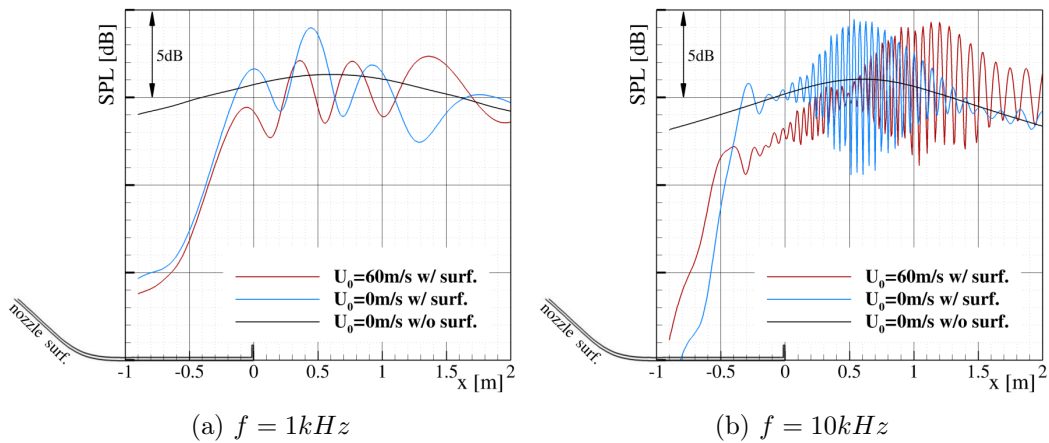


Figure 4.30: Comparison of SPL along microphone lines at  $y_M = 1.1\text{m}$  for computations with and without nozzle surface (pressure pulse).

for the others, which represents the original directivity of the sound source in a non-moving medium free of solid surfaces. The blue curves give the data received in a same quiet medium but with the nozzle surface included, which illustrates a fluctuation around the black curve due to the surface reflection. The data in a shear flow with surface reflection as in the previous case is expressed as red curves, which show less fluctuation range in SPL at  $10kHz$ . Regarding the difference between the black and the colored curves, the reflection itself again results in a maximum  $3dB$  local increase for  $1kHz$  and  $5dB$  local increase for  $10kHz$ . Note that these values as well as the level distribution represented by the red curves correspond remarkably well to the harmonic point source simulation in Fig.4.29. This agreement shows that the influence of the internal sponge zone does not significantly disturb the field at the microphone line considered.

Additionally, some features were noticed during the analysis. The existence of the shear flow appears to push the interference area farther downstream (compare blue and red curves in Fig.4.30). From the numerical results one may conclude that if reflections occur at the nozzle rim, not only the measured amplitude will vary considerably along the microphone line for harmonic signals but spectra will be strongly modified since the interference pattern depends on the frequency. This effect needs to be taken seriously as well if a microphone array is utilized. Another feature is about the setting in the numerical simulation. One should note that for proper comparison it is necessary to use a quite small spatial half width for the Gaussian-distributed source pulse of about a quarter of the wavelength in order to avoid source-wise non-compactness effects. If the source compactness can not be guaranteed, the disturbances from the source itself could result in an unexpected sound pressure level distribution for any specified frequency.

So far the surface reflection due to the nozzle rim was analysed by two different sound sources. The reflection can result in a fluctuation distribution along the microphone line for the single frequency. The effect induced by the surface reflection is closely related to the phase shift between the original wave and the reflected wave. Since currently available correction methods are frequency independent these can not be applied to such a situation. This reflection effect needs further experimental validations as well as numerical studies to obtain appropriate correction.

### 4.3 Sound propagation through analytical shear layers (3D)

The mean flow gradient effect has been intensively investigated in 2D as sound waves get transmitted through a free shear layer. The sound propagation characteristics were analyzed in detail for various background shear flows. Based on available numerical results, the reliability of Amiet's approach was tested and validated, and further slightly modified according to the practical situation. With this background information of the mean flow gradient effect through the 2D shear layer, the study was extended to the 3D computations to explore its influences on the 3D sound

propagation.

This section aims at investigating the 3D sound propagation through a 2D plane shear layer and a 3D rectangularly shaped wind tunnel shear layer of the AWB. The performance of Amiet's approach was tested at various spanwise locations for both shear layer shapes. Moreover, the applicable area of the approach can be determined through such a process.

### 4.3.1 Computational setup

The computations were implemented for both the planar shear flow and the 3D realistic wind tunnel shear flow (rectangularly shaped). The former one was modelled as an extension of 2D shear flow in the spanwise direction with the velocity in spanwise direction being  $0m/s$ . The 2D shear flow was generated by extracting the spanwise symmetry plane along the nozzle centerline in the realistic 3D wind tunnel flow. The spreading shear layer was chosen as the subject instead of constant thickness shear layer since quite a small deviation was observed between them in 2D computations and the spreading shear layer is a more practical sample for the 3D study. The flow field in the test chamber of the AWB with rectangular jet cross section was considered with empty test section to provide a realistic 3D shear flow. Both base flows were obtained at three typical wind tunnel flow speeds, i.e.  $40m/s$ ,  $50m/s$ , and  $60m/s$ . Fig.4.31 gives the horizontal velocity contour at  $U_0 = 60m/s$  for both the planar shear flow and the wind tunnel shear flow. Only a quarter of the wind tunnel flow field was taken as the base flow due to the symmetrical feature of the nozzle (see Fig.4.32a). Its characteristic variation in the flow direction is illustrated in Fig.4.32b, which shows a round corner shape with increasing radius as one goes downstream.

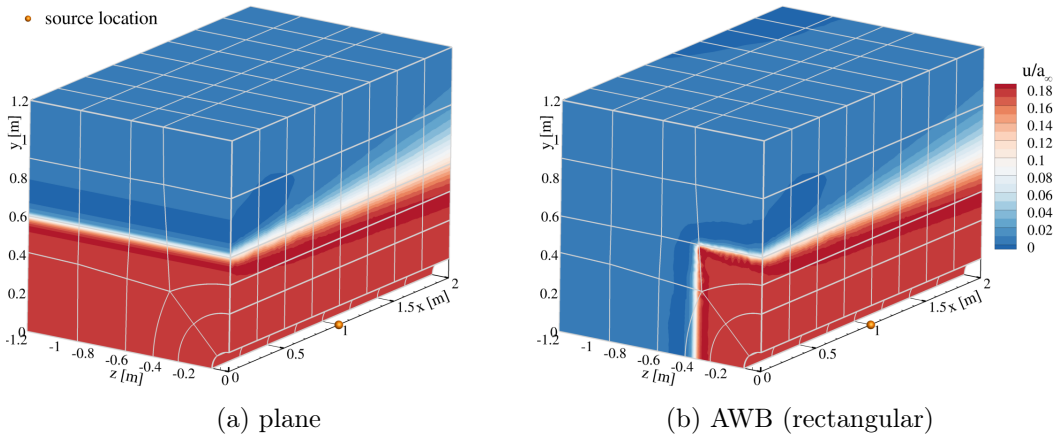


Figure 4.31: Flow field and the computational grids for 3D simulations.

Similar as in 2D computations, a point source (refer to Sec.3.2.4) was placed outside the domain and introduced into the domain by the sponge layer boundary condition. It results in a block structure as shown in grey color in Fig.4.31.

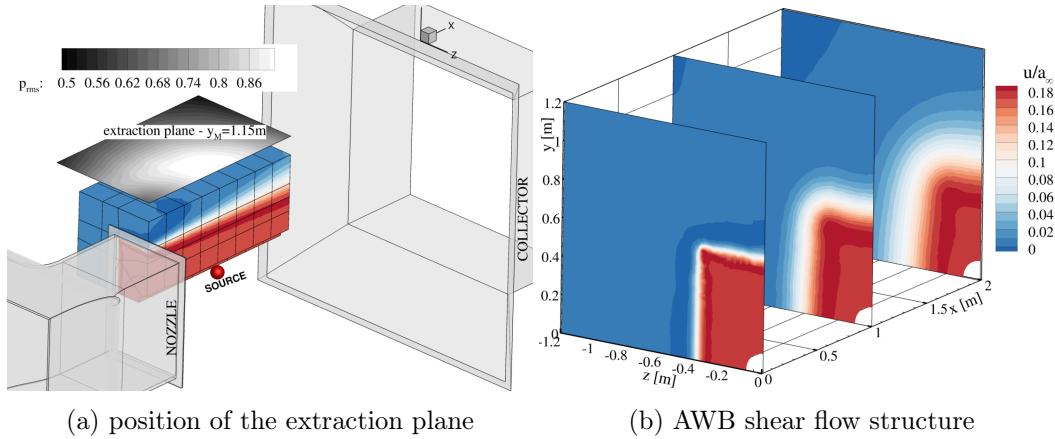


Figure 4.32: Sketch of extraction plane and flow structure in AWB shear flow.

The entire domain is constructed by 152 blocks, of which each contains approximate 200,000 points. The source is located on the nozzle centerline at coordinates  $(1.0, 0.0, 0.0)$ . It is surrounded by a quarter of a cylinder, whose surface is used to introduce the sound wave into the domain again via sponge layer. The domain size is shrunk to  $2m$  in the flow direction and to  $1.2m$  in the vertical direction to reduce the computational effort. The extension in the spanwise direction is chosen to be  $1.2m$  as well. The side surface ( $z = 0$ ) and the bottom surface ( $y = 0$ ) is set to be symmetrical surfaces by the boundary condition. The computations were carried out at three source frequencies, i.e.  $1kHz$ ,  $5kHz$  and  $10kHz$ .

In order to quantitatively determine the amplitude alteration by the shear layer, the pressure perturbation data on the plane  $y = 1.15m$  was extracted from the numerical results, whose location in the domain is shown in Fig.4.32a. The selection of the plane guarantees enough distance from the shear layer and from the domain boundary to minimize the effect of the boundary condition. The SPL distribution on this plane was provided to observe its variation with the flow speed as well as the shear layer shape.

### 4.3.2 Sound propagation through the planar and the realistic wind tunnel shear layers

Different from the 2D sound propagation through the 2D shear layers, 3D sound waves generally feature a divergence of the intensity vector field in the spanwise direction due to the spherical spreading of the sound power. Sound waves emitted in a plane different from the spanwise symmetry plane continue to propagate in different planes after passage through the shear layer due to additional refraction occurring in the spanwise direction. A plane containing both the incident and transmitted waves can not be extracted as in the case when the sound is emitted in the spanwise symmetry plane. Therefore, the instantaneous field will not be presented here. The sound propagation characteristics through the shear layers are introduced by the time-averaged field of the pressure amplitude.

Fig.4.33 gives the SPL distribution on the planes near the domain boundaries, whose position in the computation domain is indicated in Fig.4.33a by the shaded rectangles. The contour is not given directly on the boundary of the domain since the applied boundary condition may cause slight deviation. The corresponding root mean square value of the pressure perturbation was calculated by averaging the results in thirty wave periods after transients left the domain. Fig.4.33b plots the reference SPL distribution for the sound propagation in the uniform flow, which is the target distribution of the shear layer correction in the wind tunnel tests. Fig.4.33c illustrates the distribution as the sound waves transmit through a planar shear layer, whose center plane is located at  $y = 0.6m$ . Looking at the side plane ( $z = -1.15m$ ), the protrusion part towards upstream results from the total reflection similar as observed in the 2D cases. The same reason leads to the distribution on the front plane ( $x = 0.05m$ ). Next, the sound propagation in the real wind tunnel flow is considered in Fig.4.33d. The shear layer center planes are located at  $y = 0.6m$  and  $z = -0.4m$  respectively and intersect along the line  $(x, 0.6, -0.4)$ . Due to the multiple effects from these two shear layers, the protrusion pattern due to total reflection in the planar shear layer does not appear on the lateral side plane. Instead, it shows a quite distinctive distribution on the front plane, which has a high SPL area inside the shear layer. This is a result from the total reflection by both shear layers. Both the upper and the side shear layer would reflect the sound waves back into the jet flow in particular at this far upstream location. These reflections cause an interference pattern as observed in the figure. Besides, the total reflection happens at a smaller polar radiation angle  $\theta_0$  for the side shear layer than the upper shear layer, since it corresponds to a smaller  $h/y_M$  distance ratio.

Another distinctive feature in Fig.4.33d is the protrusive distribution in the area  $y > 0.6m$  on the front plane as well as the similar distribution on the top plane. Such areas are already beyond the shear layer, which could not be induced by the total reflection by the shear layer. This characteristic of sound propagation is relevant with the shear layer shape considered in the current study. As the flow goes through the AWB wind tunnel, a rectangular shear flow is generated, as shown in Fig.4.31b and 4.32b. When sound waves propagate through such a shear layer, the refraction is determined by the superimposed influences of top and side shear layers. The superimposition expresses a 'focusing' effect upstream and a 'spreading' effect downstream, as sketched in Fig.4.34. The sound transmissions through the upper shear layer are illustrated by solid curves, while the transmissions through the side shear layer are plotted by dashed curves. This feature is determined by the directions of shear layer refraction around the corner part. One may notice that the SPL on the side plane in Fig.4.33d was not altered too much by such a rectangular shear layer. It could be attributed to the size of the nozzle and refraction direction. This feature will be discussed in more details in the following section.

Similarly, the SPL distribution on these planes was plotted at the source frequency  $10kHz$ , as shown in Fig.4.35. The sound propagation in the planar shear flow shows a similar pattern as that at  $1kHz$ . The 'focusing' effect in the AWB shear flow results in a more pronounced and sharper distribution as the frequency

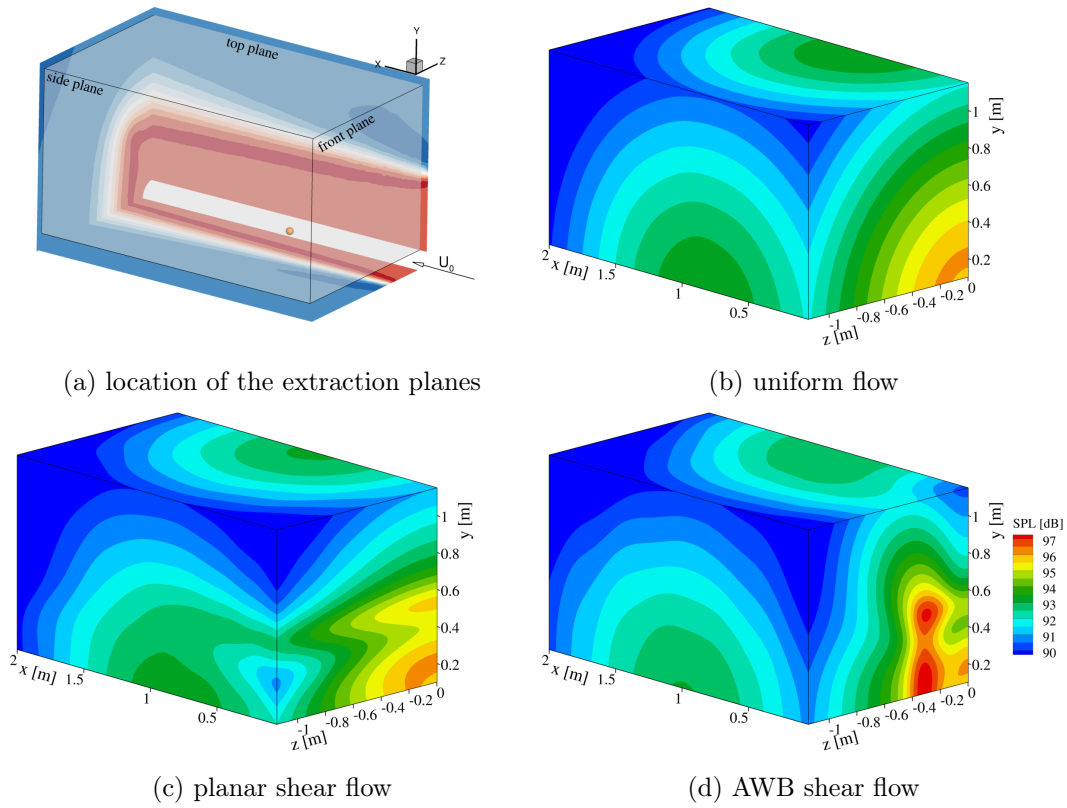


Figure 4.33: Far-field SPL distribution under various flow conditions at  $U_0 = 40\text{m/s}$ ,  $f = 1\text{kHz}$ .

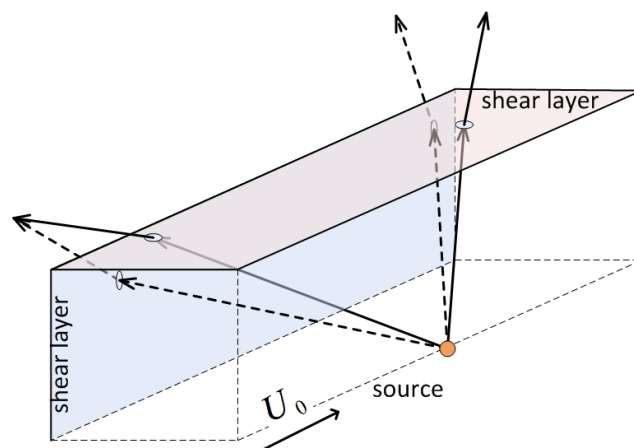


Figure 4.34: Sketch of 3D rectangularly shaped shear layer effects.

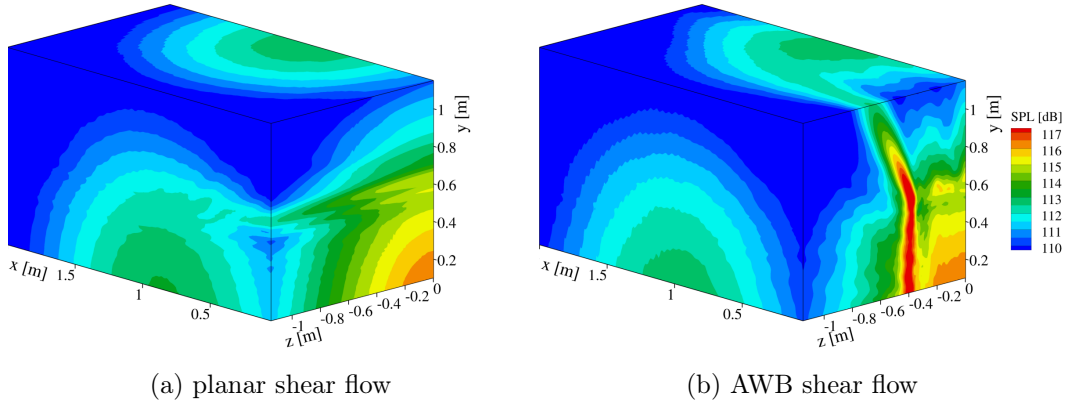


Figure 4.35: Far-field SPL distribution under various flow conditions at  $U_0 = 40m/s$ ,  $f = 10kHz$ .

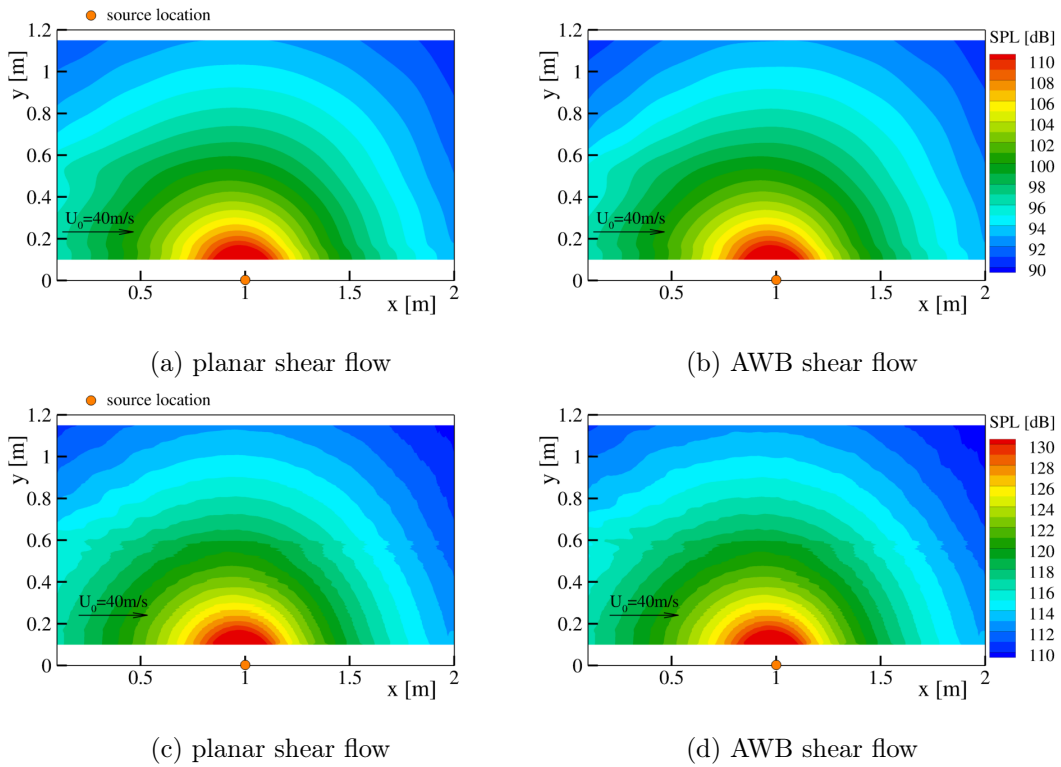


Figure 4.36: SPL distribution on the symmetry plane ( $z = 0$ ) under various flow conditions at  $U_0 = 40m/s$  ( $a \sim b : f = 1kHz; c \sim d : f = 10kHz$ ).

increases. The affected area shrinks to a smaller range comparing with  $1kHz$  but increases in the amplitude.

The SPL distribution is given on the symmetry plane of the wind tunnel test section as well. The symmetry plane is identical to the plane in the studies of the sound wave propagation in the 2D shear flow. By observing the distribution on this plane, the 3D shear layer effect can be identified for the symmetry plane. Fig.4.36 presents the SPL contour in the shear flow with  $U_0 = 40m/s$  for both the planar shear layer and the AWB shear layer. Comparing with the 2D cases, the intrusive structure caused by the total reflection upstream is only slightly observable due to the shrink of the computational domain. Looking at the distributions at  $1kHz$ , it shows a weaker total reflection in the AWB shear flow. This could be caused by the interference between the incident wave and the reflected wave from the side shear layer.

Fig.4.37 gives the SPL distribution on the surrounding planes in the shear flow at  $U_0 = 60m/s$ . Comparing with Fig.4.33, a stronger reflection is observed in the distribution as the flow speed raises up. This is coincident with the phenomenon observed in 2D computations. The aforementioned 'focusing' effect shows up as an extended high SPL area on the front plane in Fig.4.37b. Fig.4.38 shows the same trend at  $10kHz$ . By the comparison of these contours, it is concluded that a strong relevance of the source frequency and the flow speed in the 3D shear layer effect, which should be further studied.

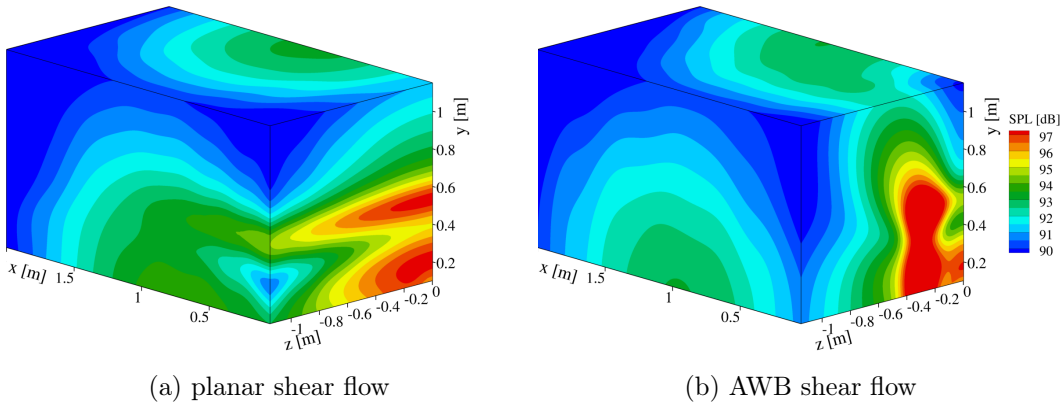


Figure 4.37: Far-field SPL distribution for various flow conditions at  $U_0 = 60m/s$ ,  $f = 1kHz$ .

Similarly, the SPL distribution is given on the symmetry plane, as in Fig.4.39. The SPL difference around the total reflection is more obvious between the two shear flow types at  $1kHz$ . The deviation between the distributions in the planar shear flow and the AWB shear flow indicates again the influences from the side shear layer in the AWB. The interference between the incident wave and the reflected wave from the side shear layer could result in an amplitude variation on the symmetry plane, which is more obvious upstream since the reflection here is stronger.

As done in the 2D analysis, the sound intensity propagation paths can be de-

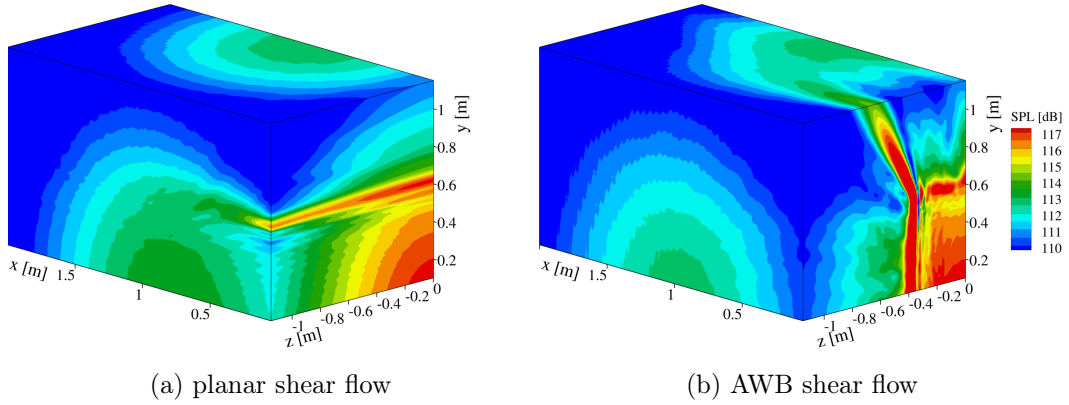


Figure 4.38: Far-field SPL distribution for various flow conditions at  $U_0 = 60m/s$ ,  $f = 10kHz$ .

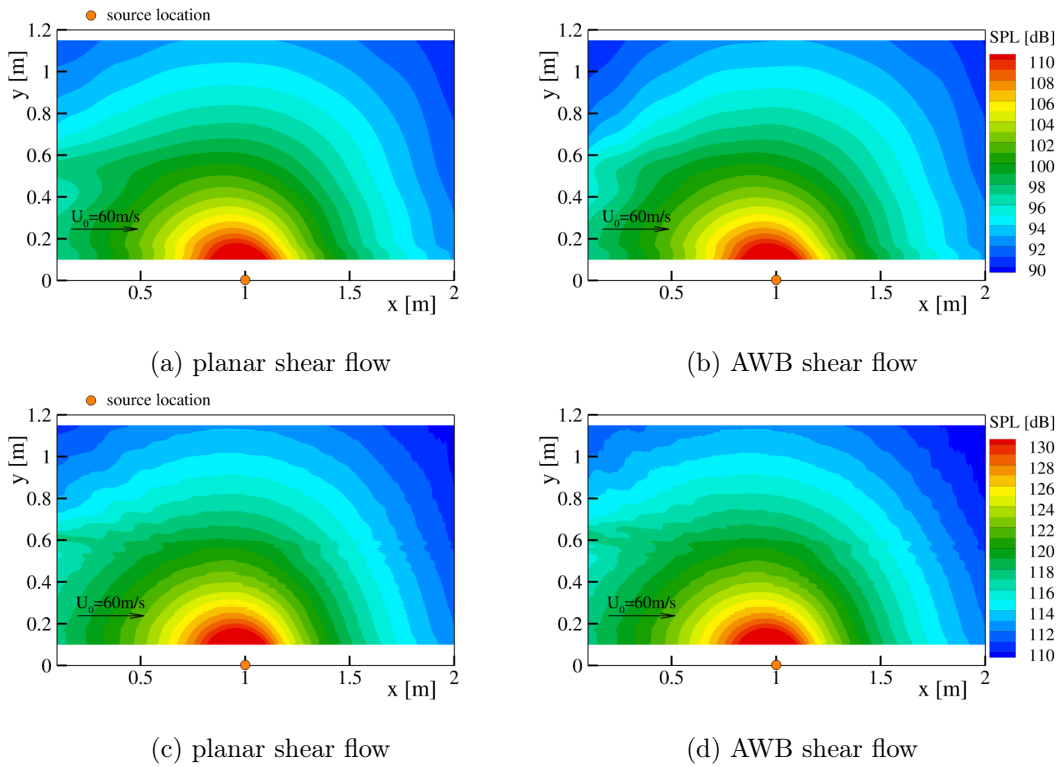
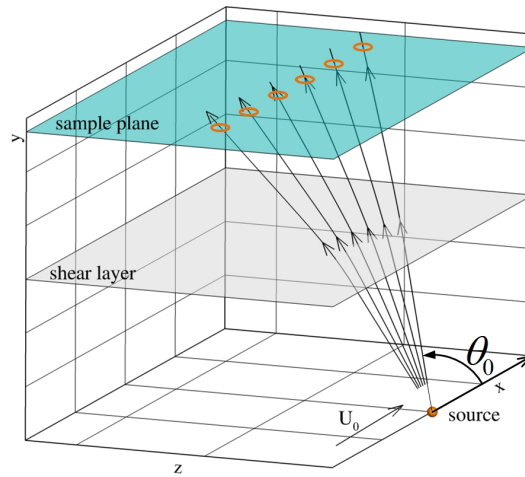


Figure 4.39: SPL distribution on the symmetry plane ( $z = 0$ ) for various flow conditions at  $U_0 = 60m/s$  ( $a \sim b : f = 1kHz; c \sim d : f = 10kHz$ ).

terminated from the computational results in both the shear flow and the uniform flow. By comparing them with the theoretical angle correction, the performance of Amiet's approach can be evaluated in the 3D applications. Since the transmitted wave radiates in a different plane from the incident wave, the paths are not given in the form as in 2D cases but in another way. The path for each radiation angle is given as the intersection point of the intensity propagation path with the specified sample plane ( $y = 1.15m$ ). Once the corresponding radiation angle is fixed, the position of the theoretical intersection point with the sample plane can be derived from Amiet's angle correction. Finally, the deviations between computations and the theoretical predictions can be identified.

The comparison was carried out simultaneously for both the planar shear layer and the AWB shear layer, which is helpful in the validation of the correction approach (for the planar shear layer) as well as the observation of the 'corner' effect in AWB wind tunnel flow. Fig.4.40a illustrates the extraction process of sample points from the computational results, where the orange circles give the location of intersection points for each radiation path. The source position projected on the sample plane is illustrated by the orange circle. The points distribution on the sample plane is given for open jet flow speed  $40m/s$  and  $60m/s$  in the other two figures. The traces are plotted for radiation angles distributed at three spanwise locations, which are  $z = -0.2m$ ,  $-0.6m$  and  $-1.0m$ . The colorful symbols in the figure represent the propagation direction for the same radiation angle in various shear flow, while the black symbols give the corresponding theoretical locations.

Regarding the trace distribution in the planar shear flow, it shows a good agreement with the predictions of the theory, with the deviation slightly larger in the spanwise direction. The more the polar angle  $\theta_0$  differs from  $90^\circ$ , so does the deviation at positions  $z = -1.0m$ , especially in the upstream locations. The reason for this effect on the deviation has been presented in the 2D cases, which is due to the finite thickness of the shear layer. When the sound wave radiates in a polar angle different from  $90^\circ$ , the local distance, which the sound is travelling through the shear layer increases as well. During the travelling period in the shear layer, the flow velocity effect are more obvious than that for an infinitely thin shear layer. This effect is also applicable for the explanation of downstream deviation. The maximum deviation happens in the upstream location at  $z = -1.0m$  in the flow at  $U_0 = 60m/s$ , with a value around  $0.05m$ . This value corresponds to a deviation of the transmission angle of approximately  $5^\circ$  (derived by  $\Delta\alpha = \Delta r/0.55$ ). Similarly, the traces in the 3D AWB shear flow are plotted, in which the distribution around  $z = -1.0m$  is in absence since the intensity paths crossing through this part is refracted from the side shear layer instead of the upper shear layer. As the sampling points move far away from the source point in the spanwise direction, the deviation between the computations and the theoretical predictions increases sharply in both upstream and downstream. The sequence at  $z = -0.6m$  is around the area where the focusing effect was observed in the previous contours, where an apparent deviation is noticed from the other two data series. Obviously, as the sound wave transmits through a rectangular shear layer, its local propagation direction is altered as well.



(a) sketch for sample plane ( $y = 1.15m$ )

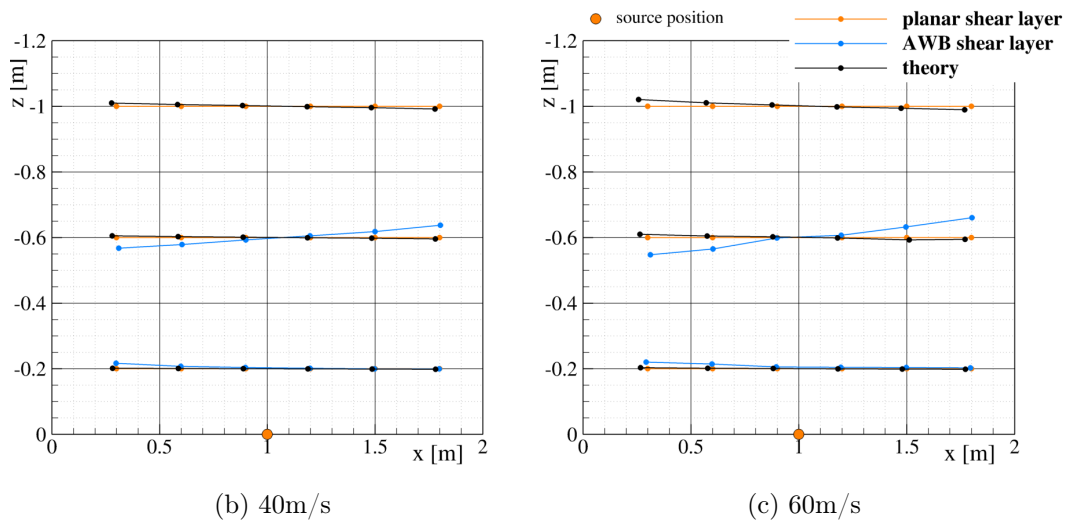


Figure 4.40: Comparisons of transmitted wave direction between computations and theory at source frequency  $1kHz$ .

In the upstream locations, such deviation could be caused by the aforementioned 'corner' effect. Since the intensity propagation direction is determined by the local intensity vector (refer to Sec.3.4), the direction drawn for the trace is actually a synthesis of two transmitted wave which crossed with each other at this point if the 'corner' effect happened. In downstream, it is speculated that the deviation could result from the round shear layer shape.

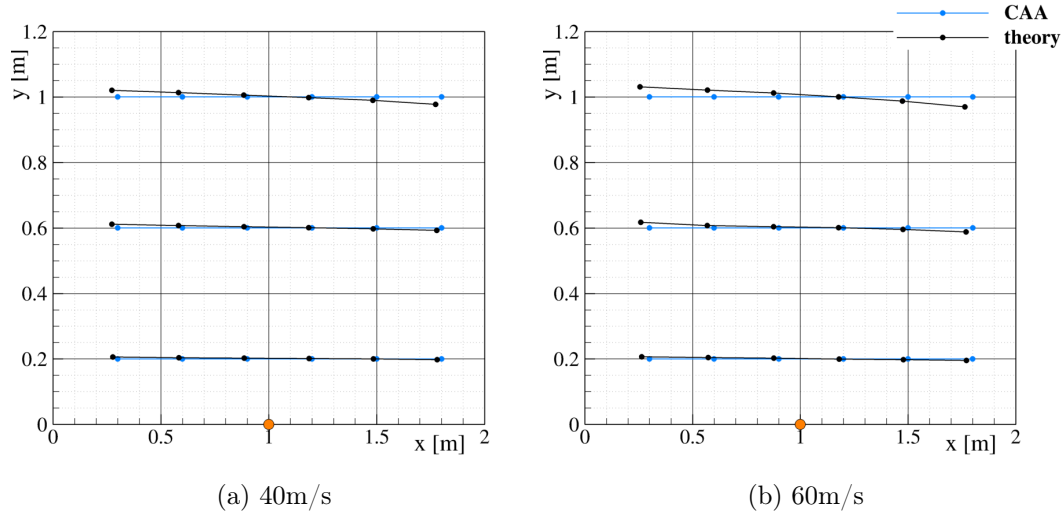


Figure 4.41: Comparisons of transmitted wave direction between the computations and the theory at source frequency  $1kHz$  in side plane  $z = -1.15m$  (AWB shear flow).

Similarly, another sample plane was chosen to observe the sound propagation through the side shear layer. The plane is parallel to the side shear layer center plane, locating at  $z = -1.15m$ . By implementing the same approach as above, the projection of the sound wave propagation trace on the sample plane was derived and given in Fig.4.41. It illustrates a much better coincidence between the computations and the theory, even at locations far away from the source. The maximum deviation is equivalent to that in the correction of the planar shear layer. Such a small deviation is coincident with the SPL distribution on the side plane in the contour figures, where the SPL shows a regular distribution without being altered by the shear layer significantly. This relative insensitivity compared to the considered  $y$ -plane is due to the smaller distance of this shear layer to the source and its larger size. Looking at the SPL distribution on the front plane in the wind tunnel flow (Fig.4.33d, 4.35b, 4.37b, 4.38b), it is clear that the aforementioned 'corner' effect is limited to a certain angle range, which is relevant to the size of the nozzle shape. If the observer stands out of this region (as the side sample plane), the received signal only experiences the regular refraction effect by the side shear layer. This finding is useful for our analysis of amplitude correction since it provides the 'safe area' of Amiet's correction in the considered wind tunnel flow.

So far the sound wave propagation in the 3D shear layers has been qualitatively

investigated for a point source, accompanied by the validation of Amiet’s angle correction. It shows a good agreement with numerical results in the planar shear flow with the maximum deviation appearing at the farthest spanwise location. Knowing this information, it is proceeded further to the study of the sound wave amplitude alteration through the 3D analytical shear layers in the next section.

4.3.3 Alteration of the sound wave amplitude through 3D analytical shear layers

As mentioned earlier, in order to figure out the amplitude alteration caused by the shear layer, the SPL distribution on a plane ( $y_M = 1.15m$ ) outside the shear layer was extracted from the computational results for the sound propagation through planar shear layers, rectangular shear layers as well as in the uniform flow.

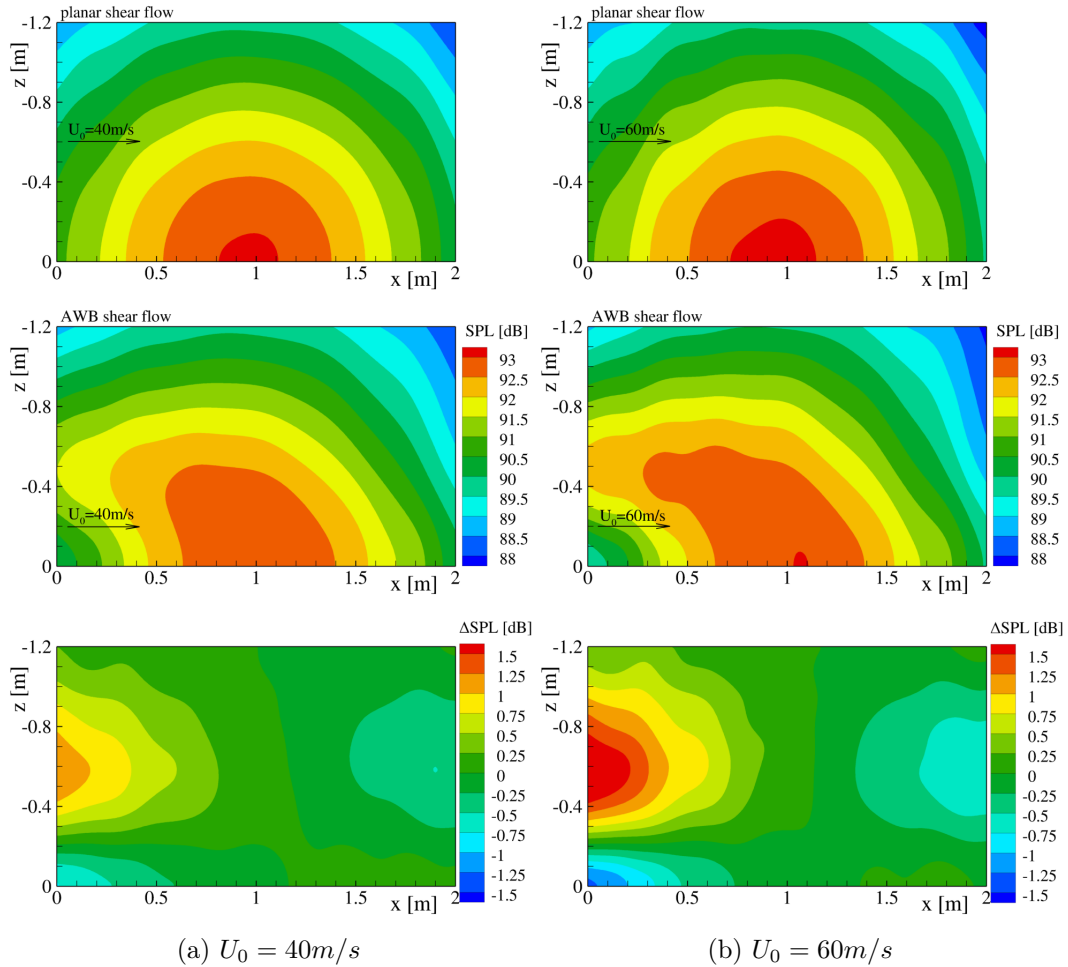


Figure 4.42: SPL distribution on the extraction plane  $y_M = 1.15m$  ( $f = 1kHz$ ).

The SPL distribution is firstly given for the source frequency  $1kHz$  in the shear flow at two flow speeds, as shown in Fig.4.42. The figures in the first row plot the distribution for the sound transmission through the planar shear layer, while the

figures in the second row are the distribution in the corresponding AWB shear flow. The flow direction is along the  $x$ -axis, as indicated in the figures. The focusing effect due to the 3D shear layer shape can be easily observed in the figures for the AWB shear flow by the distortion of the level contour lines towards upstream at about  $z = -0.5m$  (indicating level increase). Note that the upstream levels near the plane of symmetry ( $z = 0$ ) also change significantly, but here they show a reduction compared to the planar shear layer. This remarkable effect was already seen in the upper right corner of Fig.4.37b. First of all, this shows that even in the symmetry plane  $z = 0$  the three-dimensionality of the AWB shear layer shows an influence, which can not be captured by a 2D shear layer. Obviously, there is a reflection of the side shear layer and a corresponding destructive interference effect at work. This explanation is supported by the fact that this phenomenon is frequency dependent as a comparison with Fig.4.38b shows. As usual all effects become more significant as the flow speed increases. Comparing with CAA results at  $U_0 = 40m/s$ , more energy is refracted to the upstream direction in the higher speed shear flow. The spreading effect in the downstream direction seems not so strong as the focusing effect. Its intensity can be observed in the bottom row of Fig.4.42. It was obtained by subtracting the SPL distribution in the planar shear flow from that in the AWB shear flow. The  $\Delta$ SPL distribution clearly verifies the 'corner' influence in upstream and downstream directions as well as the level reduction upstream near  $z = 0$ . Besides, they present the deviation caused by the 3D shear layer effect, which increases with the flow speeds and approaches to maximum  $1.5dB$  at the source frequency  $1kHz$ .

The similar distributions can be given at  $10kHz$  as well, shown in Fig.4.43. A much stronger 'corner' effect is observed. The deviation between the AWB shear flow and the planar shear flow increases considerably, up to  $3dB$  at  $U_0 = 40m/s$  and  $5dB$  at  $U_0 = 60m/s$ . The deviation caused by the 'spreading' effect increases as well, up to around  $1dB$ . At the same time, it is noticed that the 'focusing' point moves outward in the negative  $z$  direction as the frequency increases, which could be related to the phase shift between the intersecting sound waves refracted from the upper and side shear layers. This feature does not vary with the flow velocity.

The above comparisons provide the basic characteristics of the shear layer shape effect as well as the affected region. Although the deviation caused by the shear layer shape increases obviously with the source frequency, the corresponding affected area becomes narrower. This makes it possible to obtain a reasonable shear layer correction across a 3D rectangularly shaped shear layer with a proper treatment around the corner part. This possibility and its application region will be discussed in the following part of the amplitude correction application.

As done in the curved shear layer case, the independent numerical amplitude ratio ( $\overline{p_A^2/p_M^2}$ ) was derived without searching for the help of the angle correction. The same procedure was applied here to plot the numerical amplitude ratio curve: for a specified radiation angle, its radiation paths in both uniform flow and shear flow are determined from the intensity field. Then their intersection points with the sample plane  $y = 1.15m$  are fixed, of which the pressure amplitudes can be extracted

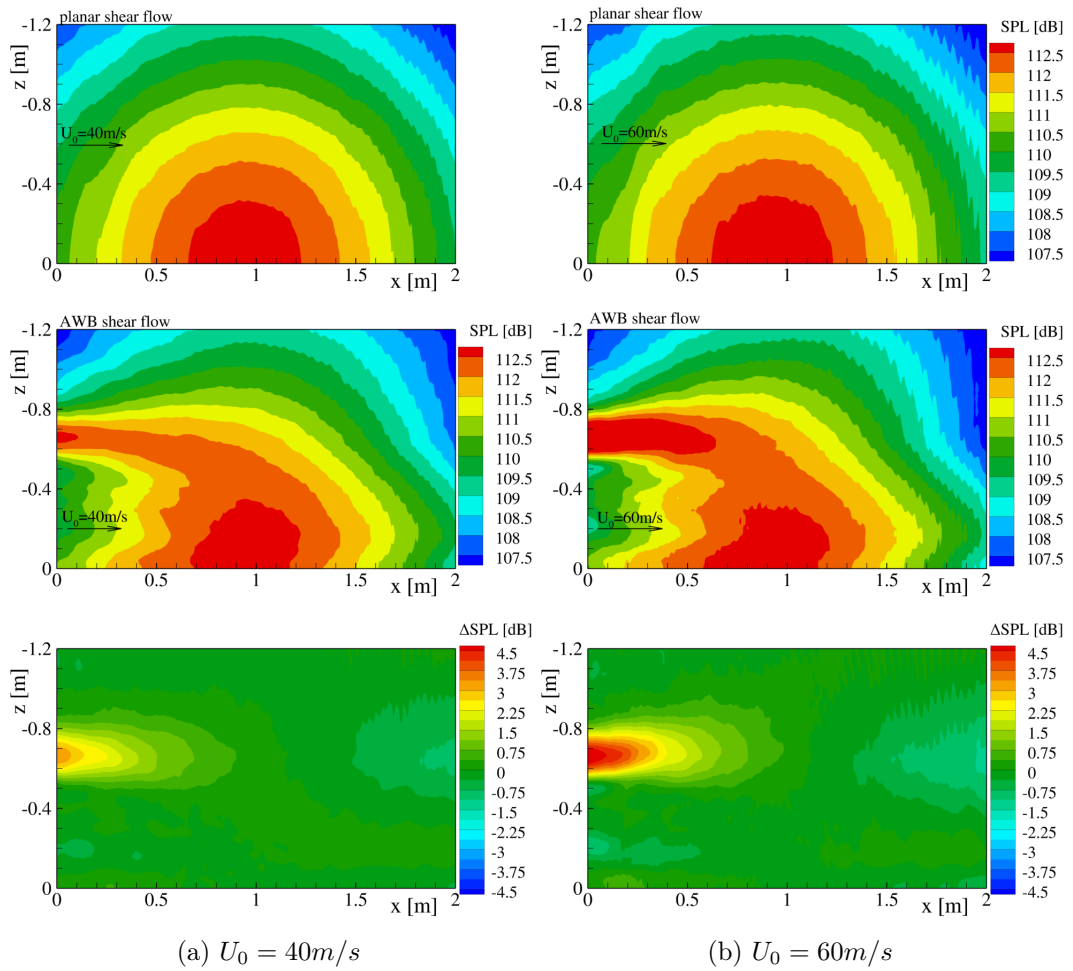


Figure 4.43: SPL distribution on extraction plane  $y_M = 1.15\text{m}$  ( $f = 10\text{kHz}$ ).

from computational results to plot the amplitude ratio curve. Such a process avoids the deviations induced by the angle correction if the corrected position  $A$  is given by the theoretical angle correction.

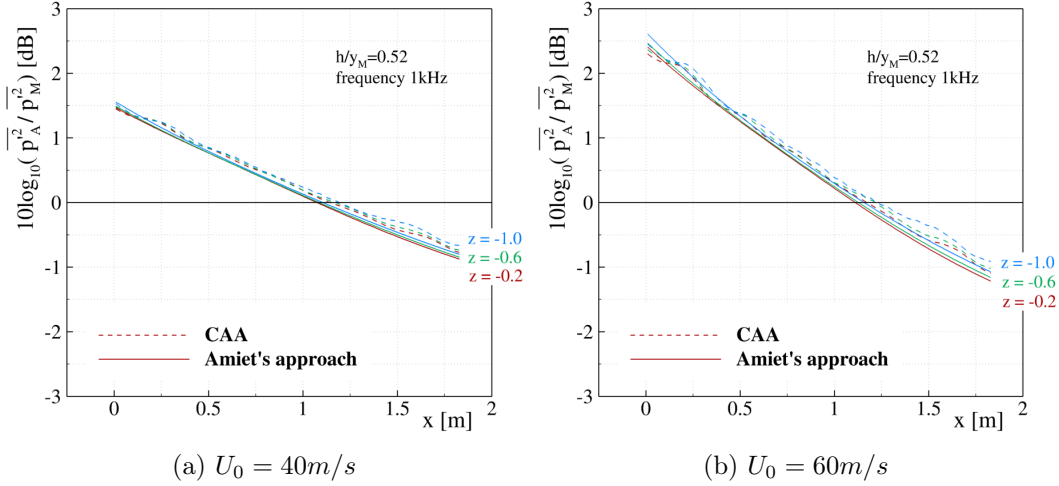


Figure 4.44: Amplitude ratio comparison between the theory and the computations at  $f = 1 \text{ kHz}$  through planar shear layers.

Fig.4.44 plots the amplitude ratio at  $f = 1 \text{ kHz}$  through the planar shear layers for the observer's positions at various spanwise locations. These spanwise locations are identical to that in the validation of the angle correction. The measurement positions were chosen at each same spanwise location along the line, which is indicated in the figure as their coordinates in the  $z$ -axis. With the increasing distance from the source point, the correction curves show small variation, while the theory predicts a slightly stronger shear layer effect in the alteration of the sound wave amplitude. The deviation goes up with the flow velocity. Generally, the theoretical curves show a good agreement with the numerical curves.

Fig.4.45 gives the amplitude correction curves for the sound transmission through the rectangular shear layers, which share the same measurement positions as in the planar shear flow. When the observer position is chosen close to the symmetry plane  $z = 0$  ( $z = -0.2 \text{ m}$ ), where it is essentially out of the affected area by the 'corner' effect, the deviation between computations and the theory is similar to that in the planar shear layer. As the observer moves further from the source, the correction curve from computations shows a quite different distribution from that through the planar shear layers. The accuracy of the angle correction is part of the reason for such a phenomenon. Another reason is the 'corner' effect mentioned earlier. In the upstream locations, the energy loss due to the effect from upper shear layer could be compensated by the refracted wave from the side shear layer, then further reduces the correction value. In the downstream direction, the spreading effect reduces the local pressure amplitude, which results in a smaller correction value. Such an obvious deviation in the further spanwise locations are expected since it was presented that the sound wave propagation through the upper shear layer can

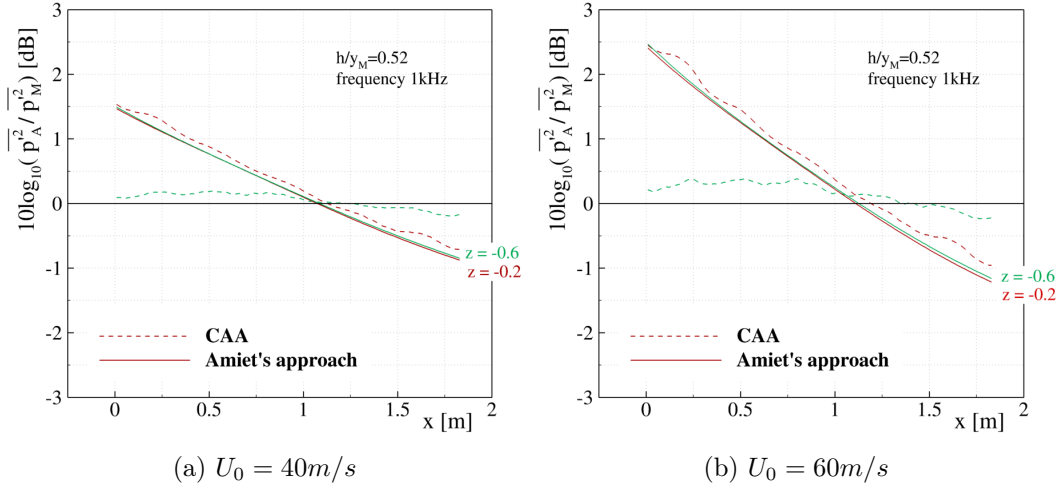


Figure 4.45: Amplitude ratio comparison between theory and computations at  $f = 1\text{ kHz}$  through AWB shear layers (top plane).

not be well predicted by the theory. In the following, the amplitude correction curves are plotted at several vertical locations outside the side shear layer, where the sound wave did not experience an obvious 'corner' effect according to the previous comparisons.

Fig.4.46 plots the amplitude correction curve for the sound transmission through the side shear layer in the AWB shear flow. As expected, the computational correction curves show a quite similar trend as that in the planar shear flow, with a slight difference in the upstream locations. Generally, they show identical features as observed in the planar shear flow, which illustrate slow variation with the distance from the source. Therefore, the side plane can be taken as a 'safe area' out of the 'corner' effect, where the measurement data needs only to be corrected for the shear layer refraction effect under the currently considered situation. It should be mentioned that the side plane should be chosen at locations  $h/y_M < 0.5$ , since beyond this region the measurement data could still be altered by the 'corner' effect even at side plane, as observed in Fig.4.33d, 4.35b, 4.37b and 4.38b.

So far the 3D sound transmission through the planar and the rectangular shear layer have been systematically explored. The pressure amplitude outside the shear layer was extracted from the numerical results to analyze the role of the flow velocity, the source frequency as well as the shear layer shape in the shear layer effects. Additionally, the performance of the correction was examined in both the planar and the rectangular shear layers. The theory shows an increasing deviation as the observer moves far away from the source point. The 'corner' effect was validated and its affected region was identified, which could help to avoid the corresponding error in the experimental work. In the following part, another important factor in the free shear layer will be taken into account, i.e. the turbulence part. As usual, the work is begun with the 2D computations.

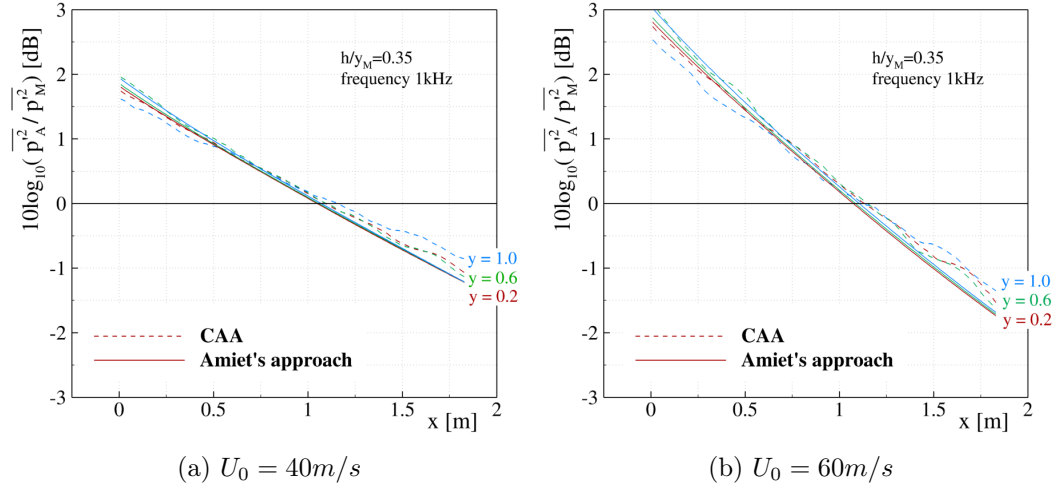


Figure 4.46: Amplitude ratio comparison between the theory and the computations at  $f = 1kHz$  through AWB shear layers (side plane).

## 4.4 Sound propagation through turbulent shear layers (2D)

In the previous sections, the study focused on the effects induced by the mean flow gradient through the free shear layer, in which the turbulence part was ignored. Such a separate treatment is helpful to identify the respective effect from the mean flow gradient and the turbulence. The latter one is of concern in this part. As introduced in the first chapter, the turbulence part plays an important role in the alteration of sound propagation characteristics, whose effect is usually named as scattering. Its influences express not only as the change of the sound wave direction and amplitude, but also in the frequency band. The alteration in the frequency band is referred as frequency scattering or haystacking. Both effects will be investigated numerically in 2D in this section. The turbulence part was reconstructed stochastically by the FRPM method from the RANS results, as introduced in Sec.3.3. In its 2D application, two components of the velocity fluctuations in the plane of interest are extracted from the complete stochastic turbulence representation, avoiding the possible unphysical velocity fluctuations in a 2D 'turbulence' simulation.

### 4.4.1 Computational setup

The computations were implemented in two types of the turbulent shear flow. The first one is the turbulent shear flow with constant thickness, which differs from the linear shear flow adopted in Sec.4.1. The background flow was generated by the extension of a slice extracted from the 2D AWB shear flow ( $U_0 = 60m/s$ ) at the location where the thickness  $\delta = 0.3m$ . Both the mean flow and the turbulent data at the slice were applied to give the information for the extended 2D turbulent shear flow. Such a turbulent shear flow does not physically exist but can help to

provide the information of the sound propagation through the turbulent shear layer without any other influences. Besides, the computational domain of such a flow field is not limited as that of the 2D AWB shear flow, so that the sound propagation characteristics around the extreme angles could be analyzed. The second type is the 2D turbulent shear flow in the AWB wind tunnel, which owns the same properties as that in Sec.4.1 but with the turbulence part added.

The computational grid employed for the constant thickness shear layer in Sec.4.1 was again applied for the turbulent shear flow with constant thickness here, whose domain size is  $10m \times 2.1m$ . The computational grid for the 2D wind tunnel turbulent shear flow is the same as that in Sec.4.1 for the AWB shear flow, which has the size of  $3m \times 2.1m$ . The characteristics of the corresponding mean flow field are not repeated here. The data of the turbulence part was added to the domain with additional grids, which is named as 'patch' in the current study. The patch lies over the previous CAA grid in the shear layer region, containing the averaged turbulence statistics from the CFD simulations. Five overlapped patches were generated to represent the turbulence stochastically. They could be assigned to different processors to reduce the computation time significantly. Fig.4.47 gives the turbulence kinetic energy (TKE) distribution for both cases. In the overlapping area, a weighting function was applied for every two neighboring patches to make sure that the summation of the TKE in this region equals to the original value from the RANS solution.

The 2D harmonic source used in the previous computations was still applied in the current cases. It was employed to generate periodic sound waves at three frequencies  $5kHz$ ,  $7.5kHz$  and  $10kHz$ . Tab.4.3 lists the conditions considered in the CAA simulations. The frequencies and the flow speeds were chosen to observe the variation of the scattering effect with them, as presented in Candel's experiments [S. Candel 1975]. The other settings were kept exactly the same as in the previous study of the mean flow gradient effects. Therefore, the variation of the sound wave amplitude due to the turbulence can be easily determined by the following comparisons.

Table 4.3: Conditions for shear layer scattering effects (2D).

shear layer type	flow speed ( $m/s$ )	domain size ( $m \times m$ )	source frequency ( $kHz$ )
constant	60	$10 \times 2.1$	5, 7.5, 10
spreading	40, 60	$3 \times 2.1$	5, 7.5, 10

Similar as done in the previous cases, a microphone line was chosen outside the shear layer at  $y_M = 1.2m$  to monitor the pressure fluctuation. The spectra of the received signals was compared with the corresponding data in the uniform flow and the shear flow without the turbulence part.

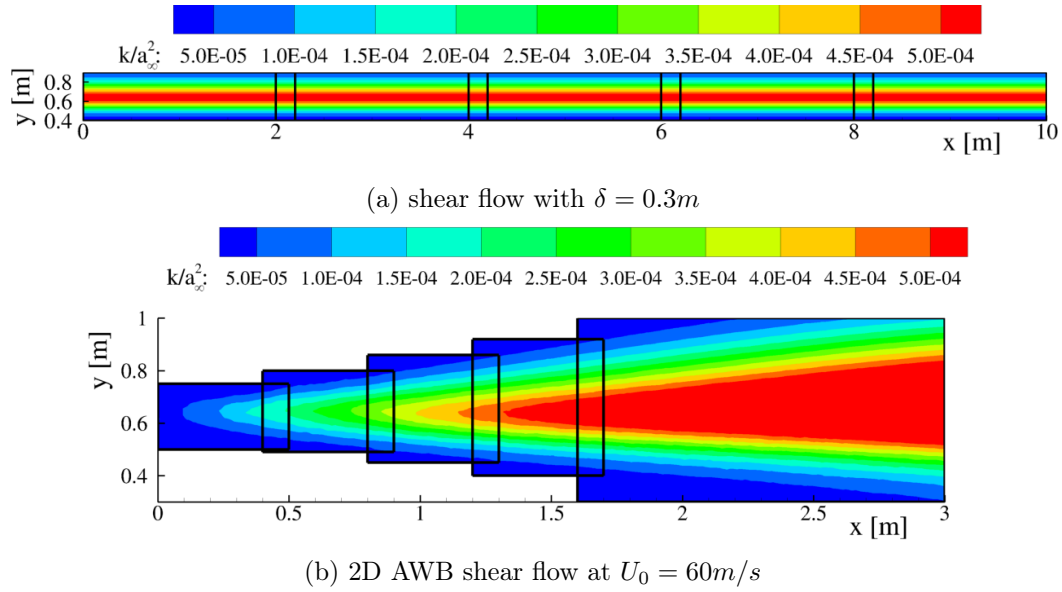


Figure 4.47: Structure of the patches with TKE contour.

#### 4.4.2 Characteristics of the turbulence part in the free shear layer

The reconstruction of the turbulence statistics by FRPM is mainly based on two parameters of the shear flow from the RANS simulation results. One is the turbulence kinetic energy  $k$ , as shown in Fig.4.47. The other is the integral length scale of the turbulence  $l_s$ , which are calculated from the turbulent kinetic energy and the specific dissipation rate ( $\omega$ ) of the shear flow.

Fig.4.48 shows the turbulent kinetic energy distribution at three cuts of the shear flow as well as the local velocity profile. Both parameters were normalized by the sound speed. The location  $x$  represents the distance from the nozzle exit. The first cut is extracted near the nozzle exit, where the turbulence intensity is relatively small. As the flow goes further, the turbulence well developed, so that a typical peak distribution is observed at cut  $x = 1.5m$  in the center figure. The flow parameters at this cut were also used to generate the constant thickness shear flow to study the corresponding turbulence effect. The last cut is extracted at  $x = 2.8m$ , which is close to the right boundary of the CAA domain. The TKE shows a wider distribution while its peak stays around  $y = 0.7m$ .

Taking the above TKE distributions as the target, the stochastic method FRPM reconstructed the turbulence statistics in the CAA computations. Whether the reconstructed distribution meets the original target is an important criterion for the quality of the stochastic model. It determines whether the scattering effect can be well realized in the simulations. In the following part, the reconstructed TKE will be shown as a comparison with the target one to show the effectiveness of the method and also its influence on the computation results.

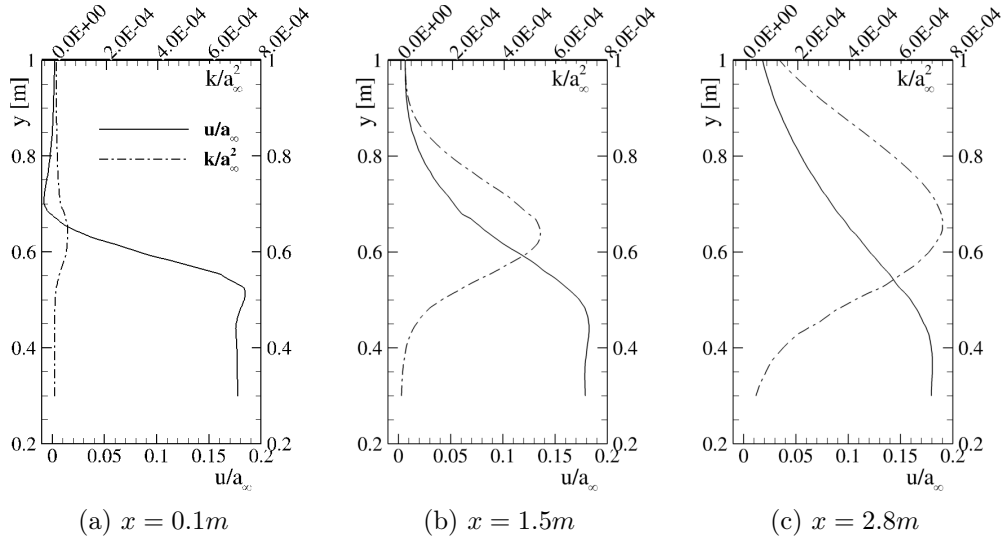


Figure 4.48: Turbulence kinetic energy distribution at  $U_0 = 60\text{m/s}$ .

#### 4.4.3 Sound propagation through the turbulent shear layer

Before presenting the CAA simulation results, the reconstructed turbulence kinetic energy is given as the distribution along vertical directions at the specified sections for both the turbulent shear flow with constant thickness and the AWB shear flow, as shown in Fig.4.49a. Since the TKE distribution does not vary in the flow direction in the constant thickness case, its TKE is plotted only at the center cut of the first patch (refer to Fig.4.47a) in Fig.4.49a, comparing with the original data from the CFD simulations. The TKE curves are given for the AWB turbulent shear flow at five sections in the flow direction, as indicated by the top figure in Fig.4.49. The reconstructed TKE (plotted by the dashed curves) illustrates a slightly smaller peak, which may result from the filter kernel applied in the current cases. The filter kernel can cause a wider energy distribution in the vertical direction as indicated by the dashed curves and a reduced peak value of the TKE. Generally, the TKE was well reconstructed, which illustrates the turbulent feature of the free shear layer.

Starting with the computations in the turbulent shear flow with constant thickness, the sound propagation characteristics at different radiation angles were examined. According to the previous study[R. H. Schlinker 1980], the sound wave will experience an omnidirectional refraction by the turbulence through the shear layer, which is quite different from the refraction observed in Sec.4.1. Fig.4.50 gives the temporal pressure field of the sound wave transmission through the constant thickness ( $\delta = 0.3\text{m}$ ) shear layer at source frequency  $5\text{kHz}$  with turbulence considered. Obviously, the regular refraction pattern is interrupted by the turbulence if compared with the similar case in Fig.4.7. The pressure amplitude outside the shear layer is enhanced in some area while reduced in other area. Such a phenomenon is also observed upstream below the shear layer, where the total reflection happens. In the study of the mean flow gradient, a shadow area was observed right above the shear layer when the total reflection happened. The amplitude of the pressure perturbation

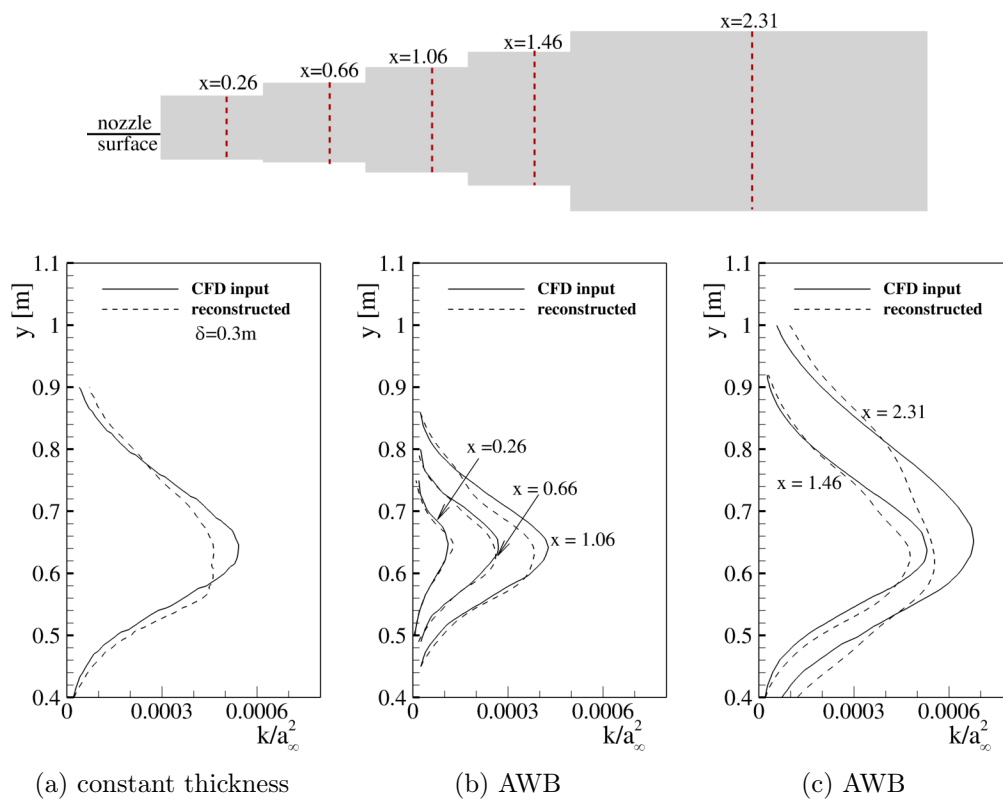


Figure 4.49: Reconstructed TKE of the turbulent shear layer at  $U_0 = 60\text{m/s}$ .

tion increases in this area as the turbulence is included, indicating the scattering of the sound wave direction by the turbulence. The pattern downstream below the shear layer does not vary too much from the distribution observed in the study of the mean flow gradient effect. This indicates a weak reflection effect due to the turbulence. It should be mentioned that the scattering induced pattern varies with time, which means that the high and low amplitude area is not fixed at certain positions but closely depends on the intersection between sound waves and the turbulence in the shear layer. If one checks the time history of the pressure fluctuation at the single point, it shows a clear stochastic feature.

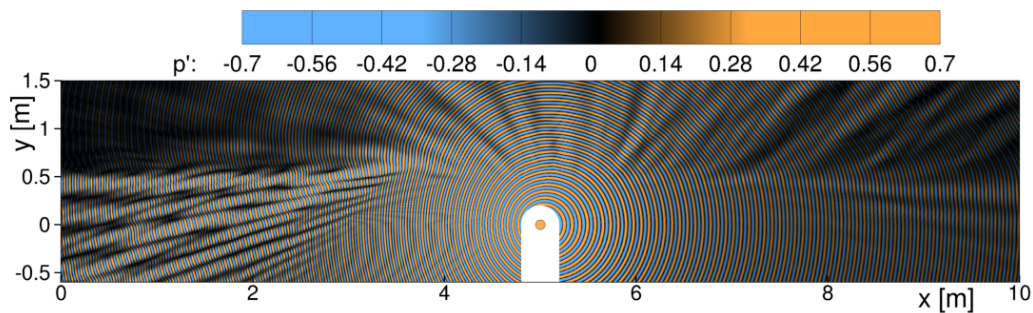


Figure 4.50: Instantaneous pressure field of the sound transmission through the turbulent shear layer with constant thickness  $\delta = 0.3m$  ( $f = 5kHz$ ,  $U_0 = 60m/s$ ).

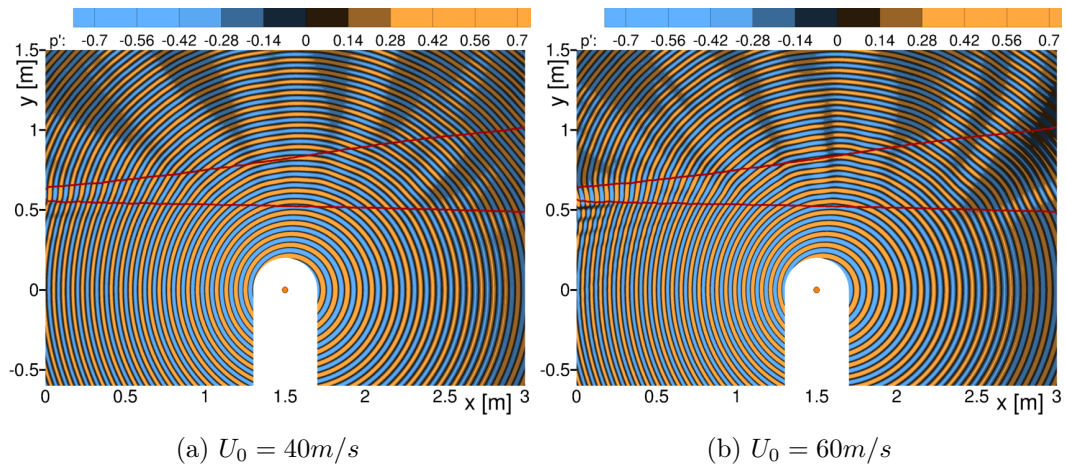


Figure 4.51: Instantaneous pressure perturbation field of the sound transmission through the AWB turbulent shear flow ( $f = 5kHz$ ).

Fig.4.51 plots the instantaneous perturbation field for the AWB turbulent shear flow. The shear layer shape is given by the red curves. The contours show a very similar scattering pattern as observed in the constant thickness shear flow. The spreading shape of the shear layer seems not to bring much variation to the scattering effect. It will be further quantitatively evaluated in the next section.

#### 4.4.4 Alteration of the sound wave characteristics through the turbulent shear layer

The most apparent feature of the turbulent shear layer effect is the alteration in the frequency band of the original sound wave. To clearly illustrate this feature, the narrow band spectra are firstly given in Fig.4.52 for the microphones in the uniform flow (orange curve), the averaged shear flow in AWB (blue curve) and the turbulent shear flow in AWB (black curve), respectively. Three microphone locations are chosen to show the variation with the measurement angle, as shown in Fig.4.52a. The SPL was normalized by the magnitude of the tone frequency at  $\theta_M = 90^\circ$  in the uniform flow. In order to show the amplitude variation of the sound wave through different flow fields, the magnitudes of the tone frequency in different flow fields are marked in the corresponding color by the horizontal lines. Obviously, the turbulent shear flow results in a severe amplitude reduction at the tone frequency as well as an apparent spectral broadening. The amplitude variation of the sound wave by the mean flow gradient can be observed as well.

Next, the narrow band spectra are given for the microphones outside the shear layer as sound waves transmit through different type of the turbulent shear flow. These spectra can indicate the variation of the turbulent effects with the shear layer thickness, the source frequency and the flow speeds. Fig.4.53 plots the narrow band spectra at three locations along the microphone line  $y_M = 1.2m$  when the sound wave propagates through the turbulent shear layer with constant thickness. The corresponding simulations have a 1.25s real time duration. Obviously, the computations captured the spectral broadening effect by the turbulence. This effect becomes severer as the source frequency increases. It is coincident with the phenomenon observed in Candel's work [S. Candel 1975]. Moreover, it can be noticed that the severity of the spectral broadening varies with the measurement angle. As the measurement angle deviates from  $90^\circ$ , the spectral broadening becomes more obvious. At upstream and downstream locations, the SPL reduction at the tone frequency is much bigger than that at the location right above the source. However, the apparent sidelobes observed in Candel's experimental work (refer to Fig.1.2b) are not very clearly illustrated in the figure. This may result from the resolution of the spectra analysis.

Fig.4.54 shows the spectra along the  $y_M = 1.2$  line outside the shear layer for the sound propagation through the AWB turbulent shear flow at  $U_0 = 60m/s$ . The shown spectra are normalized in such a way that the tone amplitude is constant. As above, three locations were chosen to investigate the turbulent effect variation with the measurement angle, as indicated in Fig.4.54a. Comparing with the spectra obtained in the shear flow with constant thickness, the sound wave in the AWB shear flow experiences a weaker spectral broadening as it propagates upstream. This results from the fact that the local traveling distance of the sound wave through the AWB shear flow is much smaller than that in the constant thickness shear flow. Downstream the spectral broadening is more obvious in the AWB shear flow since the wave travels a longer distance in the turbulent shear layer. The amplitude at

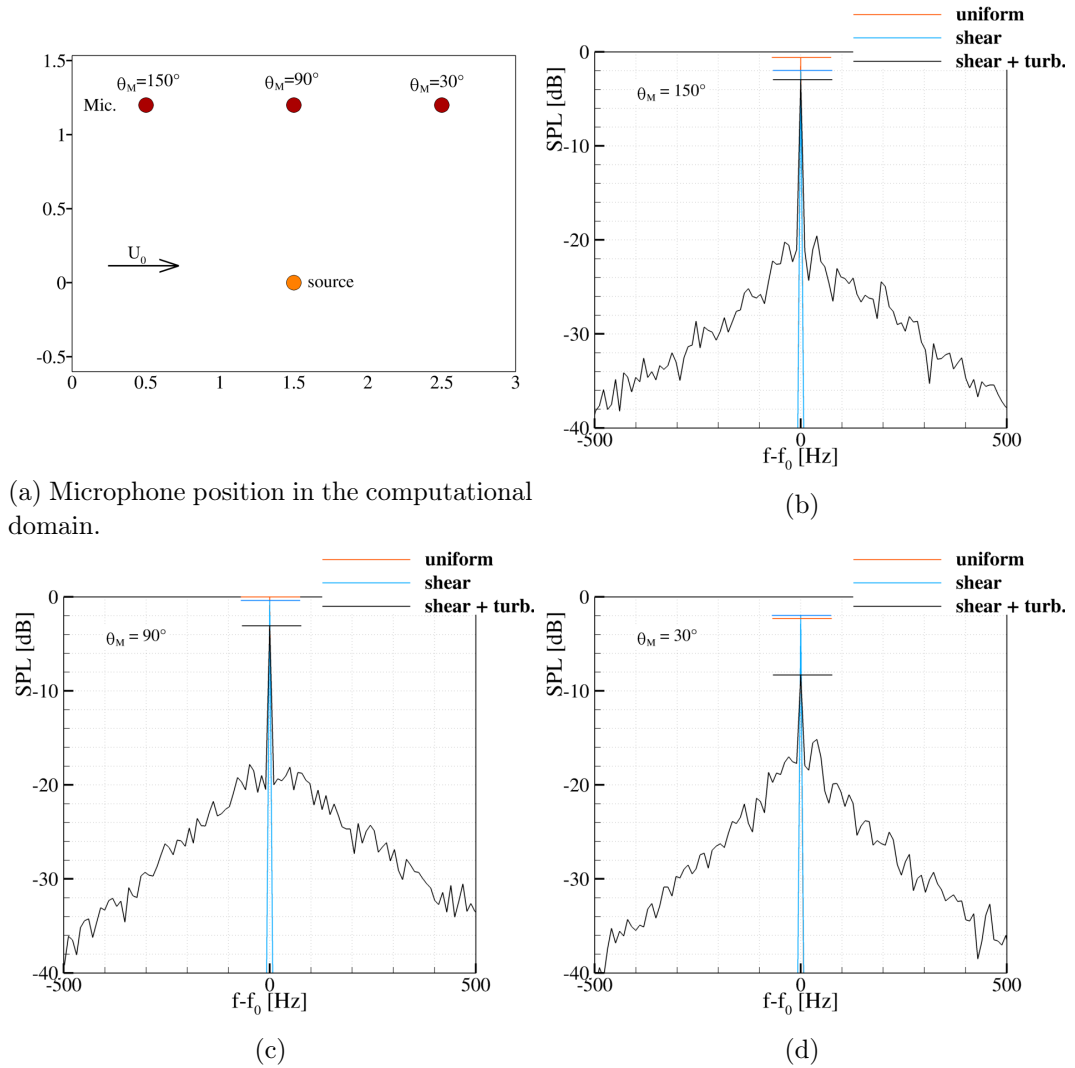


Figure 4.52: Spectra comparison in the uniform flow, averaged shear flow (in AWB) and turbulent shear flow (in AWB) ( $U_0 = 60m/s, f_0 = 10kHz, \Delta f = 10Hz$ ).

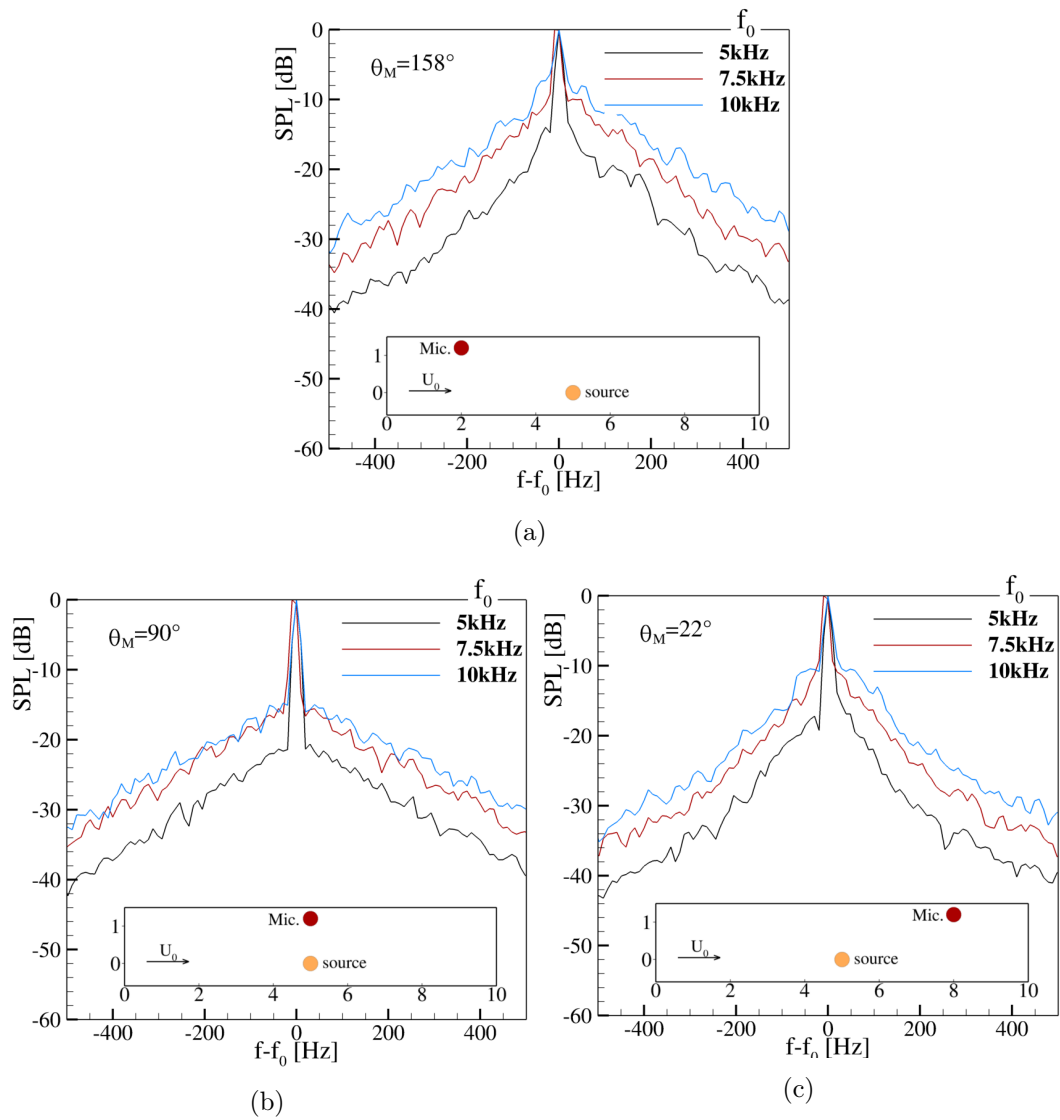


Figure 4.53: CAA simulated spectra in the turbulent shear flow with constant thickness ( $U_0 = 60\text{m/s}$ ,  $\Delta f = 10\text{Hz}$ ).

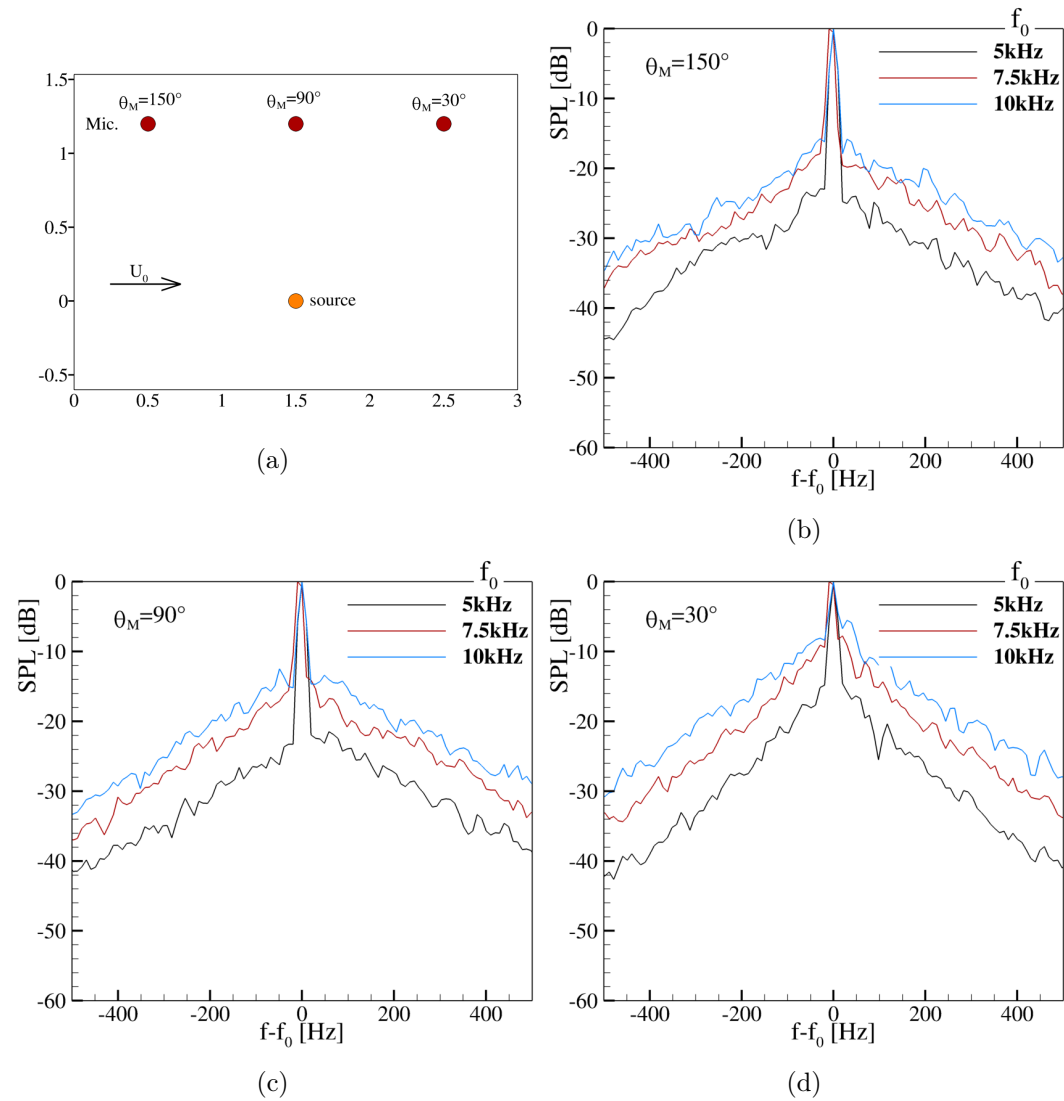


Figure 4.54: CAA simulated spectra in the AWB turbulent shear flow ( $U_0 = 60\text{m/s}$ ,  $\Delta f = 10\text{Hz}$ ).

the tone frequency is almost smoothed out by the scattering effect at  $10kHz$  at the downstream location. Again, the sidelobes due to the 'haystacking' effect were not well captured in the simulations.

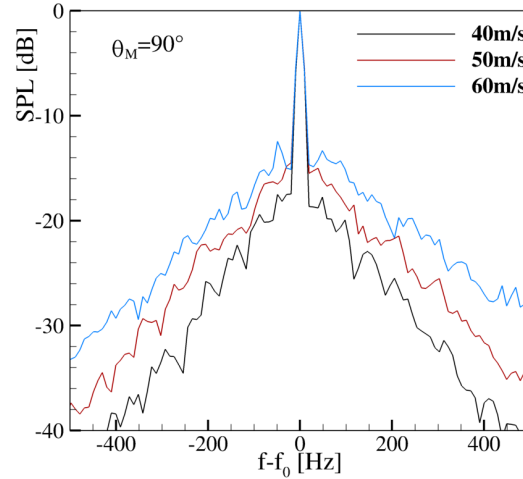


Figure 4.55: CAA simulated spectra in the AWB turbulent shear flow at  $f = 10kHz$  ( $\Delta f = 10Hz$ ).

To illustrate the variation of the spectral broadening effect with the flow speed, the spectra at the tone frequency  $10kHz$  were plotted for the AWB turbulent shear flow with various flow speeds, shown in Fig.4.55. The observer's position was chosen right above the source. As the flow speed increases, an obvious wider spectrum was obtained with two small observable sidelobes near the tone frequency.

In order to analyze the amplitude reduction at the tone frequency outside the turbulent shear flow, the SPL value at the tone frequency was calculated from the corresponding spectra in the uniform flow, the time-averaged shear flow, and the turbulent shear flow. The SPL value at the single observer's position was obtained by integrating the area around the tone frequency in the length  $\Delta f$  from the spectrum. Applying the process to several observer's positions along the line  $y_M = 1.2m$ , the SPL curve similar to that in the mean flow gradient study can be obtained. Fig.4.56 gives the curves in the shear flow with constant shear layer thickness, comparing with that in the uniform flow. The horizontal axis represents the observer's position in the computation domain, in which  $x = 5m$  is the position right above the source point. Different from the sound propagation in the time-averaged shear flow, the sound propagation through the turbulent shear layer shows an obvious relevance with the source frequency. The maximum amplitude reduction at the observer's position increases from  $1.5dB$  at  $5kHz$  to  $5dB$  at  $10kHz$ . A common feature noticed in the figures is the bigger deviation between the curves for the time-averaged shear flow and the turbulent shear flow in the downstream locations. This may be caused by the additional convective effects from the turbulence part.

Similarly, the SPL curves were plotted for the sound propagation in the AWB turbulent shear flow at  $U_0 = 60m/s$  in Fig.4.57. Comparing with the previous con-

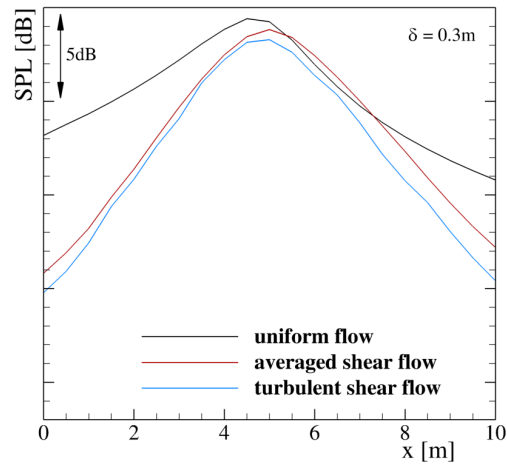
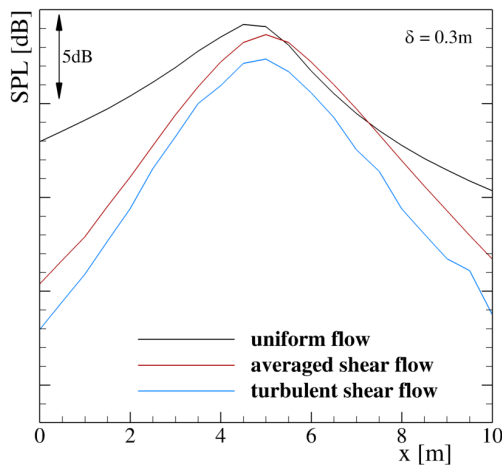
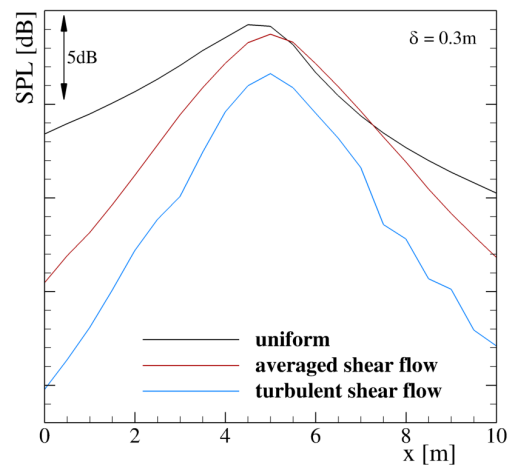
(a)  $f = 5\text{ kHz}$ (b)  $f = 7.5\text{ kHz}$ (c)  $f = 10\text{ kHz}$ 

Figure 4.56: The SPL value along the microphone line  $y_M = 1.2\text{ m}$  at the tone frequency in the shear flow with constant thickness ( $U_0 = 60\text{ m/s}$ ).

stant thickness shear flow, the turbulence induced deviation decreases to a smaller value in the upstream location. This can be attributed to the thin shear layer thickness upstream. Correspondingly, the deviation in the downstream locations goes up significantly, resulting from the thicker shear layer in this part. The turbulence effect could cause an amplitude reduction up to around  $7dB$  at  $10kHz$ . In the mean time, one may notice that the curve in the turbulent shear flow overlaps to that in the time-averaged shear flow in some areas at  $7.5kHz$ . This could be caused by the cancellation between the scattering effect and the turbulence convective effect. Fig.4.58 plots the identical distribution in the shear flow at  $U_0 = 40m/s$ , indicating a smaller reduction in the amplitude at the tone frequency downstream as the flow speeds decreases.

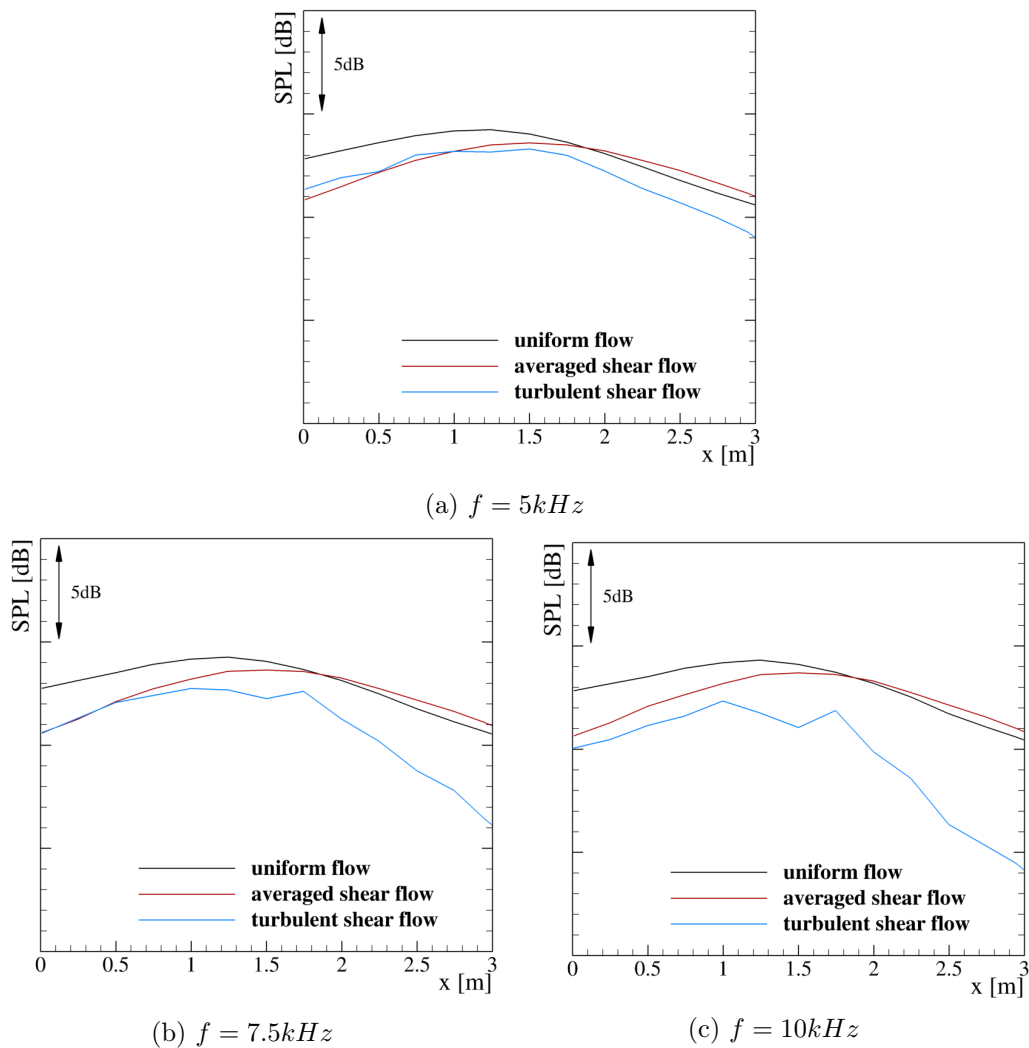


Figure 4.57: The SPL value along the microphone line  $y_M = 1.2m$  at the tone frequency in the AWB shear flow ( $U_0 = 60m/s$ ).

So far the scattering effect by the free shear layer was investigated, with the

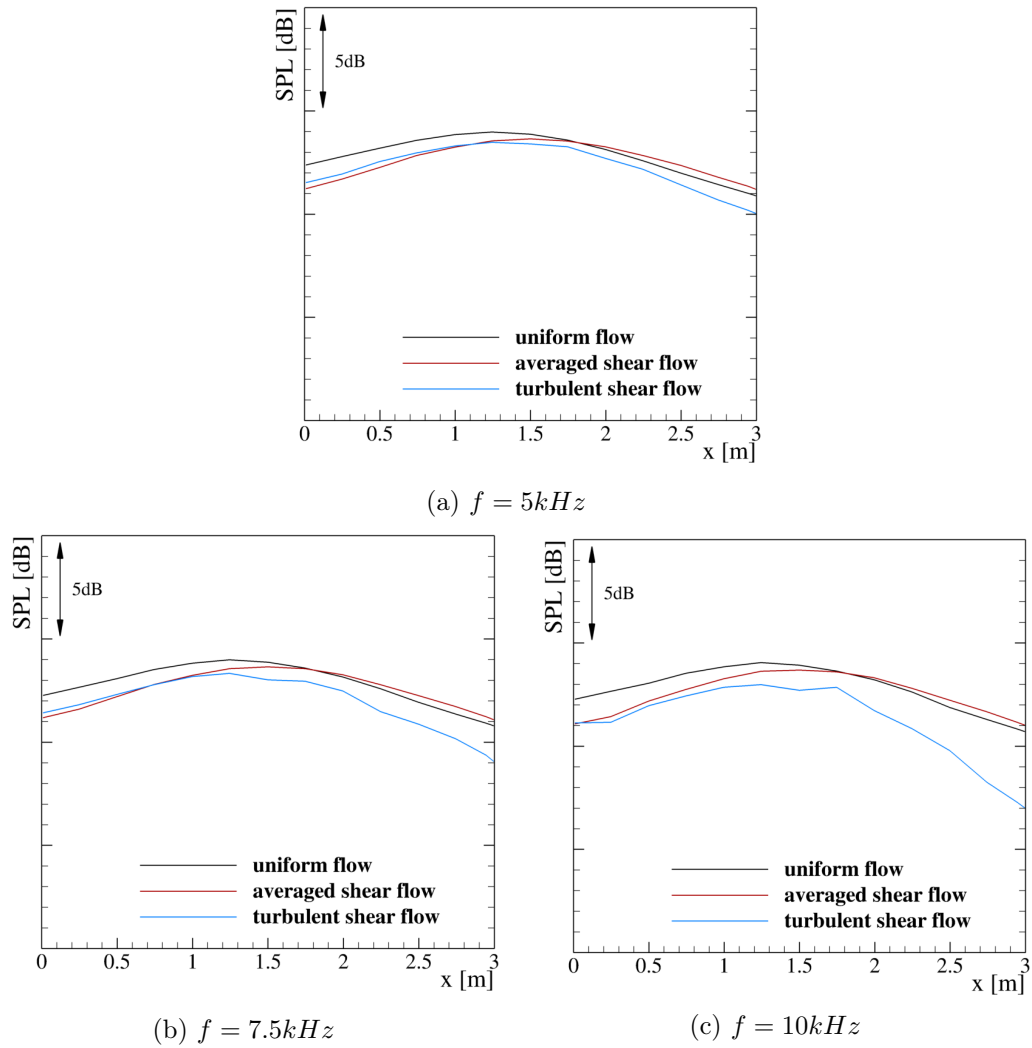


Figure 4.58: The SPL value along the microphone line  $y_M = 1.2\text{ m}$  at the tone frequency in the AWB shear flow ( $U_0 = 40\text{ m/s}$ ).

analysis of its inducing deviation from the situation when only the mean flow gradient was considered. The spectral analysis shows the coincident phenomena with that in Candel's experiments. However, the sidelobes in the spectra due to the scattering effect was not well established, which may be relevant to the frequency band resolution in the analysis.

#### 4.4.5 Role of turbulent pressure fluctuation in the scattering effects

In the previous study of the scattering effects, the pressure fluctuation of the turbulence was neglected. In this part, the role of the pressure fluctuations in the turbulence will be examined. The turbulent pressure fluctuation ( $p_t$ ) was roughly estimated on the basis of a local linearized Bernoulli equation as  $p_t \simeq -\rho \mathbf{v}_0 \cdot \mathbf{v}_t$ . To keep the consistency of other parameters with the previous study, the identical computational setup was adopted as the simulations of the 2D study in the AWB shear flow with  $U_0 = 60m/s$  with the source frequency  $f = 10kHz$ . Besides, the same parameters were utilized in the spectra analysis.

Fig.4.59 gives the spectrum at three specified measurement locations as in the previous investigations. The magnitude was normalized by the SPL at  $\theta_M = 90^\circ$  in the original simulation when  $p_t$  was not considered. Apparently, the participation of the turbulent pressure fluctuations do not bring a significant deviation into the spectra distribution at the considered flow speed and the source frequency. The spectrum upstream show a slightly wider distribution due to the broadening effects by the turbulence; the reverse effect is seen downstream. The effect of the turbulence related pressure perturbation therefore can result in a tonal amplitude variation less than  $1dB$ . If the observer stands right above the source outside the shear layer ( $\theta_M = 90^\circ$ ), a very similar spectrum was generated without obvious tonal amplitude reduction.

### 4.5 Sound propagation through turbulent shear layers (3D)

As the last part of the numerical investigations of the shear layer effects, the sound propagation through the 3D turbulent shear layer was simulated and analysed. The 3D shear flow of the AWB wind tunnel at  $U_0 = 40m/s$  and  $U_0 = 60m/s$  were chosen as the background flow field in this part.

#### 4.5.1 Computational setup

The CAA domain of the computations was kept the same as that in the study of the 3D mean flow gradient effects (refer to Sec.4.3.1). It is a  $2m \times 1.2m \times 1.2m$  domain with the source surrounded by a quarter cylinder. The patch area was limited to include only the upper shear layer in the wind tunnel since the computational effort increases significantly in 3D as the turbulence was considered. Five overlapped

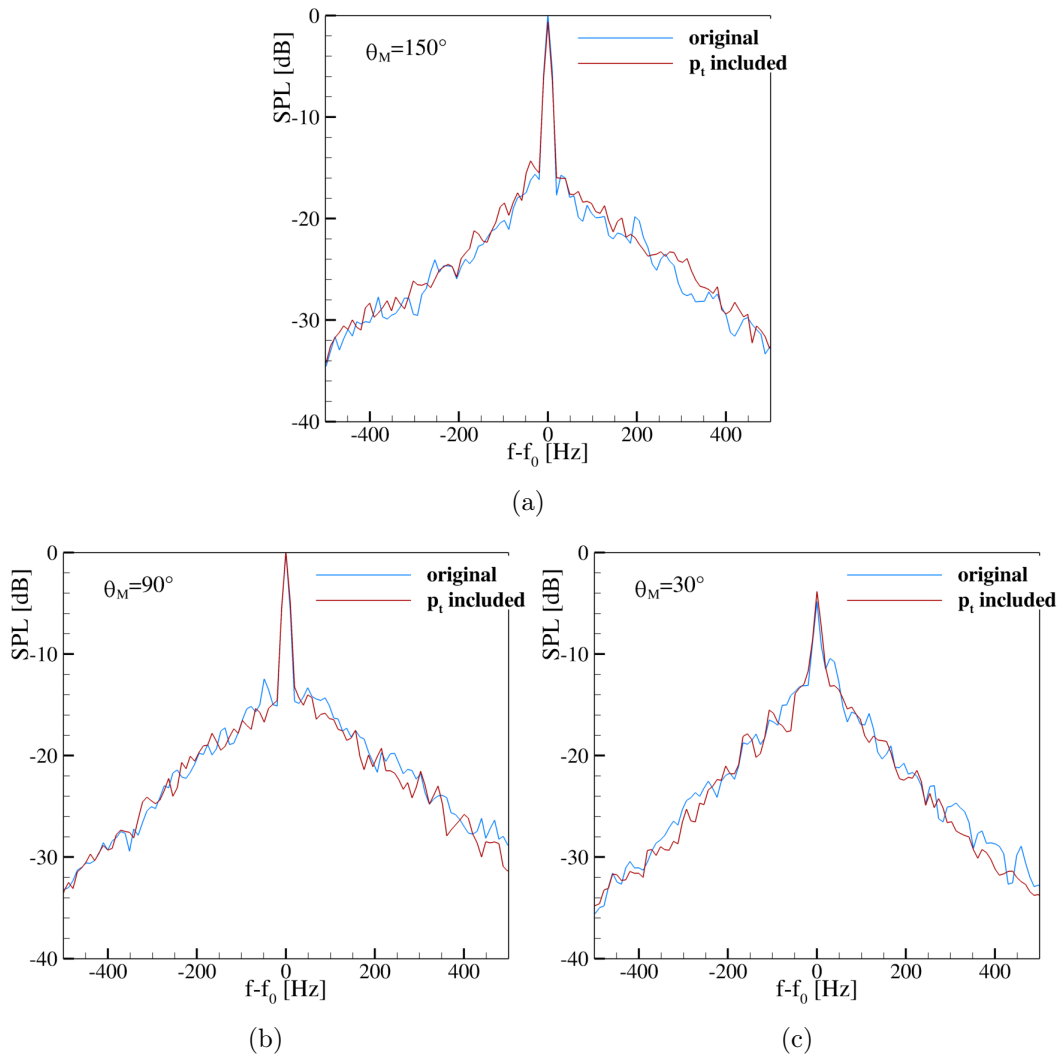


Figure 4.59: CAA simulated spectra in the AWB turbulent shear flow ( $U_0 = 60m/s$ ,  $\Delta f = 10Hz$ ).

patches were generated to store the turbulence statistics. The overall length of the patches is  $2m$  long in the flow direction and  $0.4m$  long in the span-wise direction. Their lengths in the vertical direction vary with the shape of the shear layer, similar to that in the 2D applications. Fig.4.60 gives the location of the patches in the wind tunnel test section and the turbulence kinetic energy distribution at  $U_0 = 40m/s$ .

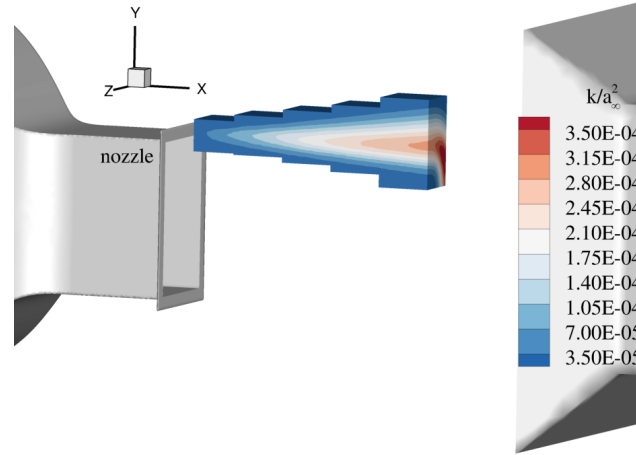


Figure 4.60: Location of the patches with TKE contour at  $U_0 = 40m/s$ .

Fig.4.61 plots the turbulent kinetic energy at three cuts along the flow direction at  $U_0 = 40m/s$ . The rectangular shape of the shear layer is also illustrated in the TKE distribution, with part of the shear layer corner included. A high TKE area is found downstream near the intersection corner of the shear layer, which might exert strong effects on the sound wave. In this area, the mixture of the flow at the wake of the corner generates more turbulence. The TKE distribution at  $U_0 = 60m/s$  shows a similar feature as that at  $U_0 = 40m/s$ . Its contour will not be repeated here.

The identical point source at  $10kHz$  as in the 3D mean flow gradient study at the frequency  $10kHz$  was chosen in this part. Three microphone circles with radius  $r = 1.2m$  were placed outside the shear layer to monitor the variation of the signals by the turbulent shear layer. By this arrangement, the difference is easily observed between the measurement data experiencing the scattering effects (through the upper shear layer) and the data without experiencing the scattering effects (through the side shear layer). The time length of the collected data at the microphones achieves  $0.625s$  real time duration. Moreover, another phenomenon needs to be mentioned is the instability in the simulations. The instability problem was found on the  $z = 0m$  plane, which was set to be a symmetrical plane. This problem was solved by increasing the local damping on the symmetrical plane. A detailed description of the instability and its solution can be found in the Appendix C.

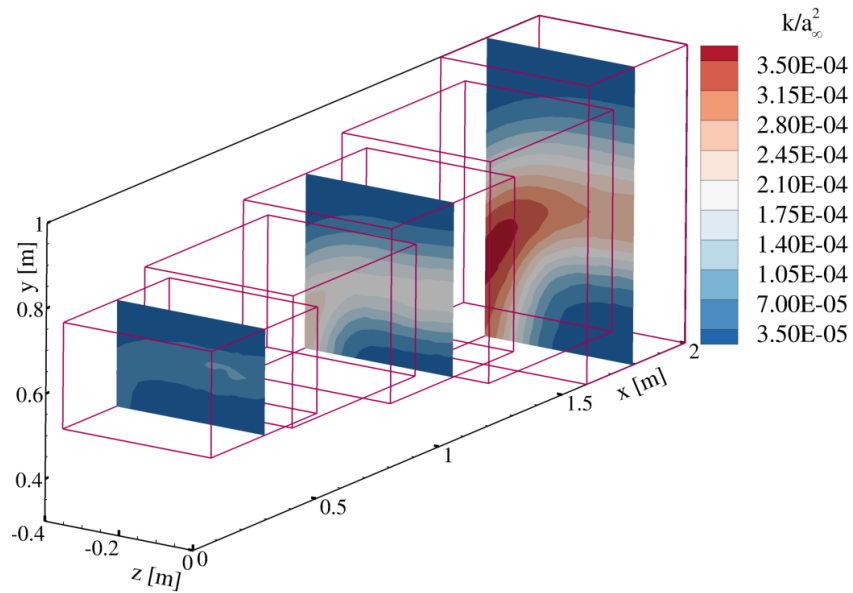


Figure 4.61: TKE distribution in the flow direction at  $U_0 = 40\text{m/s}$ .

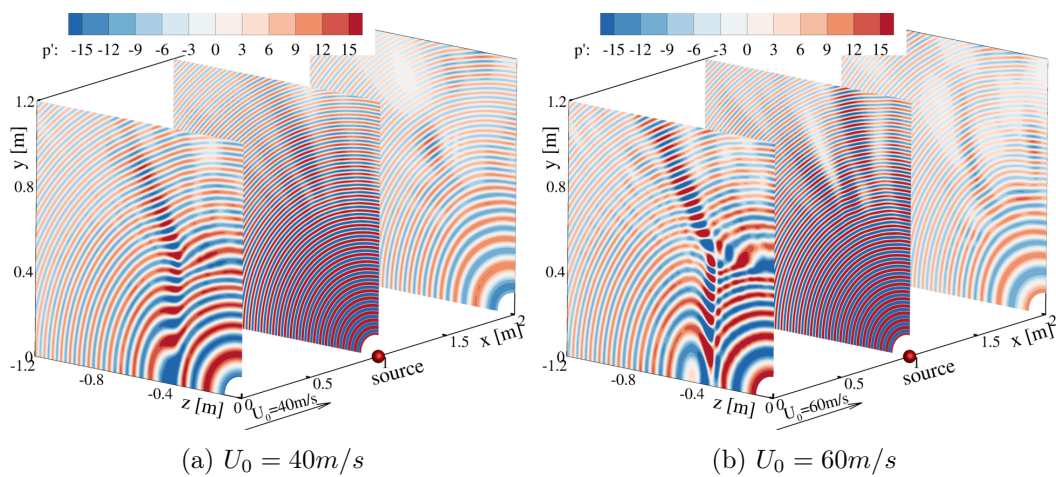


Figure 4.62: Instantaneous pressure field through the 3D turbulent shear flow ( $f_0 = 10\text{kHz}$ ).

### 4.5.2 Sound propagation through the turbulent shear layer

In order to give a straightforward view of the 3D sound transmission through the turbulent shear layer, the instantaneous pressure field is given at three sections perpendicular to the flow direction at two flow speeds, as shown in Fig.4.62. The distorted wavefront pattern in the first section ( $x = 0m$ ) in both figures results from the mean flow gradient effect discussed in the previous section, which becomes more obvious with the flow speed. The turbulence effect does not show a dominant effect at this section since the TKE in this part is in a low level. But its influence becomes stronger with the flow speed. At the middle section ( $x = 1.0m$ ), the scattering effects become more obvious, especially in the high speed turbulent flow. The last sections ( $x = 2.0m$ ) illustrate the strongest scattering effect, where the original sound wave pattern was completely destroyed and scattered to other directions. This is coincident with the phenomena in the 2D study that the scattering is more severe as the shear layer thickness (and correspondingly the TKE) or the flow speed increases.

### 4.5.3 Alteration of the sound wave characteristics through the turbulent shear layer

As another effective tool to study the feature of the scattering effects, the spectra at several microphone positions are plotted, as shown in Fig.4.63 and Fig.4.64. Three microphone circles were positioned outside the shear layer to collect the data. The circles center at a specified position on the  $x$ -axis, indicated by  $x_M$ . Each microphone on the circle is defined by the angle  $\phi_M$ , as plotted in Fig.4.63a and Fig.4.64a. In the analysis, three microphones were chosen to observe the scattering effect:  $\phi_M = 90^\circ$  represents the reference point where the sound wave does not experience the scattering effect, and  $\phi_M = 0^\circ, 30^\circ$  give the indication when the sound wave goes through the turbulent shear layer but at different angles. The magnitude of the spectra was normalized by the amplitude at the tone frequency itself, such that the peak of the spectrum locates exactly at  $0dB$ . It is convenient for observation of analysis of the spectral broadening effect.

Fig.4.63 shows the spectra in the turbulent shear flow at  $U_0 = 40m/s$ . The sound wave experiences a weak scattering effect upstream ( $x_M = 0.2m$ ) due to the low intensity of the turbulence and the thin thickness of the shear layer. The scattering effects become stronger as the sound wave transmits through a thicker shear layer with higher turbulence intensity ( $x_M = 1.0m, 1.8m$ ). The microphone at  $\phi_M = 30^\circ$  was firstly chosen to examine whether the scattering effects will be more obvious around this area due to the higher turbulent kinetic energy (see Fig.4.61). However, the spectrum does not support this hypothesis as expected at upstream location. A possible reason for such phenomena might be the mean flow gradient effects. The tonal amplitude reduction caused by the upper turbulent shear layer may be compensated by the refracted wave from the side shear layer (refer to Sec.4.3). Fig.4.64 illustrates the spectra in the turbulent shear flow at  $U_0 = 60m/s$ . Wider spectra

are observed at each section than those at  $U_0 = 40\text{m/s}$ , especially at downstream location ( $x_M = 1.8\text{m}$ ). This indicates a stronger scattering effect at higher flow speed and severe amplitude reduction at the tone frequency, which can be clearly observed in the following SPL analysis at the tone frequency.

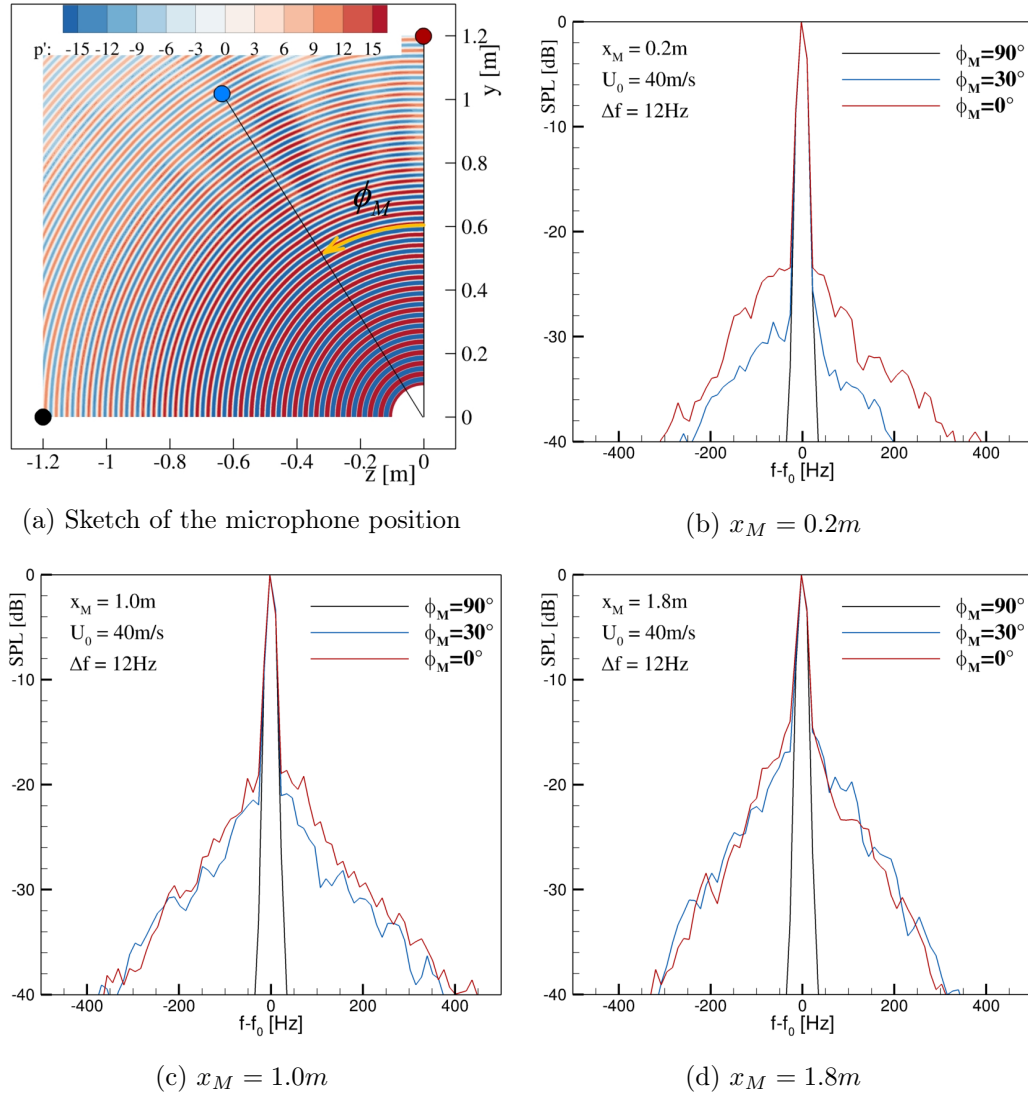


Figure 4.63: CAA simulated spectra in the AWB turbulent shear flow ( $U_0 = 40\text{m/s}$ ,  $\Delta f = 12\text{Hz}$ ).

The above interpretation can also be supported by the SPL at tonal frequency along the microphone circles, as shown in Fig.4.65. These curves were obtained by the same way as in the 2D analysis (refer to Sec.4.4.4). The SPL value at the single observer's position was obtained by integrating the area around the tone frequency in the length  $\Delta f$  from the spectrum. The solid curves represent the data obtained in the averaged shear flow (without turbulence). The dash dot curves indicate the

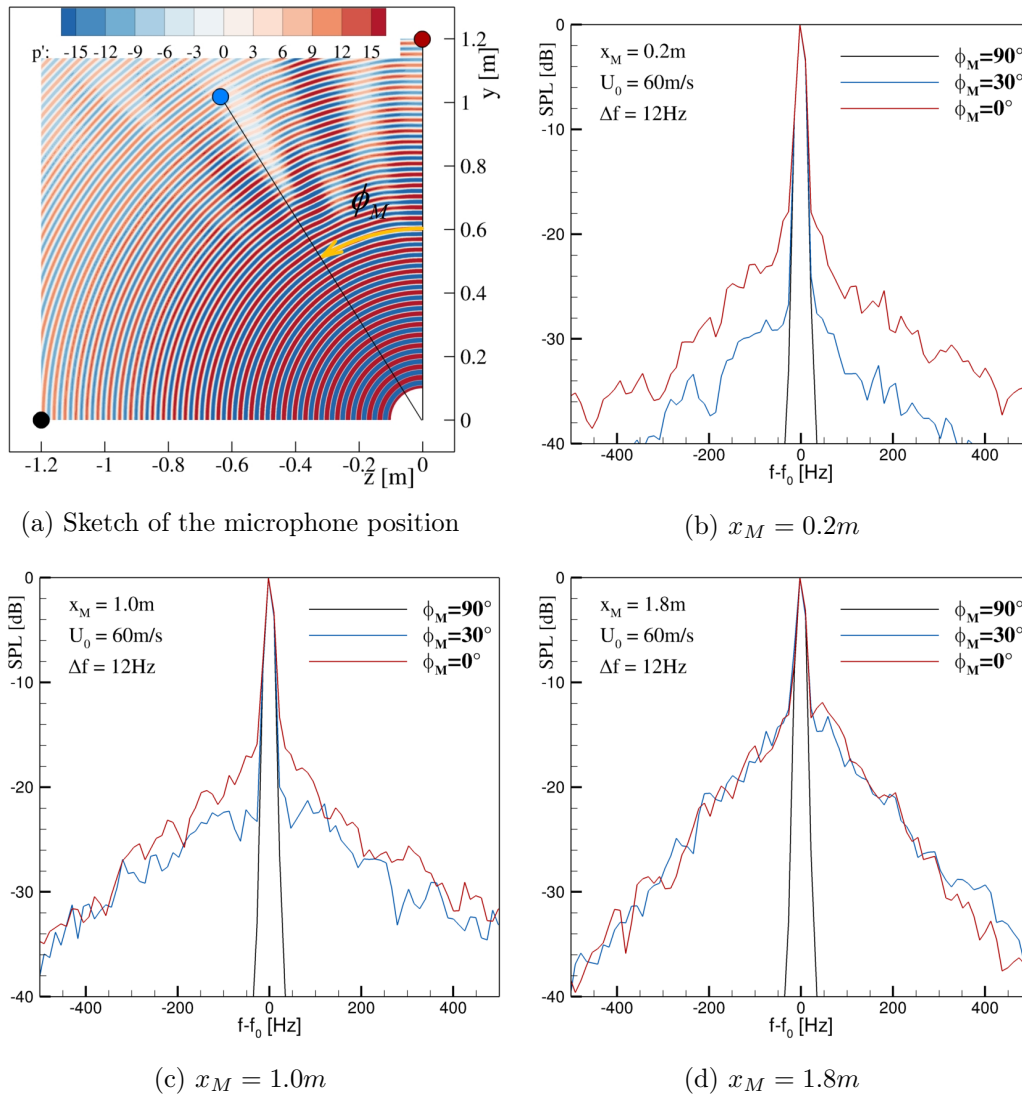


Figure 4.64: CAA simulated spectra in the AWB turbulent shear flow ( $U_0 = 60m/s$ ,  $\Delta f = 12Hz$ ).

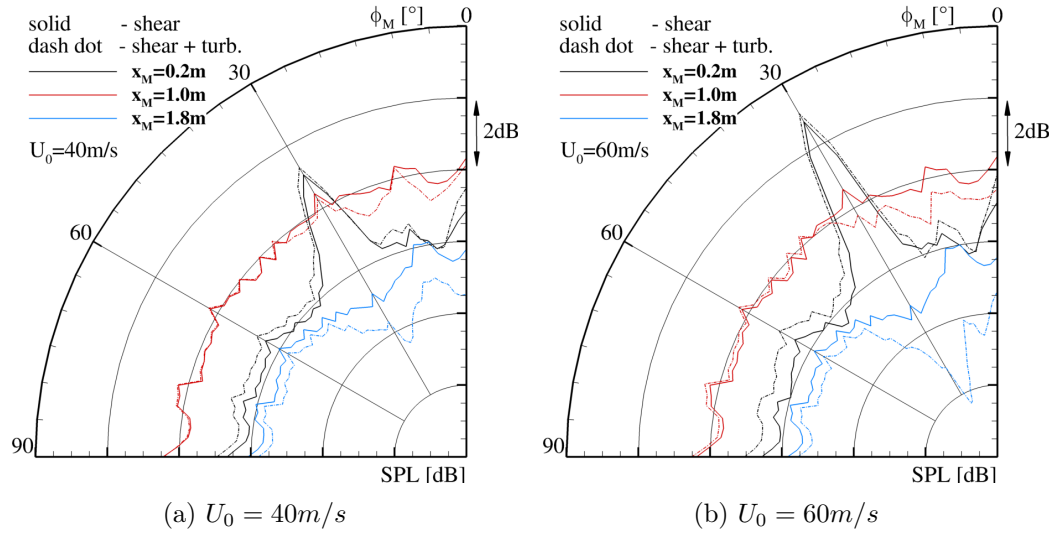


Figure 4.65: The SPL value along the microphone circle at the tone frequency ( $f_0 = 10kHz$ ) in the turbulent AWB shear flow.

data obtained in the turbulent shear flow. As the microphones were chosen in the same plane with the source ( $x_m = 1.0m$ , red curves), the receiving signals through the turbulent shear layer ( $\phi_M = 0 \sim 30^\circ$ ) illustrates a scattering induced amplitude reduction at the tone frequency. This reduction increases with the flow speed. As the upstream microphones are examined ( $x_M = 0.2m$ ), an obvious amplitude peak was noticed at  $\phi_M = 30^\circ$ , resulting from the aforementioned 'focussing' effect of the rectangular shear layer. This effect becomes more obvious as the flow speed goes up. The turbulent scattering induces only slightly amplitude variation at this section. At downstream location ( $x_m = 1.8m$ ), there is an amplitude valley around  $\phi_M = 30^\circ$ , caused by the aforementioned 'spreading' effect. In the turbulent shear flow, a deeper valley in this area is noticed. This might be related to the stronger scattering by the thick, high intensity turbulent flow around this part.

As the last point, the SPL on the symmetrical plane ( $z = 0m$ ) in 3D is compared with the SPL in the 2D simulation at the tone frequency. In the current 3D study, the flow condition on the symmetrical plane ( $z = 0m$ ) is identical to the flow condition in the previous 2D study. The comparison of the SPL at the tone frequency on this plane would be helpful to identify the deviation between the 2D and 3D simulations. Fig.4.66 plots the data at two flow speeds. The coordinates ( $x_M$ ) of the 3D data are modified according to the distance from the source point to fit the 2D data. The SPL of the 3D data is adjusted to the same range as the 2D data, since the original source magnitudes are different in the 2D and 3D simulations. The data illustrates quite similar trend between 2D and 3D cases. The amplitude decreases as the flow goes downstream. The most obvious deviation between 2D and 3D cases is the amplitude variation with the flow speed. In the 2D case, the amplitude shows an apparent amplitude reduction as the flow speed increases. In 3D case, the amplitude varies slightly with the flow speed at the available three locations. The data on more

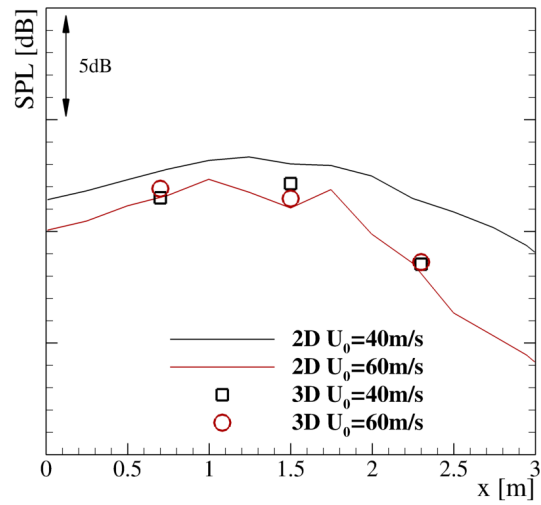


Figure 4.66: Comparison of the SPL at the tone frequency between 2D and 3D simulations.

microphone positions are needed to identify the 3D variation trend with the flow speed.

# Summary, conclusions and outlook

---

## 5.1 Summary

A numerical investigation was conducted to study the free shear layer effects in the open-jet wind tunnel. The research was performed with a hybrid CAA method, which includes the simulation of the shear flow (done by TAU), the simulation of the sound propagation (done by PIANO) and the realization of the turbulence (reproduced by FRPM).

For simulations focused on the investigation of the mean flow gradient effects, a harmonic source was employed at  $1kHz$ ,  $5kHz$  and  $10kHz$  to observe its frequency relevance. Free stream velocity in the wind tunnel varied from  $40m/s$  to  $60m/s$ . Three types of the shear flow were chosen in 2D, i.e. the constant thickness shear layers with linear velocity profile, the wind tunnel shear layer with spreading shape and the curved shear flow around a high lift airfoil. Sound propagation direction and amplitude changes across the shear layer were extracted from the computational results, which illustrated a severe alteration in both the propagation angle and the source directivity as comparing with those in the uniform flow. These numerical results were compared with the state-of-the-art correction method (Amiet's approach) for the mean flow gradient effects.

Good agreement was obtained between the correction method and the numerical results over the considered shear layer thickness, flow speed, source frequency, measurement angle range and the shear flow type. Such a consistency indicated that the angle and amplitude changes induced by the shear layer refraction are independent of the source frequency, shear layer thickness as well as the shear layer divergence. It should be mentioned that the decrease of the accuracy of the correction method in the curved shear flow can be supplemented by adjusting the correction model based on the flow curvature. Additional -and quite considerable- reflection effects at the nozzle rim were found and the computation of the harmonic source was confirmed by using additionally a pressure pulse source. The alteration in the receiving pressure amplitude at the measurement point showed a maximum of  $5dB$ .

A planar shear layer and a rectangularly shaped shear layer (formed by the nozzle geometry in the AWB) were applied to investigate the 3D sound wave propagation through the shear layer. Both the angle correction and the amplitude correction show a brilliant performance in the planar shear layer correction. Their accuracy showed a degenerated trend as the receiver located around the corner area in the AWB shear flow. In the AWB shear flow, a 'focusing' and 'spreading' effect due to the shear layer shape was found and analyzed. The resulting 'dangerous area' was

identified for source frequencies  $1kHz$  and  $10kHz$  by comparing with the results in the planar shear flow. The performance of the correction method was examined for these cases as well.

For the simulations focused on the investigation of the turbulence effects, the same harmonic source was applied with the frequency varying from  $5kHz$  to  $10kHz$  in 2D. A constant thickness ( $\delta = 0.3m$ ) shear flow and the AWB shear flow were adopted for the simulations. The reduction of the tone amplitude and the spectral broadening were observed. These features were found to be stronger at a higher source frequency or a higher flow speed. A stronger scattering effect was also observed at downstream locations in the AWB shear flow, while the source needs to pass through a thicker shear layer. The similar phenomena were noticed in the 3D sound propagation through the turbulent shear layer as well. The contribution of the turbulent pressure fluctuation was analyzed in 2D to figure out its role in the scattering effects. In this context it is important to note, that the turbulence, considered for the scattering in 2D was not turbulence from (unphysical) 2D vortex dynamics, but equivalent to respective 2D component of a 3D turbulence realization.

In the primary study of the sound propagation through the 3D turbulent shear layer, the AWB turbulent shear flow ( $U_0 = 40m/s, 60m/s$ ) was utilized to study the 3D scattering effects. The spectral broadening effect was realized and analyzed. The variation of the effect with the flow speed and the shear layer thickness was observed and analyzed. The reduction of the sound wave amplitude outside the turbulent shear layer was investigated and compared with that in the averaged shear flow.

## 5.2 Conclusions

Based on the numerical study of the shear layer effects in both 2D and 3D sound propagations, the following conclusions can be drawn for the open-jet wind tunnel shear layer effects.

Through the 2D time averaged shear flow, the alteration of the sound wave direction and amplitude due to the refraction of the shear layer is of only slight relevance with the shear layer thickness, divergence and the source frequency. The induced deviation is less than  $0.5dB$ . The main affected region is around the total reflection area, located at the upstream position at the considered flow velocities. Over the considered range of the measurement angle and the flow velocity, Amiet's approach can correct the deviations due to the mean flow gradient effects with a high accuracy. This high performance is weakened in the applications in the curved shear flow, but can be supplemented by an adjustment of the correction model according to the flow curvature. Such an adjustment can help to avoid a maximum of  $0.5dB$  error in the considered angle range. In the similar study but with the nozzle geometry included, the nozzle rim was proved to reflect the original sound waves to produce an obvious interaction pattern around the measurement area. Such a phenomenon should be seriously treated in the experiments.

For the 3D time averaged shear flow, the alteration of the sound wave direction and amplitude are closely related to the shear layer shape. Different from the regular refraction of the sound wave by the planar shear layer, sound waves passing through the rectangularly shaped shear layer (the AWB shear flow) may experience a 'corner' effect. This results in unreliable measurement results in certain areas ('dangerous area') and difficulties in the correction of the shear layer effects. This area is formed by the coupling of refractive sound waves from two intersected shear layers. The direction and amplitude alteration of the 3D sound wave can be well predicted by Amiet's approach through the planar shear layer. Through the rectangularly shaped shear layer, the prediction of the directional alteration can still give satisfying results by Amiet's approach. However, the correction method fails to predict the shear layer effects correctly in the amplitude change in the aforementioned 'dangerous area'.

From the primary study of the turbulence effects in both 2D and 3D, the scattering effects are found to be closely related to the source frequency, the flow speed and the shear layer thickness. The spectral broadening and the amplitude reduction becomes more severe as the source frequency, the flow speed and the shear layer thickness goes up. It is found that quantitatively the scattering may change the amplitudes more than the pure refraction. By the comparison of the integrated SPL at the tone frequency in 2D and 3D, it is noticed that the amplitude shows a similar trend in the variation with the streamwise location but a different characteristic in the variation with the flow speed. More data is needed to draw a conclusion about the 2D and 3D comparison.

### 5.3 Outlook

Current work provides some basic information and analysis of the shear layer effects as well as the evaluation of Amiet's approach. Based on these analyses, the following orientation of the further study is advised.

Considering the mean flow gradient effects through the shear layer, the 'corner' effect through the rectangular shear layer may be further investigated by extending the simulations to non central source positions and to other wind tunnels with rectangular nozzle. The relationship between the 'corner' effects (focussing and spreading) and the size of the nozzle geometry could be established for the correction in the aforementioned 'dangerous' area. Furthermore, a correction method, capable of dealing with the effects around this area, may be developed.

Considering the turbulence effects through the free shear layer, 3D simulations including the entire shear layer would be an important part to study the scattering effects in the AWB shear flow. Moreover, the comparison between numerical results and the experimental data or theoretical haystacking models is necessary.



# Derivation of Amiet's approach

The derivation of Amiet's approach [R. H. Schlinker 1980] [J. W. Delfs 2015] is presented here. Fig.A.1 shows the basic geometry and coordinate used in the following derivation. The basic idea has been presented in Chapter 2, which will not be given here.

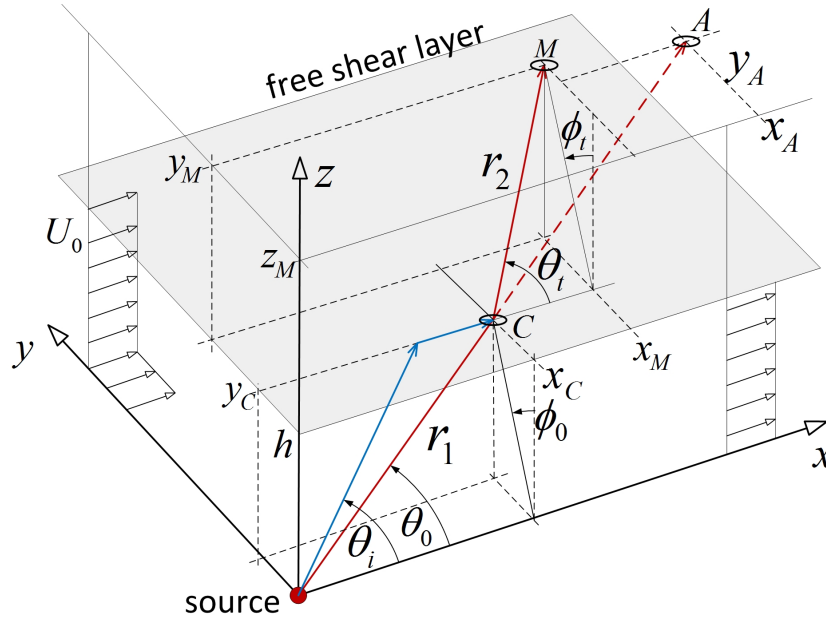


Figure A.1: Sketch of the 3D correction model.

## A.1 Refraction angle change

The incident wave is treated as a plane wave as passing through the shear layer. This assumption is reasonable as long as the incident wave length is smaller than the source to shear layer distance. The incident wave pressure can be written as

$$p_i = e^{i(\omega t - k_x x - k_y y - k_z z)} \quad (\text{A.1})$$

where  $k_x$ ,  $k_y$  and  $k_z$  indicate the wave vectors in the  $x$ ,  $y$  and  $z$  directions. Substituting the above expression into the convective wave equation

$$\left( \frac{D_0^2}{Dt^2} - a_\infty^2 \nabla^2 \right) p = 0 \quad (\text{A.2})$$

it can be obtained

$$k_{zi}^2 = \left(\frac{\omega}{a_\infty} - Mk_x\right)^2 - k_x^2 - k_y^2 \quad (\text{A.3})$$

where  $a_\infty$  is the sound speed in standard atmosphere,  $M$  is the flow Mach number calculated by  $M = U_0/a_\infty$ .

The normal direction to the wave front at the cross point can be given by taking the gradient of the phase of the incident wave as

$$\mathbf{n}_e = \frac{k_x \mathbf{i} + k_y \mathbf{j} + k_{zi} \mathbf{k}}{\omega/a_\infty - Mk_x} \quad (\text{A.4})$$

Due to the existence of the flow speed, the normal vector is relevant to the retarded source position, which deviates from the original source position with a vector  $\mathbf{i}M$ . Therefore, the energy propagation direction from the source to the cross point  $C$  can be expressed as

$$\mathbf{n}_i = \frac{n_e + \mathbf{i}M}{|n_e + \mathbf{i}M|} = \frac{[\omega M/a_\infty + (1 - M^2)k_x] \mathbf{i} + k_y \mathbf{j} + k_z \mathbf{k}}{\sqrt{\omega^2/a_\infty^2 + M^2[(\omega/a_\infty - Mk_x)^2 - k_x^2]}} \quad (\text{A.5})$$

Similarly, the pressure of transmitted wave above the shear layer at the cross point can be given as

$$p_t = T e^{i(\omega t - k_x x - k_y y - k_{zt} z)} \quad (\text{A.6})$$

where  $T$  is the transmitted wave amplitude. By substituting the above expression into the wave equation in stationary flow, it gives

$$k_{zt}^2 = \frac{\omega^2}{a_\infty^2} - k_x^2 - k_y^2 \quad (\text{A.7})$$

The normal vector to the wave front is

$$\mathbf{n}_t = \frac{a_\infty}{\omega} (k_x \mathbf{i} + k_y \mathbf{j} + k_{zt} \mathbf{k}) \quad (\text{A.8})$$

The wave vector  $k_x$  and  $k_y$  stay the same for as the incident wave, since the phase of the incident and transmitted waves should be equal across the shear layer [A. D. Pierce 1981]. To translate the relation into the angle relations between incident and transmitted wave, the coordinates at the cross point  $C$  is written as

$$\begin{aligned} x_C &= r_1 \cos \theta_0 \\ y_C &= r_1 \sin \theta_0 \sin \phi_0 \\ z_C &= r_1 \sin \theta_0 \cos \phi_0 \end{aligned} \quad (\text{A.9})$$

The normal vector along the radiation path  $r_1$  can be written in the angle form as

$$\mathbf{n}_i = \cos \theta_0 \mathbf{i} + \sin \theta_0 \sin \phi_0 \mathbf{j} + \sin \theta_0 \cos \phi_0 \mathbf{k} \quad (\text{A.10})$$

Comparing Eq.A.5 with A.10, the wave vectors can be expressed by the radiation angles as

$$k_x = \frac{\omega}{a_\infty(1-M^2)} \left( \frac{\cos \theta_0}{\sqrt{1-M^2 \sin^2 \theta_0}} - M \right) \quad (\text{A.11})$$

$$k_y = \frac{\omega}{a_\infty} \frac{\sin \theta_0 \sin \phi_0}{\sqrt{1-M^2 \sin^2 \theta_0}} \quad (\text{A.12})$$

$$k_{zi} = \frac{\omega}{a_\infty} \frac{\sin \theta_0 \cos \phi_0}{\sqrt{1-M^2 \sin^2 \theta_0}} \quad (\text{A.13})$$

The normal vector along  $r_2$  can be written in the transmitted angle form as

$$\mathbf{n}_t = \cos \theta_t \mathbf{i} + \sin \theta_t \sin \phi_t \mathbf{j} + \sin \theta_t \cos \phi_t \mathbf{k} \quad (\text{A.14})$$

Comparing the above equation with Eq.A.8, the wave vectors expressed in the transmitted angles are

$$k_x = \frac{\omega}{a_\infty} \cos \theta_t \quad (\text{A.15})$$

$$k_y = \frac{\omega}{a_\infty} \sin \theta_t \sin \phi_t \quad (\text{A.16})$$

$$k_{zt} = \frac{\omega}{a_\infty} \sin \theta_t \cos \phi_t \quad (\text{A.17})$$

Then, the relation between incident wave angles and transmitted wave angles are established as

$$\cos \theta_t = \frac{1}{1-M^2} \left( \frac{\cos \theta_0}{\sqrt{1-M^2 \sin^2 \theta_0}} - M \right) \quad (\text{A.18})$$

$$\sin \theta_t \sin \phi_t = \frac{\sin \theta_0 \sin \phi_0}{\sqrt{1-M^2 \sin^2 \theta_0}} \quad (\text{A.19})$$

The above equations can determine the shear layer refraction effect in the wave propagation direction, once the original radiation angles  $(\theta_0, \phi_0)$  are known. The angle correction equation 2.1 used in Chapter 2 is another form of Eq.A.18.

In the open jet wind tunnel tests, the measurement positions  $(\theta_M, \phi_M)$  are usually provided instead of radiation angles. To apply the angle correction practically, some additional angle relations need to be given.

$$\frac{z_M}{\cos \phi_M} \cot \theta_M = \frac{h}{\cos \phi_0} \cot \theta_0 + \frac{z_M - h}{\cos \phi_t} \cos \theta_t \quad (\text{A.20})$$

$$z_M \tan \phi_M = h \tan \phi_0 + (z_M - h) \tan \phi_t \quad (\text{A.21})$$

The combination of above equations with Amiet's angle correction (Eq.A.18, A.19) can help to define the shear layer refraction effect for a given measurement position. When the observer stands in the the same plane with the source perpendicular to the shear layer, Eq.A.20 degenerates to Eq.2.2 as the azimuth angles  $(\phi_M, \phi_0$  and  $\phi_t)$  equal to zero.

## A.2 Refraction amplitude change

The sound wave amplitude variation is determined by the ray tube divergence. Firstly considering the ray tube above the shear layer from the cross point  $C$  to the measurement point. The pressure amplitude ratio between these two points can be expressed as

$$\frac{\overline{p_C^2}}{\overline{p_M^2}} = \frac{dF_M}{dF_C} \quad (\text{A.22})$$

where  $dF_M$  and  $dF_C$  represent the cross-section area of the ray tube with the shear layer and the measurement plane respectively. Since the distance variation in the  $x$ - direction and  $y$ - direction can be related to the transmission angles as

$$\frac{dx_M dy_M}{d\theta_t d\phi_t} = J_M = \begin{vmatrix} \frac{\partial x_M}{\partial \theta_t} & \frac{\partial x_M}{\partial \phi_t} \\ \frac{\partial y_M}{\partial \theta_t} & \frac{\partial y_M}{\partial \phi_t} \end{vmatrix}$$

$$\frac{dx_C dy_C}{d\theta_t d\phi_t} = J_C = \begin{vmatrix} \frac{\partial x_C}{\partial \theta_t} & \frac{\partial x_C}{\partial \phi_t} \\ \frac{\partial y_C}{\partial \theta_t} & \frac{\partial y_C}{\partial \phi_t} \end{vmatrix}.$$

The cross-section area ratio can be written as

$$\frac{dF_M}{dF_C} = \frac{J_M}{J_C} \quad (\text{A.23})$$

To derive the pressure amplitude ratio, the expressions of the coordinates at the cross point needs to be given in the form of  $\theta_t$  and  $\phi_t$ . The expressions are derived from the geometric relationship and the angle correction equations in the last section.

$$x_C = \frac{h [(1 - M^2) \cos \theta_t + M]}{\sqrt{\zeta_t^2 - \sin^2 \phi_t \sin^2 \theta_t}} \quad (\text{A.24})$$

$$y_C = \frac{h \sin \theta_t \sin \phi_t}{\sqrt{\zeta_t^2 - \sin^2 \phi_t \sin^2 \theta_t}} \quad (\text{A.25})$$

where  $\zeta_t^2 = (1 - M \cos \theta_t)^2 - \cos^2 \theta_t$ . Similarly, the expressions of the coordinates at the measurement point are presented as

$$x_M = x_C + \frac{z_M - h}{\cos \phi_t \tan \theta_t} \quad (\text{A.26})$$

$$y_M = y_C + (z_M - h) \tan \phi_t \quad (\text{A.27})$$

Based on the above equations, the cross-section area can then be derived as a function of the transmission angles ( $\theta_t, \phi_t$ ), which is further used to calculate the pressure amplitude ratio. Nextly, the energy lost of the sound wave across the shear layer needs to be identified. Since the sound wave was treated as a plane wave as

it crosses through the shear layer, the velocity potentials of the incident, reflected and transmitted waves could be written as

$$\begin{aligned}\Phi_i &= e^{i(\omega t - k_x x - k_y y - k_{zi} z)} \\ \Phi_r &= R_\Phi e^{i(\omega t - k_x x - k_y y + k_{zi} z)} \\ \Phi_t &= T_\Phi e^{i(\omega t - k_x x - k_y y - k_{zt} z)}\end{aligned}\quad (\text{A.28})$$

where the subscript  $i, r, t$  represent the incident, reflected and transmitted wave, respectively. The expression of the wave vectors can be found in the previous angle derivation procedure. The pressure of the sound wave is derived from the velocity potential as

$$p = -\rho_0 \frac{D_0 \Phi}{Dt} \quad (\text{A.29})$$

At crossing the shear layer, the pressure amplitude and the fluid displacement needs to be matched on both sides [H. S. Ribner 1957] [J. W. Miles 1957]. The pressure relation gives

$$\left(\frac{\omega}{a_\infty} - M k_x\right)(e^{-i k_{zi} z} + R_\Phi e^{i k_{zi} z}) = T_\Phi \frac{\omega}{a_\infty} e^{-i k_{zt} z} \quad (\text{A.30})$$

The fluid displacement is matched by considering the interface as a rippled surface by the acoustic wave [H. S. Ribner 1957] [J. W. Miles 1957]. The surface moves in the  $x$  direction with velocity  $\omega/k_x$ . An observer's position is chosen to move with the ripple surface. Therefore, the mean flow velocity outside the shear layer would be  $-\omega/k_x$  while inside would be  $U_0 - \omega/k_x$ . By defining the perturbation velocity in  $z$ -direction as  $v_z$  and equating the flow slope on both sides, the following relation is generated

$$v_z^t = \frac{v_z^i + v_z^r}{1 - U_0 k_x / \omega} \quad (\text{A.31})$$

Since the velocity perturbation can be directly derived from the potential by  $v_z = \partial \Phi / \partial z$ , the above equation can be transformed to

$$\frac{\omega}{a_\infty} k_{zi} \left( e^{-i k_{zi} z} - R_\Phi e^{i k_{zi} z} \right) = \left( \frac{\omega}{a_\infty} - M k_x \right) k_{zt} T_\Phi e^{-i k_{zt} z} \quad (\text{A.32})$$

Combining Eqs.A.30 and A.32, the transmission ratio of the transmitted wave to incident wave through the shear layer can be obtained.

$$T_\Phi = \frac{2e^{iz(k_{zt} - k_{zi})} \frac{\omega}{a_\infty} \left( \frac{\omega}{a_\infty} - M k_x \right)}{\left( \frac{\omega}{a_\infty} - M k_x \right)^2 \frac{k_{zt}}{k_{zi}} + \frac{\omega^2}{a_\infty^2}} \quad (\text{A.33})$$

Due to the relation in Eq.A.29, the transmission ratio for the pressure is

$$\begin{aligned}
T &= \frac{\frac{\omega}{a_\infty} \Phi_t}{(\omega/a_\infty - Mk_x) \Phi_i} \\
&= \frac{2\omega^2/a_\infty^2}{(\omega/a_\infty - Mk_x)^2 k_{zt}/k_{zi} + \omega^2/a_\infty^2} \\
&= \frac{2\sqrt{\zeta_t^2 - \sin^2 \theta_t \sin^2 \phi_t}}{(1 - M \cos \theta_t)^2 \sin \theta_t \cos \phi_t + \sqrt{\zeta_t^2 - \sin^2 \theta_t \sin^2 \phi_t}} \quad (\text{A.34})
\end{aligned}$$

Until now the measurement data at the point  $M$  is traced back to the point  $C-$  just below the shear layer. The pressure amplitude at the corrected point  $A$  in the uniform flow can be determined by multiplying the data at  $C-$  with a distance factor  $h/z_M$ . The pressure ratio between the corrected point  $A$  and the measurement point  $M$  in the square value form can then be written as

$$\frac{\overline{p_A'^2}}{\overline{p_M'^2}} = \frac{h^2}{z_M^2} \frac{J_M}{J_C} \frac{[\sqrt{\zeta_t^2 - \sin^2 \theta_t \sin^2 \phi_t} + (1 - M \cos \theta_t)^2 \sin \theta_t \cos \phi_t]^2}{4(\zeta_t^2 - \sin^2 \theta_t \sin^2 \phi_t)} \quad (\text{A.35})$$

## Figures of the numerical results

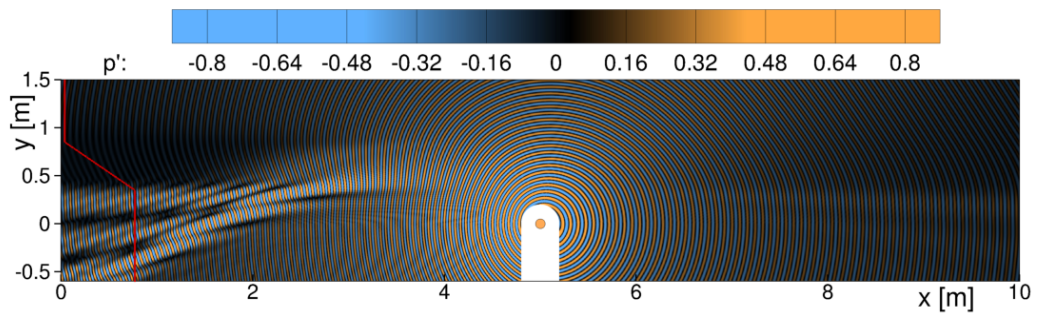
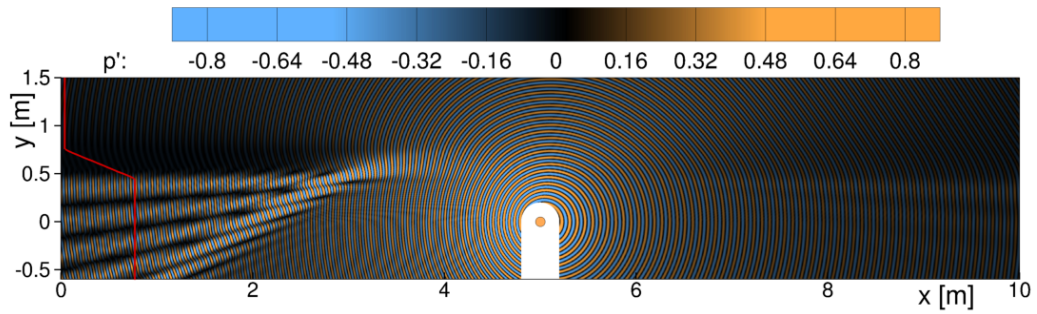
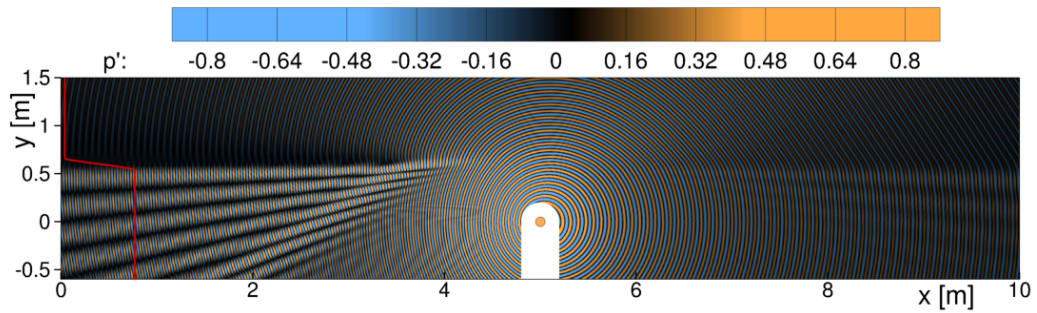


Figure B.1: Instantaneous pressure perturbation field through the constant thickness shear layer at the source frequency  $5kHz$  ( $U_0 = 60m/s$ ).

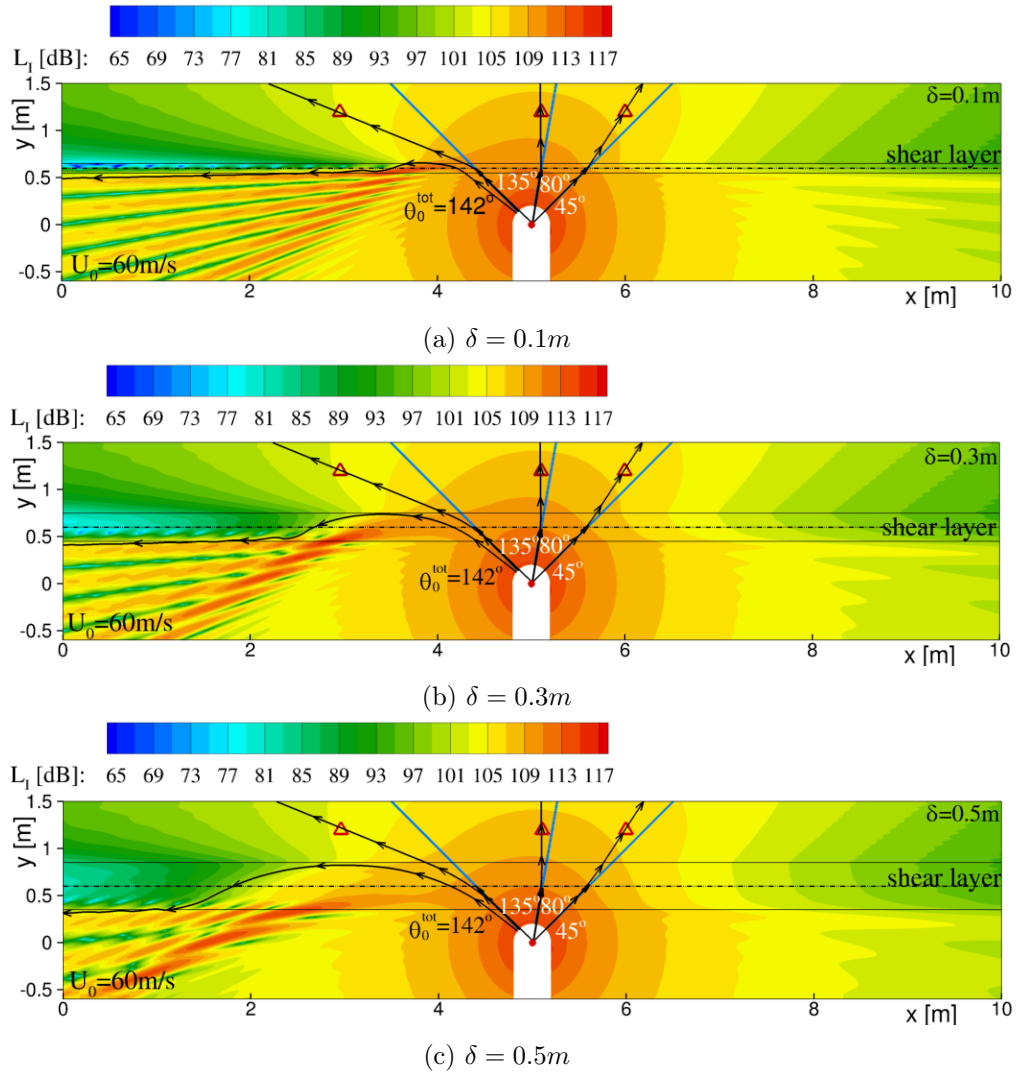


Figure B.2: Intensity level distribution through the constant thickness shear layer at the source frequency  $5kHz$ .

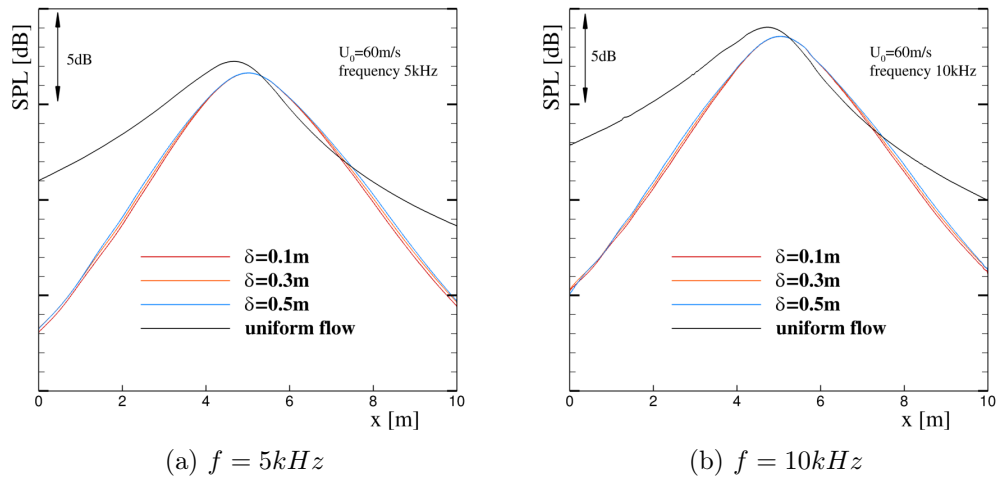
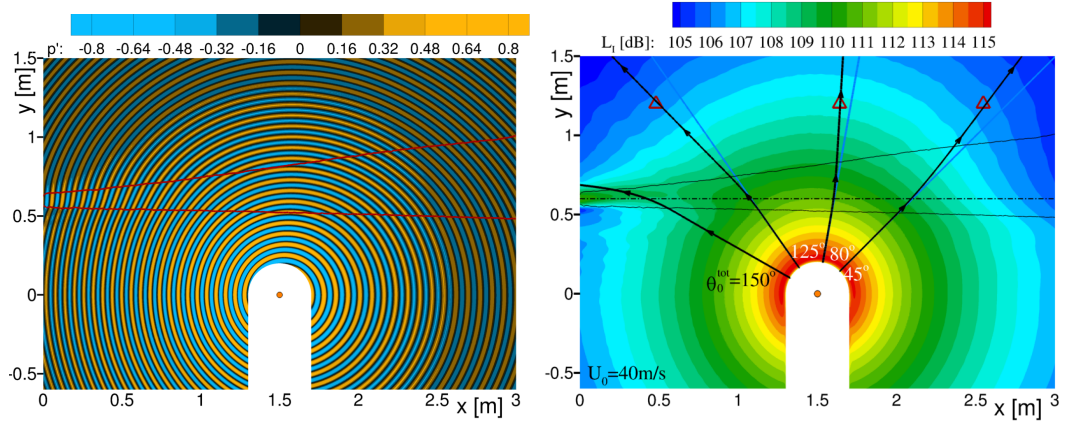
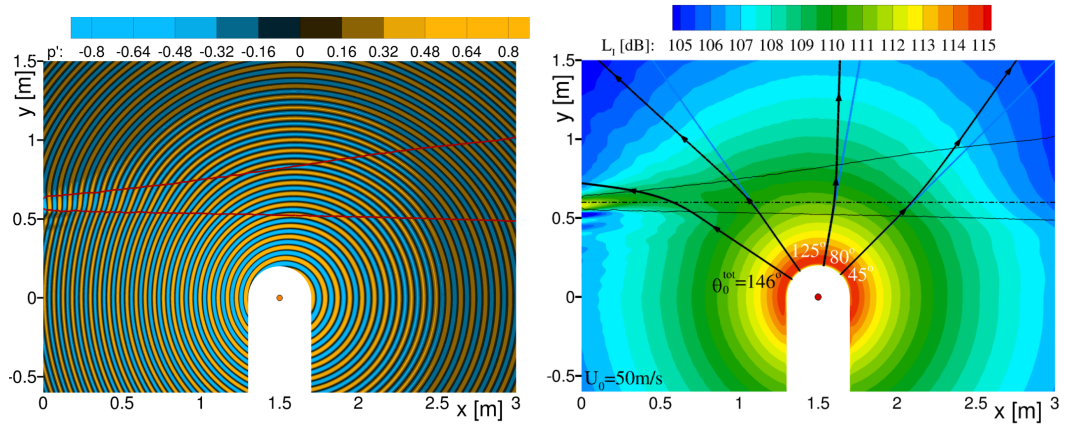
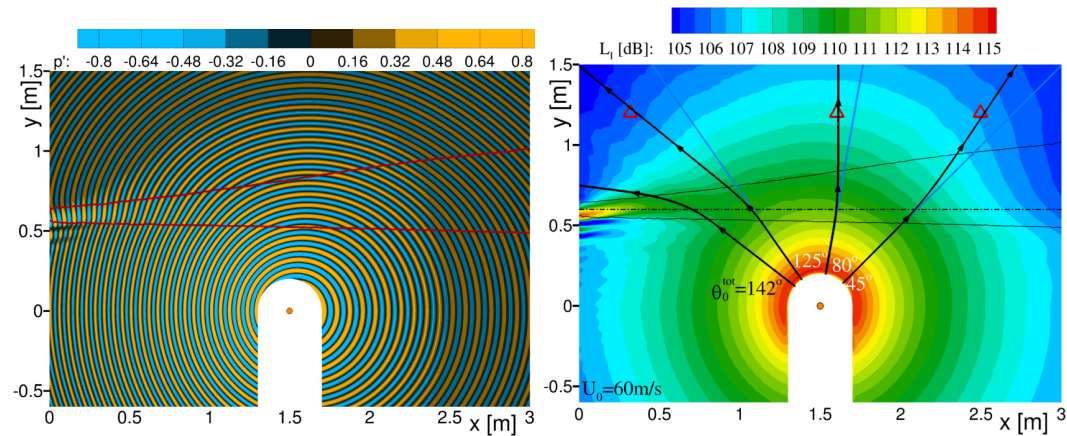


Figure B.3: The sound pressure level distribution along the microphone line  $y_M = 1.2m$  through the constant thickness shear layer.

(a)  $U_0 = 40 \text{ m/s}$ (b)  $U_0 = 50 \text{ m/s}$ (c)  $U_0 = 60 \text{ m/s}$ Figure B.4: left: Instantaneous pressure perturbation field ; right: Intensity level distribution through the 2D AWB shear layer at the source frequency  $5 \text{ kHz}$ .

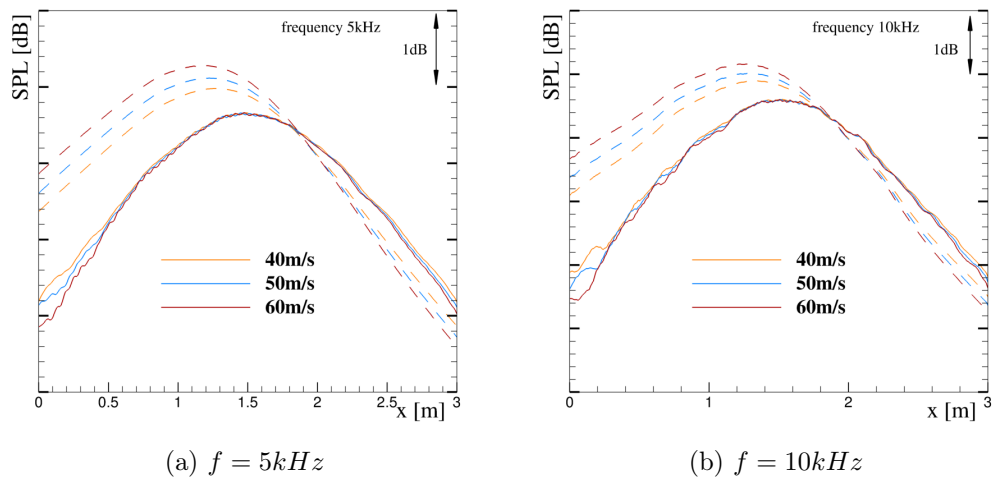


Figure B.5: The sound pressure level distribution along microphone line  $y_M = 1.2m$  through the 2D AWB shear layer.

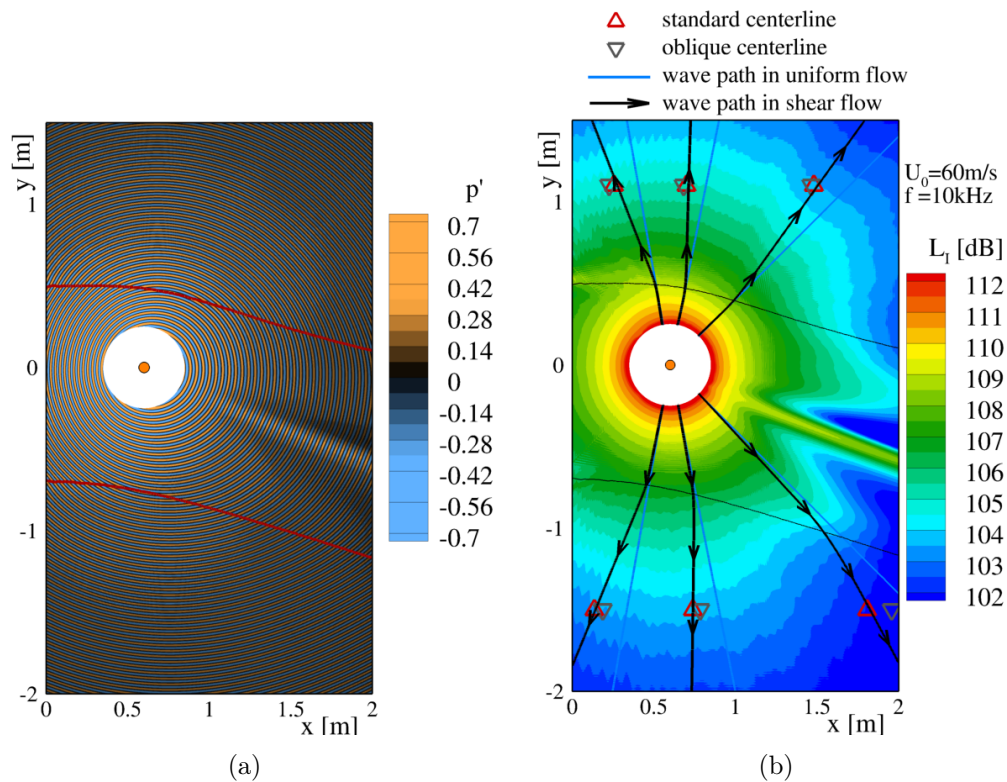


Figure B.6: (a)Instantaneous pressure perturbation field; (b)Sound intensity level field in the shear flow around the high-lift airfoil for source frequency at  $10kHz$ .

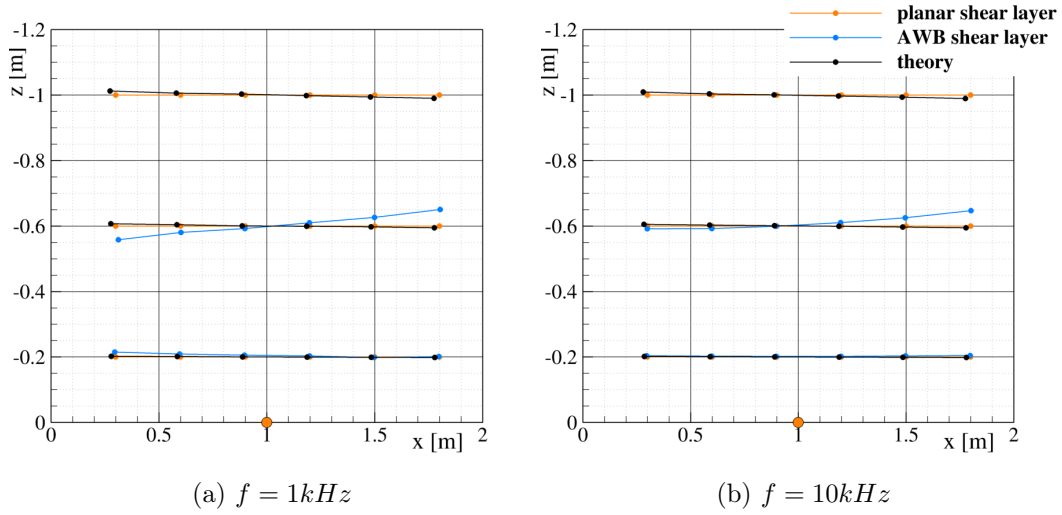


Figure B.7: Comparisons of transmitted wave direction between computations and the theory on the top plane ( $y = 1.15m$ ) in the shear flow with  $U_0 = 50m/s$ .

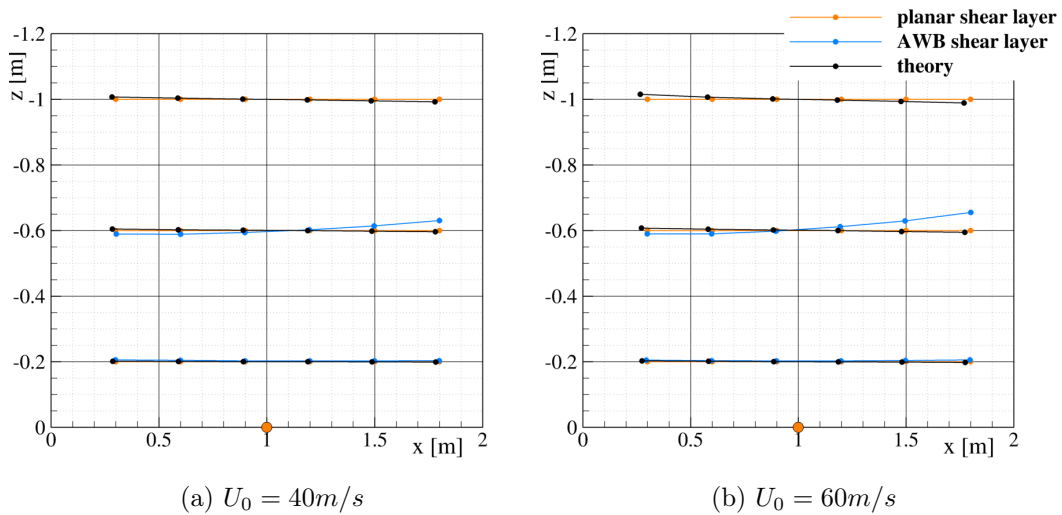


Figure B.8: Comparisons of transmitted wave direction between computations and the theory on the top plane ( $y = 1.15m$ ) at the source frequency  $f = 10kHz$ .

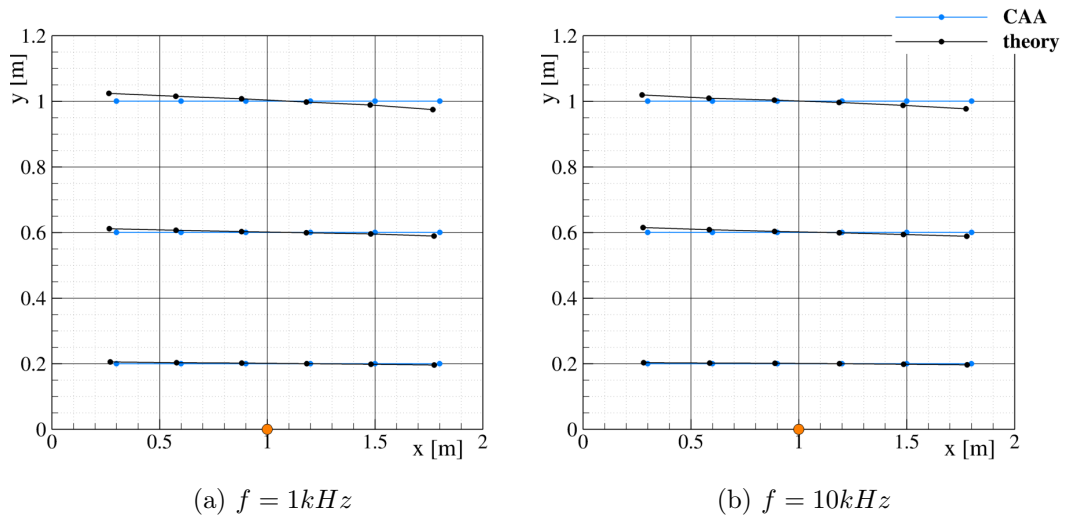


Figure B.9: Comparisons of transmitted wave direction between computations and the theory on the side plane ( $z = 1.15 \text{ m}$ ) in the shear flow with  $U_0 = 50 \text{ m/s}$  (AWB shear flow).

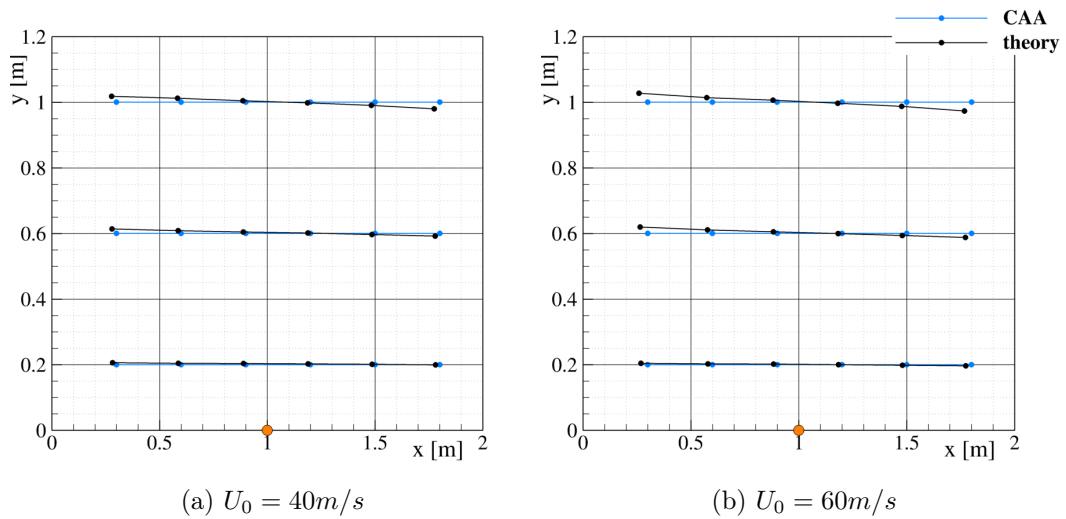


Figure B.10: Comparisons of transmitted wave direction between computations and the theory on the side plane ( $z = 1.15 \text{ m}$ ) at the source frequency  $f = 10 \text{ kHz}$  (AWB shear flow).



# Instabilities in the 3D simulation in the turbulent shear layer

The instability firstly appears in the low speed simulation ( $U_0 = 40m/s$ ) at the time step when  $t = 0.29s$  on one of the symmetrical plane ( $z = 0m$ ). Fig.C.1a gives the pressure contour at the corresponding time step, in which an unstable area is found near  $y = 0.6m$  in the upstream direction. A similar situation happens in the high speed simulation ( $U_0 = 60m/s$ ) at later time step ( $t = 0.5s$ ), refer to Fig.C.1b. The initial settings for both cases are exactly the same except the flow speed. On the contrary to  $40m/s$ , the insatibility happens at the dowanstream locations, but still on the symmetrical plane (where a slip-wall boundary condition is specified).

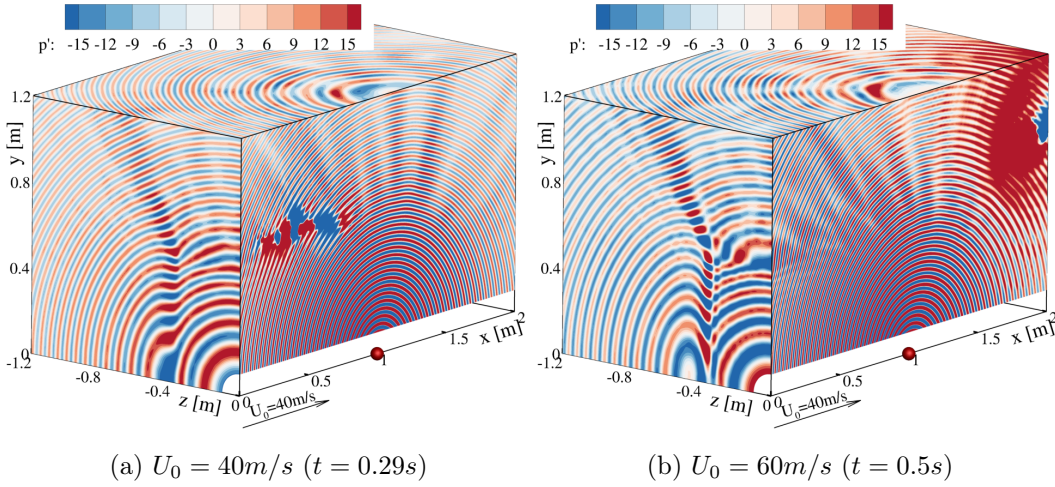


Figure C.1: Instantaneous pressure contour in the flow field.

It was speculated [Delfs] that the instability might be caused by the inappropriate handling of the turbulent flow in the slip wall boundary condition, in which the turbulent velocity  $\mathbf{u}_t$  is not considered. It would be a time-consuming way to add the  $\mathbf{u}_t$  to the slip wall boundary condition. Another easy and fast way to obtain a stable simulation would be adding a local 'Wall Damping' on the symmetrical wall, where the slip wall boundary condition was specified.

Therefore, in the following simulation the local 'Wall Damping' was added, while the other settings are kept the same as in previous simulations. Fig.C.2 plots the instantaneous pressure contour at the time step when  $t = 0.625s$ . Obviously, the

instability on the plane  $z = 0m$  disappears after the application of wall damping for both flow speeds.

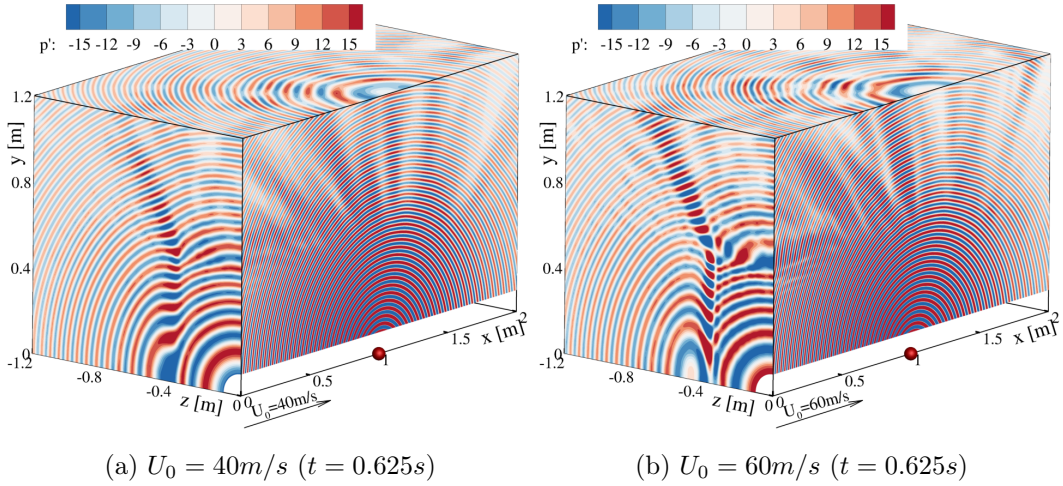


Figure C.2: Instantaneous pressure contour in the flow field.

The application of the wall damping may affect the simulation results and brings deviations into our analysis. To investigate its influences on simulation results, the following comparison was implemented. Since the simulation only becomes unstable at  $t = 0.5s$  at the flow speed  $U_0 = 60m/s$ , it is possible to study the effect of the wall damping before this time point in such a flow field. The simulations were done with a time duration  $t = 0.375s$ . One is implemented with wall damping, the other is without wall damping. Then the spectra at several microphone positions are compared to observe the effect of the wall damping.

Fig.C.3 shows the spectra comparison at different microphone locations, whose position in the computational domain can be found in Fig.4.64a. By such a comparison, it can be found out that the 'Wall Damping' does not bring obvious deviations into the spectral analysis. Therefore, the 'Wall Damping' will be applied in the 3D simulations in the turbulent shear flow to avoid the instability problem on the symmetrical plane.

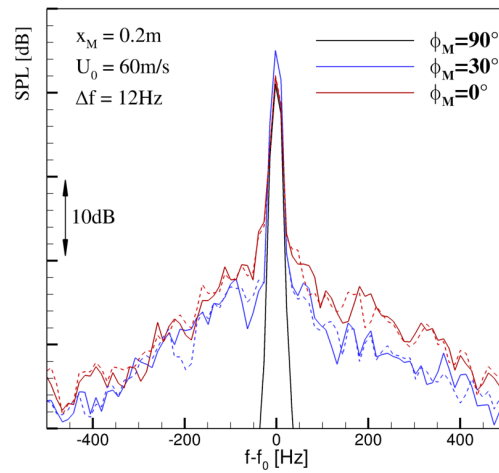
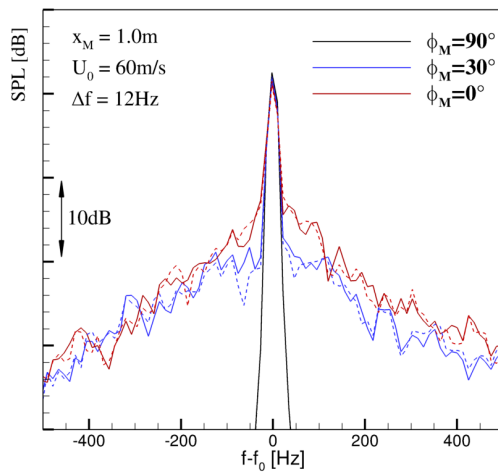
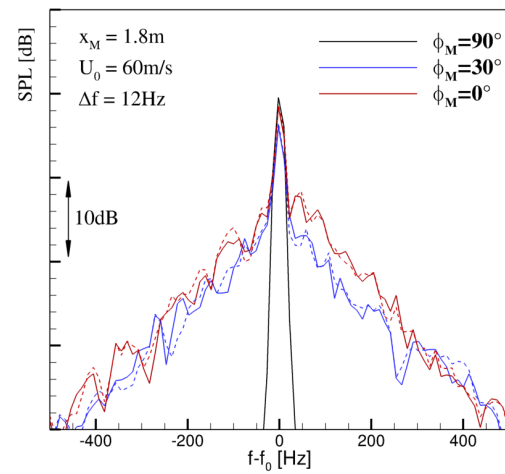
(a)  $x_M = 0.2m$ (b)  $x_M = 1.0m$ (c)  $x_M = 1.8m$ 

Figure C.3: CAA simulated spectra for wall damping effects in the AWB turbulent shear flow ( $U_0 = 60m/s$ ,  $\Delta f = 12Hz$ ) ( with wall damping —; without wall damping - - ).



# Nomenclature

## Abbreviations

APE	Acoustic Perturbation Equations
AWB	Aeroacoustic Wind tunnel Braunschweig
CAA	Computational AeroAcoustics
CFD	Computational Fluid Dynamics
DLR	German Aerospace Center
DNC	Direct Noise Computation
DNW	German-Dutch Wind tunnel
DRP	Dispersion Relation Preserving
FRPM	Fast Random Particle Method
LDDRK	Low-Dissipation, low-Dispersion Runge-Kutta
LEE	Linearized Euler Equations
PIANO	Perturbation Investigation of Aerodynamic NOise
RANS	Reynolds-Averaged Navier-Stokes
TKE	Turbulence Kinetic Energy

## List of Symbols

$a_\infty$	reference value of speed of sound
$\alpha$	geometric angle of attack
$\psi$	stream function
$\tau$	non-dimensionalized viscous stress
$\xi_0$	position vector of the source point
$I$	sound intensity
$M$	local Mach number vector
$n$	normal vector
$q$	non-dimensionalized heat flux density

---

$\mathbf{r}$	distance vector
$\mathbf{r}_0$	distance vector
$\mathbf{U}$	local flow velocity vector
$\mathbf{v}$	nondimensionalized velocity
$\mathbf{x}$	position vector
$\mathbf{x}^c$	position vector of the source location
$\mathbf{x}_{\text{ref}}$	position vector at the reference point
$\Delta x$	grid spacing
$\delta$	shear layer thickness, Dirac delta function
$\delta_{ij}$	Kronecker symbol
$\dot{\theta}'$	source term
$\eta$	similarity parameter
$\gamma$	heat capacity ratio
$\hat{A}$	FRPM scaling function
$\hat{\theta}_p$	magnitude of the harmonic source
$\lambda$	acoustic wavelength
$\mathcal{U}_i$	FRPM white noise field
$\mu_\infty$	reference value of dynamic viscosity
$\omega$	circular frequency
$\overline{p_A^2}$	mean square value of the pressure perturbation at the corrected point A
$\overline{p_M^2}$	mean square value of the pressure perturbation at the measurement point M
$\phi'$	representative of various perturbation quantities
$\phi_{\text{ref}}$	forcing function term
$\rho$	nondimensionalized density
$\rho_\infty$	reference value of density
$\sigma(\xi)$	fading function

---

$\tau_s$	FRPM time scale
$\theta_0$	radiation angle
$\theta_0^{tot}$	critical radiation angle of total reflection
$\theta_i$	incidence angle
$\theta_M$	measurement angle between shear layer and source-observer line
$\theta_t$	transmission angle between shear layer and sound wave propagation direction above the shear layer
$\theta_t^s$	critical transmission angle for zone of silence
$\zeta$	$\left[ (1 - M \cos \theta_t)^2 - \cos^2 \theta_t \right]^{1/2}$
$a_0$	local sound speed
$b$	half-value radius of Gaussian
$c_l$	coefficient for 7-point stencils
$c_p$	specific heat capacity
$f$	frequency
$f_0$	tone frequency
$G$	FRPM filter kernel
$h$	shear layer to source distance
$J_0, J_1$	Bessel function of the first kind, zeroth and first order
$k$	wave number
$k_\infty$	reference value of heat conductivity
$L$	characteristic length
$L_p$	sound pressure level (SPL)
$l_s$	FRPM length scale
$L_I$	sound intensity level
$M$	Mach number
$p$	nondimensionalized pressure
$p_t$	turbulent pressure fluctuation

$p_{\max}$	magnitude of the pressure pulse
$Pr$	Prandtl number
$r$	radius for directivity plotting (source point as the center)
$Re$	Reynolds number
$U$	flow velocity in x-direction
$U_0$	wind tunnel flow speed
$U_\infty$	reference value of flow speed
$Y_0, Y_1$	Bessel function of the second kind, zeroth and first order
$y_M$	observer/microphone to source distance
$y_{1/2}$	half-velocity line position

# Bibliography

- [A. D. Pierce 1981] A. D. Pierce. *Acoustics: an introduction to its physical principles and applications*, volume 20. McGraw-Hill New York, 1981. (Cited on pages 14 and 110.)
- [A. Guedel 1985] A. Guedel. *Scattering of an acoustic field by a free jet shear layer*. *Journal of Sound and Vibration*, vol. 100, no. 2, pages 285–304, 1985. (Cited on page 7.)
- [A. McAlpine 2009] A. McAlpine, C. J. Powles and B. J. Tester. *A weak scattering model for tone haystacking*. *AIAA Paper*, vol. 3216, page 2009, 2009. (Cited on page 7.)
- [A. Ozkul 1979] A. Ozkul and J. C. Yu. *An experimental investigation of acoustic radiation from a source inside a large turbulent free jet*. *The Journal of the Acoustical Society of America*, vol. 65, no. 2, pages 336–344, 1979. (Cited on pages 5 and 7.)
- [B. J. Tester 1976] B. J. Tester and C. L. Morfey. *Developments in jet noise modelling—theoretical predictions and comparisons with measured data*. *Journal of Sound and Vibration*, vol. 46, no. 1, pages 79–103, 1976. (Cited on page 5.)
- [B. J. Tester and R. H. Burrin 1974] B. J. Tester and R. H. Burrin. *On sound radiation from sources in parallel sheared jet flows*. In *American Institute of Aeronautics and Astronautics, Aerospace Sciences Meeting, 12 th*, Washington, D. C, 1974. (Cited on page 5.)
- [C. Bahr 2010] C. Bahr, N. S. Zawodny, T. Yardibi, F. Liu, D. Wetzel, B. Bertolucci and L. Cattafesta. *Shear layer correction validation using a non-intrusive acoustic point source*. In *16th AIAA/CEAS Aeroacoustics Conference*, page 3735, 2010. (Cited on page 5.)
- [C. Bahr 2011] C. Bahr, N. S. Zawodny, T. Yardibi, F. Liu, D. Wetzel, B. Bertolucci and L. Cattafesta. *Shear layer time-delay correction using a non-intrusive acoustic point source*. *International Journal of Aeroacoustics*, vol. 10, no. 5-6, pages 497–530, 2011. (Cited on page 5.)
- [C. L. Morfey 1977] C. L. Morfey and B. J. Tester. *Noise measurements in a free jet flight simulation facility: shear layer refraction and facility-to-flight corrections*. *Journal of Sound and Vibration*, vol. 54, no. 1, pages 83–106, 1977. (Cited on page 5.)
- [C. L. Morfey 2001] C. L. Morfey and P. F. Joseph. *Shear layer refraction corrections for off-axis sources in a jet flow*. *Journal of sound and vibration*, vol. 239, no. 4, pages 819–848, 2001. (Cited on page 5.)

- [C. Tam 1993] C. Tam and J. C. Webb. *Dispersion-relation-preserving finite difference schemes for computational acoustics*. Journal of computational physics, vol. 107, no. 2, pages 262–281, 1993. (Cited on pages 23 and 24.)
- [C. Tam 1994] C. Tam and Z. Dong. *Wall boundary conditions for high-order finite-difference schemes in computational aeroacoustics*. Theoretical and Computational Fluid Dynamics, vol. 6, no. 5-6, pages 303–322, 1994. (Cited on page 24.)
- [Delfs ] J. W. Delfs. Personal discussion with Prof. Delfs. (Cited on page 123.)
- [E. W. Graham 1969] E. W. Graham and B. B. Graham. *Effect of a Shear Layer on Plane Waves of Sound in a Fluid*. The Journal of the Acoustical Society of America, vol. 46, no. 1, pages 169–175, 1969. (Cited on page 5.)
- [F. Q. Hu 1996] F. Q. Hu, M. Y. Hussaini and J. L. Manthey. *Low-dissipation and low-dispersion Runge–Kutta schemes for computational acoustics*. Journal of Computational Physics, vol. 124, no. 1, pages 177–191, 1996. (Cited on page 23.)
- [H. S. Ribner 1957] H. S. Ribner. *Reflection, Transmission, and Amplification of Sound by a Moving Medium*. The Journal of the Acoustical Society of America, vol. 29, no. 4, pages 435–441, 1957. (Cited on pages 5, 11, 14 and 113.)
- [J. C. Hardin 1981] J. C. Hardin and J. S. Preisser. *Stochastic analysis of spectral broadening by a free turbulent shear layer*. 1981. (Cited on page 7.)
- [J. D. Belleval 1976] J. D. Belleval, M. Perulli, S. M. Candel and A. Julienne. *Analysis of problems posed by simulation of flight effects in anechoic open wind tunnels*. In American Institute of Aeronautics and Astronautics, Aero-Acoustics Conference, 3 rd, Palo Alto, Calif, page 1976, 1976. (Cited on page 6.)
- [J. W. Delfs 2008] J. W. Delfs, M. Bauer, R. Ewert, H. A. Grogger, M. Lummer and T. G. W. Lauke. Piano handbook, version 5.2 ed. 2008. (Cited on pages 21, 23 and 25.)
- [J. W. Delfs 2014] J. W. Delfs. Grundlagen der aeroakustik (basics of aeroacoustics), 2014. (Cited on pages 25 and 26.)
- [J. W. Delfs 2015] J. W. Delfs. Gliederung der vorlesung 'methoden der aeroakustik', 2015. (Cited on page 109.)
- [J. W. Miles 1957] J. W. Miles. *On the Reflection of Sound at an Interface of Relative Motion*. The Journal of the Acoustical Society of America, vol. 29, no. 2, pages 226–228, 1957. (Cited on pages 5, 11, 14 and 113.)
- [K. K. Ahuja 1978] K. K. Ahuja, B. J. Tester and H. K. Tanna. *The free jet as a simulator of forward velocity effects on jet noise*. 1978. (Cited on pages 4 and 7.)

- [K. K. Ahuja 1981] K. K. Ahuja, H. K. Tanna and B. J. Tester. *An experimental study of transmission, reflection and scattering of sound in a free jet flight simulation facility and comparison with theory*. Journal of Sound and Vibration, vol. 75, no. 1, pages 51–85, 1981. (Cited on pages 5 and 7.)
- [L. Koop 2005] L. Koop, K. Ehrenfried and S. Kröber. *Investigation of the systematic phase mismatch in microphone-array analysis*. AIAA Paper, vol. 2962, page 2005, 2005. (Cited on page 5.)
- [L. M. B. C. Campos 1986] L. M. B. C. Campos. *On waves in gases. Part I: Acoustics of jets, turbulence, and ducts*. Reviews of modern physics, vol. 58, no. 1, page 117, 1986. (Cited on page 12.)
- [M. J. Lighthill 1952] M. J. Lighthill. *On sound generated aerodynamically. I. General theory*. In Proceedings of the Royal Society of London A: Mathematical, Physical and Engineering Sciences, volume 211, pages 564–587. The Royal Society, 1952. (Cited on page 1.)
- [M. J. Lighthill 1953] M. J. Lighthill. *On the energy scattered from the interaction of turbulence with sound or shock waves*. In Mathematical Proceedings of the Cambridge Philosophical Society, volume 49, pages 531–551. Cambridge Univ Press, 1953. (Cited on pages 6 and 7.)
- [M. J. Lighthill 1954] M. J. Lighthill. *On sound generated aerodynamically. II. Turbulence as a source of sound*. In Proceedings of the Royal Society of London A: Mathematical, Physical and Engineering Sciences, volume 222, pages 1–32. The Royal Society, 1954. (Cited on page 1.)
- [M. Pott-Pollenske 2008] M. Pott-Pollenske and J. W. Delfs. *Enhanced capabilities of the aeroacoustic wind tunnel Braunschweig*. In 29th AIAA Aeroacoustics Conference, Vancouver, Paper, volume 2910, 2008. (Cited on page 16.)
- [M. S. Howe 1973] M. S. Howe. *Multiple scattering of sound by turbulence and other inhomogeneities*. Journal of Sound and Vibration, vol. 27, no. 4, pages 455–476, 1973. (Cited on page 6.)
- [M.K. Myers 1986] M.K. Myers. *An exact energy corollary for homentropic flow*. Journal of Sound and Vibration, vol. 109, no. 2, pages 277–284, 1986. (Cited on page 31.)
- [N. Kroll 1989] N. Kroll, C. Rossow, K. Becker and F. Thiele. *MEGAFLOW - A numerical flow simulation system*. In 21st Congress of the International Council of the Aeronautical Sciences, Melbourne, Australia, 1989. (Cited on page 21.)
- [P. Gottlieb 1960] P. Gottlieb. *Sound Source near a Velocity Discontinuity*. The Journal of the Acoustical Society of America, vol. 32, no. 9, pages 1117–1122, 1960. (Cited on page 5.)

- [P. Sijtsma 2014] P. Sijtsma, S. Oerlemans, T. Tibbe, T. Berkefeld and C. Spehr. *Spectral broadening by shear layers of open jet wind tunnels*. In 20th AIAA/CEAS Aeroacoustics Conference, pages 16–20, 2014. (Cited on page 7.)
- [R. Ewert 2007] R. Ewert. *RPM—the fast Random Particle-Mesh method to realize unsteady turbulent sound sources and velocity fields for CAA applications*. AIAA paper, vol. 4, page 1, 2007. (Cited on page 29.)
- [R. Ewert 2008] R. Ewert, O. Kornow, B. J. Tester, C. J. Powles, J. W. Delfs and M. Rose. *Spectral broadening of jet engine turbine tones*. AIAA Paper, vol. 2940, page 2008, 2008. (Cited on page 7.)
- [R. Ewert 2009] R. Ewert, O. Kornow, J. Delfs, J. Yin, T. Röber and M. Rose. *A CAA based approach to tone haystacking*. AIAA Paper, vol. 3217, page 2009, 2009. (Cited on page 29.)
- [R. Ewert 2011] R. Ewert, J. Dierke, J. Siebert, A. Neifeld, C. Appel, M. Siefert and O. Kornow. *CAA broadband noise prediction for aeroacoustic design*. Journal of sound and vibration, vol. 330, no. 17, pages 4139–4160, 2011. (Cited on pages 22 and 29.)
- [R. H. Schlinker 1980] R. H. Schlinker and R. K. Amiet. *Refraction and scattering of sound by a shear layer*, volume 3371. National Aeronautics and Space Administration, Scientific and Technical Information Branch, 1980. (Cited on pages 5, 7, 25, 36, 38, 85 and 109.)
- [R. K. Amiet 1975] R. K. Amiet. *Correction of Open Jet Wind Tunnel Measurements for Shear Layer Refraction*. In American Institute of Aeronautics and Astronautics Conference, volume 1, 1975. (Cited on pages 5 and 11.)
- [R. K. Amiet 1978] R. K. Amiet. *Refraction of sound by a shear layer*. Journal of Sound and Vibration, vol. 58, no. 4, pages 467–482, 1978. (Cited on pages 5 and 12.)
- [R. Ross 1981] R. Ross. *Spectral broadening effects in open wind tunnels in relation to noise assessment*. AIAA Journal, vol. 19, no. 5, pages 567–572, 1981. (Cited on page 7.)
- [R. Ross 1983] R. Ross, K. J. Young, R. M. Allen and J. C. A. van Ditshuizen. *Acoustic wave propagation through the shear layer of the DNW large open jet wind tunnel*. In American Institute of Aeronautics and Astronautics Conference, volume 1, 1983. (Cited on page 7.)
- [S. B. Pope 2000] S. B. Pope. *Turbulent flows*, 2000. (Cited on page 29.)
- [S. Candel 1975] S. Candel, A. Guedel and A. Julienne. *Refraction and scattering of sound in an open wind tunnel flow*. In ICIASF'75; 6th International Congress

- on Instrumentation in Aerospace Simulation Facilities, volume 1, pages 288–300, 1975. (Cited on pages 4, 6, 25, 83 and 88.)
- [S. M. Candel 1976] S. M. Candel. *Application of geometrical techniques to aeroacoustic problems*. In American Institute of Aeronautics and Astronautics Conference, 1976. (Cited on page 6.)
- [T. Padois 2013] T. Padois, C. Prax and V. Valeau. *Numerical validation of shear flow corrections for beamforming acoustic source localisation in open wind-tunnels*. Applied Acoustics, vol. 74, no. 4, pages 591–601, 2013. (Cited on page 5.)
- [V. Ciobaca 2009] V. Ciobaca, S. Melber-Wilkending and M. Pott-Pollenske. *A CFD process chain for simulating open windtunnel test sections*. 2009. (Cited on pages 21 and 34.)
- [W. H. Herkes 1985] W. H. Herkes, F. G. Strout and R. Ross. *Evaluation of a correction for sound propagation through free-jet shear layers*. Journal of Aircraft, vol. 22, no. 12, pages 1065–1071, 1985. (Cited on page 5.)
- [Y. Wang 2015] Y. Wang, J. Yang, Q. Jia, Z. Yang and Z. Shen. *An Improved Correction Method for Sound Source Drift in A Jet Flow and Its Application to A Wind Tunnel Measurement*. Acta Acustica united with Acustica, vol. 101, no. 3, pages 642–649, 2015. (Cited on page 5.)